

# Functional renormalization group for strongly interacting Fermi systems

Von der Fakultät Mathematik und Physik der Universität  
Stuttgart zur Erlangung der Würde eines Doktors der Naturwissenschaften  
(Dr. rer. nat.) genehmigte Abhandlung

vorgelegt von

**Demetrio Vilardi**

aus Reggio di Calabria (Italien)

Hauptberichter: Prof. Dr. Walter Metzner

Mitberichter: Prof. Dr. Maria Daghofer

Tag der mündlichen Prüfung: 12. Februar 2019

**Max-Planck-Institut für Festkörperforschung**  
**Stuttgart 2019**



*Io non l'ho piú questo bisogno,  
perché muojo ogni attimo, io,  
e rinasco nuovo e senza ricordi:  
vivo e intero, non piú in me,  
ma in ogni cosa fuori.*

*Uno, nessuno e centomila.* Luigi Pirandello



# Abstract

The treatment of strongly interacting two-dimensional Fermi systems constitutes one of the most challenging problems in the field of condensed matter physics. Many theoretical works focused on the strongly coupled Hubbard model, since it is expected to capture the most important physics of cuprate superconductors. Due to our methodological improvements and understanding of the frequency dependence of the two-particle vertex function, the functional renormalization group combined with the dynamical mean field theory can now be used to study competing correlations in the strongly interacting regime.

While limited to moderate interaction strengths, the functional renormalization group describes efficiently systems with a hierarchy of different energy scales and competing correlations. For instance, it provides definite evidence for  $d$ -wave superconductivity in the two-dimensional Hubbard model at moderate coupling. In a first project, we study the frequency dependence of the one-particle irreducible vertex function generated by the functional renormalization group flow. The frequency dependence, which becomes singular for strong interactions, appears to be important already for moderate couplings, and it cannot be represented by separate channels each depending on a single linear combination of frequencies.

For strongly interacting systems, the dynamical mean field theory captures strong local correlation effects nonperturbatively. With this approximation, we study the impact of local correlations on the magnetic susceptibility. The local dynamics strongly affects the spin response function and its momentum dependence. In contrast to the widely used random-phase approximation with self-energy corrections that predicts Néel antiferromagnetic order, the local vertex corrections favor an incommensurate order similar to the ordering instability predicted by the Fermi surface geometry, as for weakly

---

interacting systems.

The dynamical mean field theory is also used as starting point for the functional renormalization group flow. We demonstrate that, due to our improvements for the parametrization of the vertex function, this approach is actually able to access the strong coupling physics. Moreover, we derive a flow scheme that conserves the local contributions and reduces the truncation error of the flow equations. In the strongly interacting regime, we capture strong  $d$ -wave pairing correlations driven by magnetic fluctuations with a mechanism similar to the one observed in the weakly interacting system.

# Contents

<b>Introduction</b>	<b>v</b>
<b>1 From weak to strong coupling: fRG, DMFT and DMF<sup>2</sup>RG</b>	<b>1</b>
1.1 Functional renormalization group . . . . .	1
1.1.1 Functional derivation of flow equations . . . . .	1
1.1.2 Field expansion and truncation . . . . .	5
1.1.3 Vertex properties and flow equations . . . . .	11
1.1.4 Hubbard model: instabilities at weak coupling . . . . .	12
1.2 Dynamical mean field theory: strong correlation effects . . . . .	15
1.2.1 Dynamical mean field . . . . .	15
1.2.2 Anderson impurity model . . . . .	18
1.2.3 Hubbard model at half-filling: Mott transition vs Antiferromagnetism . . . . .	20
1.2.4 Vertex function and ladder-DMFT . . . . .	22
1.3 DMF <sup>2</sup> RG: Combining the fRG with the DMFT . . . . .	26
1.3.1 Formalism and implementation . . . . .	26
<b>2 Frequency dependent interaction with the functional RG</b>	<b>33</b>
2.1 Full dynamical decomposition . . . . .	34
2.2 Interaction scheme . . . . .	36
2.3 Instability analysis and phase diagram . . . . .	38
2.4 Vertex frequency dependence and charge divergence . . . . .	45
2.5 Self-energy and pseudogap . . . . .	51
<b>3 Dynamical effects on the nonlocal magnetic correlations</b>	<b>57</b>

---

3.1	Bethe-Salpeter equations and nonlocal spin susceptibility . . . . .	58
3.2	Dynamical vertex corrections to magnetic susceptibility . . . . .	60
<b>4</b>	<b>Magnetic and superconducting correlations with the fRG at strong coupling</b>	<b>67</b>
4.1	Vertex parametrization . . . . .	68
4.2	DMFT conserving scheme . . . . .	70
4.3	Single-channel approximation . . . . .	74
4.4	Flow at strong coupling: the role of the frequency dependence . . . . .	75
4.5	Nonlocal correlations at finite dopings . . . . .	80
	<b>Conclusion</b>	<b>89</b>
	<b>Appendix A Vertex and self-energy flow equations</b>	<b>95</b>
	<b>Appendix B Numerical setup</b>	<b>99</b>
	<b>Appendix C DMFT from a functional perspective</b>	<b>103</b>
	<b>Bibliography</b>	<b>120</b>
	<b>Acknowledgments</b>	<b>121</b>
	<b>Deutsche Zusammenfassung</b>	<b>124</b>

# Introduction

## Motivation and overview

The discovery of high-temperature superconductivity in cuprates by Bednorz and Müller [1] opened new challenges in the field of strongly correlated electron systems. Since then, much progress has been made on both the theoretical and experimental side. Due to the low dimensionality of the Cu-O plane, responsible for the relevant physics, nonlocal fluctuation effects are particularly important, leading to competing instabilities and a rich phase diagram [2, 3]. The competition between the antiferromagnetic and superconducting instabilities represents only part of the phase diagram, which exhibits many other features, such as, anomalous transport properties in the normal state [4], a pseudogap phase, and charge-density-wave order [5, 6].

Right after the discovery of superconducting cuprates, P. W. Anderson [7] proposed the two-dimensional Hubbard model on a square lattice for the electrons moving in the Cu-O planes. Zhang and Rice [8] showed that the single-band Hamiltonian is indeed able to capture the low energy physics of these compounds. This model [9] has been originally introduced for three-dimensional materials with partially filled  $d$ - or  $f$ -shells which exhibit, on one side, properties predicted by the band theory and, on the other side, features explained by the atomic model. The Hubbard model describes spin- $\frac{1}{2}$  lattice fermions with inter-site hopping amplitudes  $t_{ij}$  and a local interaction  $U$ . The Hamiltonian is given by

$$\mathcal{H} = \sum_{i,j,\sigma} t_{ij} c_{i,\sigma}^\dagger c_{j,\sigma} + U \sum_i n_{i,\uparrow} n_{i,\downarrow}, \quad (1)$$

where  $c_{i,\sigma}^\dagger$  ( $c_{i,\sigma}$ ) creates (annihilates) fermions on site  $i$  with spin orientation  $\sigma$  ( $\uparrow$  or

$\downarrow$ ), and  $n_{i,\sigma} = c_{i,\sigma}^\dagger c_{i,\sigma}$ . We consider the two-dimensional case on a square lattice and repulsive interaction  $U > 0$ . The hopping amplitude is restricted to  $t_{ij} = -t$  for nearest neighbors and  $t_{ij} = -t'$  for next-to-nearest neighbors. Fourier transforming the hopping matrix yields the bare dispersion relation as

$$\varepsilon_{\mathbf{k}} = -2t(\cos k_x + \cos k_y) - 4t' \cos k_x \cos k_y. \quad (2)$$

The Hamiltonian in Eq. (1) represents the competition between the tendency towards localization, driven by the onsite interaction term, and an itinerant electron picture at small coupling. Recently, it became possible to realize the Hubbard model in experiments by using an atomic quantum gas in an optical lattice [10, 11], see Ref. [12] for a review.

At half-filling the physics is dominated by strong antiferromagnetic fluctuations and the low energy physics is captured by the nonlinear sigma model [13].

While limited to weak coupling, methods like the fluctuations exchange approximation (FLEX) [14, 15], self-consistent perturbation theory around an ordered state [16], parquet approximation [17, 18] and functional renormalization group (fRG) [19, 20], provide a better understanding of the model. The self-consistent perturbation theory expands in powers of the interaction strength at fixed order parameter and can be used to correct the mean-field solution of the system [16]. The FLEX approximation partially decouples the fluctuating channels and describes the pairing instability with a spin-fluctuations mediated mechanism. On the other side, the parquet approach and the fRG treat all the interacting channels on equal footing. The equations involved in the parquet approach are, however, difficult to be implemented and have been solved only in special cases [17] or, more recently, with a rough momentum discretization [18].

The renormalization group (RG) dates back to the early 70s, when K. G. Wilson [21] applied the renormalization group to the quantum field theory for critical phenomena and reinterpreted it in terms of the scaling picture by Kadanoff [22]. The idea is to treat fluctuations at different scales by continuously taking them into account from the high-energy to the low-energy scales. This continuous integration defines the RG flow. Among the different implementations of the Wilsonian flows [23, 24], Wetterich's formulation, the one-particle irreducible fRG, is particularly efficient [19]. The fRG solves the functional integrals in a scale-selective way through an exact differential equation for the functional generator of the one-particle irreducible (1PI) vertex functions. The truncated

field expansion in terms of 1PI vertices introduces, in the context of the Hubbard model, a limitation to weak-to-moderate interaction strengths. Functional RG equations were first used for an unbiased instability analysis of the two-dimensional Hubbard model by Halboth and Metzner [25], Honerkamp *et al.* [26] and Zanchi and Schulz [27, 28]. A  $d$ -wave pairing instability in the Cooper channel has been observed in the weak coupling regime. The pairing mechanism is clearly of magnetic type, where strong antiferromagnetic fluctuations, generated at the early stage of the flow, drive the divergence of the  $d$ -wave pairing interaction.

A key object of the fRG is the two-particle vertex function, representing the fermionic effective interaction. For instance, it determines the susceptibilities and the flow of the self-energy. In a translation invariant system, the vertex depends on three independent frequency and momentum variables, making a precise numerical treatment difficult. A suitable parametrization is necessary for the numerical implementation of the flow equations. Several parametrizations in both frequency and momentum space have been proposed, for instance, in the Anderson impurity model [29, 30, 31], the Holstein-Hubbard model [32] and in the 2D Hubbard model [33, 34, 35]. The frequency dependence has received an increasing attention in this field. While irrelevant in power counting, the vertex frequency dependence becomes singular upon approaching instabilities toward symmetry breaking [34]; the singular dependence is associated with the appearance of Goldstone modes [36]. Husemann *et al.* [33] introduced a vertex decomposition in terms of pairing, magnetic and charge channels with a simplified treatment of the frequency dependence. In an earlier fRG analysis of the single-impurity Anderson model, Karrasch *et al.* [29] suggested an approximate parametrization where the frequency dependence of the vertex is supposed to be *separable*, where each channel depends only on a linear combination of frequencies. In the Hubbard model, with a refined parametrization, a spurious divergence without physical interpretation was found in the charge channel at finite frequency transfer [34].

Baier *et al.* [37] treated the fluctuations of the antiferromagnetic order parameter via a Hubbard-Stratonovich transformation. By using the dynamical bosonization [38], where the bosonization is continuously applied during the flow, they showed that at low temperature the flow is governed by the fluctuations associated with the Goldstone mode. In this way, the Mermin-Wagner theorem [39] is fulfilled already at the one-loop level.

At strong coupling, methods like quantum Monte Carlo (QMC) and the dynamical mean field theory (DMFT) [40, 41, 42], together with its extensions [43, 44], treat the correlation effects nonperturbatively. QMC is limited by the system size and by the statistical error which becomes a dramatic issue when considering the doped regime due to the famous sign problem. For a review of QMC for the 2D Hubbard model see Ref. [45].

By mapping the lattice system onto an impurity problem, the DMFT is able to include strong *local* correlations nonperturbatively. A major success of DMFT is the description of the Mott metal-insulator transition, which plays a crucial role in the strongly interacting Hubbard model. This method has been extended to cluster approximations to take short-ranged nonlocal correlations into account [43]. In this case, pairing order has been found by forcing the paramagnetic solution [46, 47]. Diagrammatic extensions of DMFT are able to include long-ranged correlations by perturbative methods [44]; for instance, we mention the dynamical vertex approximation (D $\Gamma$ A) [48] and the triply irreducible local expansion (TRILEX) [49]. In the search for superconducting solutions, both use the Eliashberg-type approximation with local vertex corrections. Within the D $\Gamma$ A in its ladder-approximation supplemented by the Moriyaesque  $\lambda$ -correction [50], Kitatani *et al.* [51] found a superconducting solution at moderate-to-strong coupling. The TRILEX has been recently applied to the Hubbard model [52].

Another diagrammatic extension of DMFT is the DMF<sup>2</sup>RG, introduced by Taranto *et al.* [53] and able to combine the strength of the DMFT with the fRG. In this formalism, the DMFT solution provides the starting condition for the flow equations. The Mott physics is captured by the DMFT, while the weaker nonlocal correlations may be captured by a manageable approximation of the exact fRG flow. This new method aims at the treatment of competing instabilities in the regime of intermediate-to-strong coupling. Taranto *et al.* [53] used an approximate vertex parametrization that limited the applicability to weak-to-moderate coupling. They applied this method at half-filling,  $t' = 0$  and finite temperature, where the expected antiferromagnetic instability has been found. Close to such instability, the self-energy acquires a strong momentum dependence only for the lowest available Matsubara frequency.

A better understanding of the effective interaction is essential in approaching the strong coupling regime. The frequency dependence of the vertex plays an increasingly important role in this regime, as has been confirmed for quantum impurity models [30,

31], and in the DMFT [44, 54]. A proper treatment of the frequency dependence of the vertex is mandatory for methods dealing with the interplay between fluctuations in all the channels and, at the same time, correlation effects at strong coupling.

## Contributions and outline

The thesis is organized as follows:

- In Chapter 1, we give a short introduction of the methods used in the thesis; these are the fRG, the DMFT, and the DMF<sup>2</sup>RG. The derivation of the fRG equations follows the formalism and conventions of the review by Metzner *et al.* [20]. We also comment on the truncation of the flow equation hierarchy for the vertices. Then, by starting from the local approximation of the self-energy, we derive the DMFT self-consistency condition for the Hubbard model. Within the DMFT, we discuss both the paramagnetic and the antiferromagnetic solutions at half-filling. Finally, we show how to consistently combine the fRG with the DMFT into the DMF<sup>2</sup>RG by letting the flow start from the DMFT solution.
- In Chapter 2, we apply the fRG at moderate coupling and finite temperature. We provide parametrizations of the vertex and the self-energy without any assumption on the frequency dependence, while projecting the momentum dependence onto a small set of form factors. We extend the decomposition introduced by Husemann *et al.* [34] by retaining the full frequency dependence of all interacting channels. A detailed analysis is performed by specifically focusing on the understanding and interpretation of the frequency structures that becomes important already at moderate coupling. *Nonseparable* frequency dependences appear to be important, meaning that the channels do not only depend on the bosonic frequency transfer but also on the remaining two fermionic frequencies. We confirm the presence of the spurious divergence in the charge channel observed in Ref. [34] and reveal its mechanism as a feedback effect of the frequency dependent magnetic channel on the charge channel. Such divergence is cancelled by the feedback of the self-energy, in contrast with the widespread assumption that the self-energy plays a minor role for moderate interaction. Consistently, we also study the frequency dependence of the self-energy, which is entirely generated by the vertex

frequency dependence, and calculate the quasiparticle weight and decay rate close to the antiferromagnetic instability. Parts of the chapter are published in

D. Vilaridi, C. Taranto, and W. Metzner

Nonseparable frequency dependence of the two-particle vertex in interacting fermion systems. *Phys. Rev. B*, **96** 235110 (2017).

- In Chapter 3, we study the effects of the local correlations to nonlocal magnetic properties. Although local in space, the DMFT vertex strongly changes the momentum dependence of the spin susceptibility. It not only affects the antiferromagnetic transition temperature but also the ordering wave vector of the dominant magnetic instability. We compare the momentum dependences of the DMFT susceptibility with a random-phase approximation (RPA), where the particle-hole bubble is dressed by the self-energy only. For instance in a specific doping range, while the RPA susceptibility predicts a Néel antiferromagnetic order, the DMFT susceptibility with vertex corrections exhibits an incommensurate ordering tendency. For large dopings, such local corrections enhance the distance of the incommensurate ordering wave vector from  $(\pi, \pi)$ . Surprisingly, the incommensurate ordering at strong coupling is similar to the one predicted by the Fermi surface geometry, as for weakly interacting Fermi systems. Parts of the chapter are published in

D. Vilaridi, C. Taranto, and W. Metzner

Dynamically enhanced magnetic incommensurability: Effects of local dynamics on nonlocal spin correlations in a strongly correlated metal. *Phys. Rev. B*, **97** 235110 (2018).

- In Chapter 4, we apply the DMF<sup>2</sup>RG at strong coupling. In this regime, an accurate parametrization of the full frequency dependence of the vertex is required, which becomes singular for strong interactions. We setup the flow in a new way that conserves the local corrections, already included at the DMFT level, thus improving the accuracy of the error generated by the truncation of the flow equation hierarchy. Moreover, we derive an analytic equivalence between the single-channel approximation of the DMF<sup>2</sup>RG and the DMFT. We show the failure of such equivalence at moderate-to-

---

strong coupling, once the frequency dependence of the vertex is approximated. This confirms that a proper parametrization of the vertex frequency dependence is necessary to access the strong coupling regime. We show dominant antiferromagnetic fluctuations for a wide doping range, predicting a Néel ordering at half-filling but incommensurate magnetic order for a sizeable doping. Strong  $d$ -wave pairing correlations appear at the edge of the antiferromagnetic regime. We are able to perform an analysis of the pairing fluctuations for the lowest reachable temperature. At strong coupling, the pairing fluctuations are clearly generated by nonlocal magnetic contributions, similar to the superconducting pairing mechanism as seen in the plain fRG at weak coupling [20]. Parts of the chapter are presented in the preprint

D. Vilaridi, C. Taranto, and W. Metzner

Antiferromagnetic and  $d$ -wave pairing correlations in the strongly interacting two-dimensional Hubbard model from the functional renormalization group.

ArXiv:1810.02290.



# From weak to strong coupling: fRG, DMFT and DMF<sup>2</sup>RG

In this chapter we introduce the three methods applied in this thesis. First, we focus on the functional renormalization group (fRG). While limited to weak-coupling, this method allows for an unbiased treatment of fluctuations, particularly suitable when studying the interplay of antiferromagnetism and superconductivity, and, more in general, competing instabilities. In the second part, we briefly introduce the dynamical mean field theory (DMFT), which allows for an accurate nonperturbative inclusion of local correlations by mapping the lattice problem onto an impurity model. In this way, the DMFT captures strong correlation effects at the local level, determining important physics, e.g. the Mott transition. In the last part, we show how to overcome the limitations of the two previous formalisms with the introduction of the DMF<sup>2</sup>RG, which combines the fRG with the DMFT. As we are going to see, this can be realized by starting the fRG flow from the DMFT solution. The fRG, DMFT and DMF<sup>2</sup>RG are applied to the 2D Hubbard model in Chapters 2, 3, and 4, respectively.

## 1.1 Functional renormalization group

### 1.1.1 Functional derivation of flow equations

In this section, we present the formal derivation of the functional renormalization group equation [19] for the one-particle irreducible (1PI) vertices by following the conventions of Ref. [20]. Let us start by considering the following action for a spin- $\frac{1}{2}$  system

$$S[\chi, \bar{\chi}] = - (\bar{\chi}, G_0^{-1} \chi) + V[\chi, \bar{\chi}], \quad (1.1)$$

where  $\chi$  and  $\bar{\chi}$  are Grassmann fields representing fermionic degrees of freedom. The notation  $(A, B) = \sum_x A(x)B(x)$  implies summation over the index  $x$ , collecting the imaginary time or frequency and the quantum numbers, which are, in our case, the momentum and the spin. For continuous variables, the sum over  $x$  involves an integration. Prefactors in the summation, for instance, the temperature  $T$  for the Matsubara sum, are included. The function  $G_0$  is the bare propagator, which, in the case of translation and spin invariant action, takes the form  $G_0(\omega, \mathbf{k}) = (i\omega - \epsilon_{\mathbf{k}} + \mu)^{-1}$ , with  $\epsilon_{\mathbf{k}}$  being the single-particle energy.  $V[\chi, \bar{\chi}]$  is a generic many-body interaction that fulfils SU(2) spin and U(1) global symmetries, corresponding to global spin rotation and global charge conservation, respectively. Since we do not focus on the symmetry broken regime in this thesis, we suppose that also the generating functionals, defined below, are fully symmetric with respect to SU(2) spin and U(1) symmetries.

The quantum theory is determined by the functional

$$W[\eta, \bar{\eta}] = -\ln \frac{1}{Z_0} \int \mathcal{D}\bar{\chi} \mathcal{D}\chi \exp\{-S[\chi, \bar{\chi}] + (\bar{\eta}, \chi) + (\bar{\chi}, \eta)\}, \quad (1.2)$$

which is the generating functional of connected Green's functions.  $Z_0$ , determined by

$$Z_0 = \int \mathcal{D}\bar{\chi} \mathcal{D}\chi \exp\{(\bar{\chi}, G_0^{-1} \chi)\}, \quad (1.3)$$

is the partition function of the non-interacting system.

The connected Green's functions can be calculated by functional derivatives

$$G^{(2m)}(x_1, \dots, x_m; x_{m+1}, \dots, x_{2m}) = (-1)^m \frac{\delta^{(2m)} W[\eta, \bar{\eta}]}{\delta \bar{\eta}(x_1) \dots \delta \bar{\eta}(x_m) \delta \eta(x_{m+1}) \dots \delta \eta(x_{2m})} \Big|_{\eta=\bar{\eta}=0}. \quad (1.4)$$

At this point, we introduce a new functional which provides a more efficient way to store the physical information, the *effective action* as the Legendre transform of  $W[\eta, \bar{\eta}]$ . For this scope, we define the fields

$$\psi = -\frac{\delta W}{\delta \bar{\eta}}, \quad \bar{\psi} = \frac{\delta W}{\delta \eta}, \quad (1.5)$$

and the effective action as

$$\Gamma[\psi, \bar{\psi}] = (\bar{\eta}, \psi) + (\bar{\psi}, \eta) + W[\eta, \bar{\eta}]. \quad (1.6)$$

On the right hand side  $\eta$  and  $\bar{\eta}$  must be understood as functionals  $\eta[\psi, \bar{\psi}]$  and  $\bar{\eta}[\psi, \bar{\psi}]$  obtained by the inversion of Eqs. (1.5). Taking the functional derivative of Eq. (1.6) with respect to  $\psi$  and  $\bar{\psi}$ , the inverse relations read

$$\eta = -\frac{\delta\Gamma}{\delta\bar{\psi}}, \quad \bar{\eta} = \frac{\delta\Gamma}{\delta\psi}. \quad (1.7)$$

The functional  $\Gamma[\psi, \bar{\psi}]$  generates the 1PI vertex functions

$$V^{(2m)}(x_1, \dots, x_m; x_{m+1}, \dots, x_{2m}) = \frac{\delta^{(2m)}\Gamma[\psi, \bar{\psi}]}{\delta\bar{\psi}(x_1)\dots\delta\bar{\psi}(x_m)\delta\psi(x_{m+1})\dots\delta\psi(x_{2m})} \Big|_{\psi=\bar{\psi}=0}. \quad (1.8)$$

There is a relation between the connected Green's functions, defined in Eq. (1.4), and the 1PI functions in Eq. (1.8). As an example, by taking the functional derivative of Eqs. (1.5) and (1.7) with respect to  $\psi$  and  $\bar{\psi}$ , it is possible to prove the following matrix relation

$$\begin{pmatrix} \frac{\delta^{(2)}W}{\delta\bar{\eta}\delta\eta} & -\frac{\delta^{(2)}W}{\delta\bar{\eta}\delta\bar{\eta}} \\ -\frac{\delta^{(2)}W}{\delta\eta\delta\eta} & \frac{\delta^{(2)}W}{\delta\eta\delta\bar{\eta}} \end{pmatrix} = \begin{pmatrix} \frac{\delta^{(2)}\Gamma}{\delta\bar{\psi}\delta\psi} & \frac{\delta^{(2)}\Gamma}{\delta\bar{\psi}\delta\bar{\psi}} \\ \frac{\delta^{(2)}\Gamma}{\delta\psi\delta\psi} & \frac{\delta^{(2)}\Gamma}{\delta\psi\delta\bar{\psi}} \end{pmatrix}^{-1}, \quad (1.9)$$

which, in the case of  $\psi = \bar{\psi} = 0$ , becomes a precise relation between the connected Green's function  $G^{(2)}$  and the 1PI function  $V^{(2)}$ .

As a first step towards the fRG formalism, we introduce in the path integral (1.2) a new parameter  $\Lambda$  in the bilinear part of the action (1.1) by replacing  $G_0 \rightarrow G_0^\Lambda$ . The functional integral (1.2) becomes

$$W^\Lambda[\eta, \bar{\eta}] = -\ln \frac{1}{Z_0^\Lambda} \int \mathcal{D}\bar{\chi}\mathcal{D}\chi \exp\{-S^\Lambda[\eta, \bar{\eta}] + (\bar{\eta}, \chi) + (\bar{\chi}, \eta)\}, \quad (1.10)$$

where the action

$$S^\Lambda[\eta, \bar{\eta}] = -(\bar{\chi}, G_0^{\Lambda-1}\chi) + V[\eta, \bar{\eta}], \quad (1.11)$$

and the factor

$$Z_0^\Lambda = \int \mathcal{D}\bar{\chi}\mathcal{D}\chi \exp(\bar{\chi}, G_0^{\Lambda-1}\chi) \quad (1.12)$$

depend on the new parameter  $\Lambda$  only through the function  $G_0^\Lambda$ . The idea of the fRG is to transform the calculation of the path integral (1.2) into a differential equation with respect to  $\Lambda$  with a well known initial condition. In practice, after having defined from the functional (1.10) a  $\Lambda$ -dependent effective action  $\Gamma^\Lambda[\psi, \bar{\psi}]$ , we derive an exact differential equation with respect to  $\Lambda$  with the full quantum action  $\Gamma[\psi, \bar{\psi}]$  as final solution. To recover the standard definition we impose  $G_0^{\Lambda_{\text{fin}}} = G_0$  for the final value  $\Lambda = \Lambda_{\text{fin}}$ .

The function  $G_0^\Lambda$  and, hence, the action  $S^\Lambda[\eta, \bar{\eta}]$ , has to respect the symmetries of the original action  $S[\eta, \bar{\eta}]$ . Other properties of the function  $G_0^\Lambda$  are discussed in the Section 1.1.2.

To derive the flow equation, we first extend definition (1.6) as

$$\Gamma^\Lambda[\psi, \bar{\psi}] = (\bar{\eta}, \psi) + (\bar{\psi}, \eta) + W^\Lambda[\eta, \bar{\eta}] \quad (1.13)$$

and consider the  $\Lambda$ -derivative of Eq. (1.10)

$$-e^{-W^\Lambda} \partial_\Lambda W^\Lambda = -e^{-W^\Lambda} \partial_\Lambda (\ln Z_{0,\Lambda}) + \left( \frac{\delta}{\delta \eta}, \dot{Q}^\Lambda \frac{\delta}{\delta \bar{\eta}} \right) e^{-W^\Lambda}, \quad (1.14)$$

where we used  $Q^\Lambda = (G_0^\Lambda)^{-1}$  and the notation  $\dot{Q}^\Lambda = \partial_\Lambda Q^\Lambda$ . The term  $\partial_\Lambda (\ln Z_{0,\Lambda})$  can be rewritten as follows

$$\partial_\Lambda \ln Z_{0,\Lambda} = \partial_\Lambda \ln \det Q^\Lambda = \partial_\Lambda \text{Tr} \ln Q = \text{Tr} G_0^\Lambda \dot{Q}^\Lambda,$$

where the trace operator is  $\text{Tr} A = \sum_a A_a$ . We are now able to write the flow equation for  $W^\Lambda$

$$\partial_\Lambda W^\Lambda = \text{Tr} \left( G_0^\Lambda \dot{Q}^\Lambda \right) + \text{Tr} \left[ \dot{Q}^\Lambda \frac{\delta^{(2)} W^\Lambda}{\delta \eta \delta \bar{\eta}} \right] - \left( \frac{\delta W^\Lambda}{\delta \eta}, \dot{Q}^\Lambda \frac{\delta W^\Lambda}{\delta \bar{\eta}} \right). \quad (1.15)$$

The flow equation for the effective action can be calculated directly from definition (1.13) and Eq. (1.15)

$$\begin{aligned} \partial_\Lambda \Gamma^\Lambda[\psi, \bar{\psi}] &= \partial_\Lambda W^\Lambda[\eta, \bar{\eta}] \Big|_{\eta^\Lambda = \bar{\eta}^\Lambda = \text{fixed}} + \left( \dot{\eta}, \frac{\delta W^\Lambda}{\delta \bar{\eta}} \right) - \left( \frac{\delta W^\Lambda}{\delta \eta}, \dot{\eta} \right) + (\dot{\eta}, \psi) + (\bar{\psi}, \dot{\eta}) \\ &= \partial_\Lambda W^\Lambda[\eta, \bar{\eta}] \Big|_{\eta^\Lambda = \bar{\eta}^\Lambda = \text{fixed}}, \end{aligned}$$

which leads to

$$\partial_\Lambda \Gamma^\Lambda[\psi, \bar{\psi}] = \text{Tr} \left( G_0^\Lambda \dot{Q}^\Lambda \right) + \left( \bar{\psi}, \dot{Q}^\Lambda \psi \right) - \text{Tr} \left[ \dot{Q}^\Lambda \left( \mathbf{\Gamma}^{(2)\Lambda}[\psi, \bar{\psi}] \right)_{11}^{-1} \right]. \quad (1.16)$$

$\left( \mathbf{\Gamma}^{(2)\Lambda}[\psi, \bar{\psi}] \right)_{11}^{-1}$  is the first element of the inverse matrix of second functional derivatives

$$\mathbf{\Gamma}^{(2)\Lambda}[\psi, \bar{\psi}] = \begin{pmatrix} \frac{\delta^{(2)} \Gamma^\Lambda}{\delta \psi \delta \bar{\psi}} & \frac{\delta^{(2)} \Gamma^\Lambda}{\delta \bar{\psi} \delta \psi} \\ \frac{\delta^{(2)} \Gamma^\Lambda}{\delta \psi \delta \psi} & \frac{\delta^{(2)} \Gamma^\Lambda}{\delta \bar{\psi} \delta \bar{\psi}} \end{pmatrix}. \quad (1.17)$$

Eq. (1.16), named Wetterich's equation [19], is exact. This equation determines the functional  $\Gamma^\Lambda[\psi, \bar{\psi}]$  step by step during the flow. It is not exactly solvable, but it represents a flexible starting point for appropriate approximation schemes based on physical assumptions. The approximation that is involved in this thesis simplifies the treatment of the field dependence. In fact, by truncating the field expansion, as discussed in the next section, Eq. (1.16) transforms into a hierarchy of ordinary differential equations (ODE) with respect to  $\Lambda$ .

### 1.1.2 Field expansion and truncation

Solving exactly Eq. (1.16) is more than a challenge, since the unknown variable  $\Gamma^\Lambda[\psi, \bar{\psi}]$  is not a standard function but rather a functional. To overcome this difficulty, depending on the underlying physical motivation, one can carry out a specific and pragmatic approximation [20]. For our scope, we use the field expansion, particularly suitable for an instability analysis, *i.e.*, selecting the leading instability among different channels.

By following Ref. [20], we expand the functional  $\Gamma^\Lambda[\psi, \bar{\psi}]$  using the 1PI functions defined in Eq. (1.8)

$$\Gamma^\Lambda[\psi, \bar{\psi}] = \sum_{m=0}^{\infty} \frac{(-1)^m}{(m!)^2} \sum_{x_1, \dots, x_{2m}} V^{(2m)\Lambda}(x_1, \dots, x_m; x_{m+1}, \dots, x_{2m}) \times \bar{\psi}(x_1) \dots \bar{\psi}(x_m) \psi(x_{m+1}) \dots \psi(x_{2m}). \quad (1.18)$$

The idea is to plug Eq. (1.18) into Wetterich's equation (1.16) and extract an hierarchy of differential equations for  $V^{(2m)\Lambda}$ . Before proceeding, we take care of the inverse matrix

$(\mathbf{\Gamma}^{(2)\Lambda}[\psi, \bar{\psi}])^{-1}$  by splitting  $\mathbf{\Gamma}^{(2)\Lambda}$  into a field dependent and a field independent part

$$\mathbf{\Gamma}^{(2)\Lambda}[\psi, \bar{\psi}] = (\mathbf{G}^\Lambda)^{-1} - \tilde{\mathbf{\Gamma}}^\Lambda[\psi, \bar{\psi}]. \quad (1.19)$$

Since we exclude the possibility of U(1) symmetry breaking, the field independent part has the form

$$\mathbf{G}^\Lambda = (\mathbf{\Gamma}^{(2)\Lambda}[0, 0])^{-1} = \text{diag}(G^\Lambda, -G^\Lambda). \quad (1.20)$$

Now we can insert the expansion

$$(\mathbf{\Gamma}^{(2)\Lambda})^{-1} = (\mathbf{1} - \mathbf{G}^\Lambda \tilde{\mathbf{\Gamma}})^{-1} \mathbf{G}^\Lambda = \sum_{l=0}^{\infty} (\mathbf{G}^\Lambda \tilde{\mathbf{\Gamma}}^\Lambda)^l \mathbf{G}^\Lambda \quad (1.21)$$

into Eq. (1.16)

$$\partial_\Lambda \Gamma^\Lambda[\psi, \bar{\psi}] = \text{Tr} \left( (G_0^\Lambda - G^\Lambda) \dot{Q}^\Lambda \right) + \left( \bar{\psi}, \dot{Q}^\Lambda \psi \right) + \text{Tr} \left\{ \dot{Q}^\Lambda \sum_{l=0}^{\infty} \left[ \left( \mathbf{G}^\Lambda \tilde{\mathbf{\Gamma}}^\Lambda[\psi, \bar{\psi}] \right)^l \mathbf{G}^\Lambda \right]_{11} \right\}. \quad (1.22)$$

We are ready to extract the flow equations for  $V^{(2m)\Lambda}$  by taking the functional derivatives of Eq. (1.22) evaluated at zero fields. The second functional derivatives, together with the Dyson equation  $V^{(2)\Lambda} = (G^\Lambda)^{-1} = (G_0^\Lambda)^{-1} - \Sigma^\Lambda$ , leads to the flow equation for the SU(2) spin symmetric self-energy  $\Sigma^\Lambda(k) \equiv \Sigma_\uparrow^\Lambda(k) = \Sigma_\downarrow^\Lambda(k)$

$$\partial_\Lambda \Sigma^\Lambda(k) = \sum_\sigma \int_p S^\Lambda(p) V_{\sigma, \uparrow, \sigma, \uparrow}^\Lambda(p, k, p). \quad (1.23)$$

We introduced the so called single-scale propagator

$$S^\Lambda = \partial_\Lambda G^\Lambda \Big|_{\Sigma^\Lambda \text{ const}} = -G^\Lambda \dot{Q}^\Lambda G^\Lambda, \quad (1.24)$$

as the derivative of the Green's function at fixed self-energy. Here, the index  $k = (\mathbf{k}, \nu)$  represents, at the same time, the momentum  $\mathbf{k}$  in the Brillouin zone and the discrete Matsubara frequency,  $\nu_n = (2n + 1)\pi T$ . Moreover, the shorthand notation  $\int_p = T \sum_\omega \int_{\mathbf{p}}$  is used, where  $\sum_\omega$  is the Matsubara frequency sum, and  $\int_{\mathbf{p}} = \int \frac{d\mathbf{p}}{(2\pi)^2}$  is the normalized integration over the first Brillouin zone. For the two-particle vertex we used  $V^{(4)\Lambda} = V_{\sigma_1, \sigma_2, \sigma_3, \sigma_4}^\Lambda(k_1, k_2, k_3)$ , where  $k_i$  and the spin indices  $\sigma_i = \uparrow, \downarrow$  follow the notation in

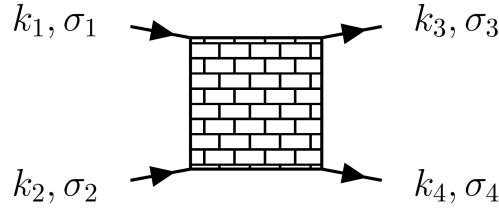


Figure 1.1: Vertex notation. The "bricks" pattern used for the box refers to the famous record by Pink Floyd: "The Wall".

Fig. 1.1. The fourth momentum  $k_4 = k_1 + k_2 - k_3$  is fixed by momentum conservation.

The flow equation for the vertex  $V^\Lambda$  reads

$$\begin{aligned} \partial_\Lambda V_{\sigma_1, \sigma_2, \sigma_3, \sigma_4}^\Lambda(k_1, k_2, k_3) = & \mathcal{T}_{\sigma_1, \sigma_2, \sigma_3, \sigma_4}^{\text{pp}}(k_1, k_2, k_3) + \mathcal{T}_{\sigma_1, \sigma_2, \sigma_3, \sigma_4}^{\text{ph}}(k_1, k_2, k_3) \\ & + \mathcal{T}_{\sigma_1, \sigma_2, \sigma_3, \sigma_4}^{\text{phc}}(k_1, k_2, k_3) + \mathcal{T}_{\sigma_1, \sigma_2, \sigma_3, \sigma_4}^{\text{V}_6}(k_1, k_2, k_3), \end{aligned} \quad (1.25)$$

where we defined

$$\begin{aligned} \mathcal{T}_{\sigma_1, \sigma_2, \sigma_3, \sigma_4}^{\text{pp}}(k_1, k_2, k_3) = & -\frac{1}{2} \sum_{\bar{\sigma}_1, \bar{\sigma}_2} \int_p \mathcal{P}_{\text{pp}}^\Lambda(k_1 + k_2, p) V_{\sigma_1, \sigma_2, \bar{\sigma}_1, \bar{\sigma}_2}^\Lambda(k_1, k_2, k_1 + k_2 - p) \\ & \times V_{\bar{\sigma}_1, \bar{\sigma}_2, \sigma_3, \sigma_4}^\Lambda(k_1 + k_2 - p, p, k_3), \end{aligned} \quad (1.26)$$

$$\begin{aligned} \mathcal{T}_{\sigma_1, \sigma_2, \sigma_3, \sigma_4}^{\text{ph}}(k_1, k_2, k_3) = & \sum_{\bar{\sigma}_1, \bar{\sigma}_2} \int_p \mathcal{P}_{\text{ph}}^\Lambda(k_3 - k_1, p) V_{\sigma_1, \bar{\sigma}_1, \sigma_3, \bar{\sigma}_2}^\Lambda(k_1, p + k_3 - k_1, k_3) \\ & \times V_{\bar{\sigma}_2, \sigma_2, \bar{\sigma}_1, \sigma_4}^\Lambda(p, k_2, p + k_3 - k_1), \end{aligned} \quad (1.27)$$

$$\begin{aligned} \mathcal{T}_{\sigma_1, \sigma_2, \sigma_3, \sigma_4}^{\text{phc}}(k_1, k_2, k_3) = & -\sum_{\bar{\sigma}_1, \bar{\sigma}_2} \int_p \mathcal{P}_{\text{ph}}^\Lambda(k_2 - k_3, p) V_{\sigma_1, \bar{\sigma}_1, \sigma_4, \bar{\sigma}_2}^\Lambda(k_1, p + k_2 - k_3, k_1 + k_2 - k_3) \\ & \times V_{\bar{\sigma}_2, \sigma_2, \bar{\sigma}_1, \sigma_3}^\Lambda(p, k_2, p + k_2 - k_3), \end{aligned} \quad (1.28)$$

$$\mathcal{T}_{\sigma_1, \sigma_2, \sigma_3, \sigma_4}^{\text{V}_6}(k_1, k_2, k_3) = - \sum_{\bar{\sigma}} \int_q S^\Lambda(q) V_{\bar{\sigma}, \sigma_1, \sigma_2, \bar{\sigma}, \sigma_3, \sigma_4}^{(6)\Lambda}(q, k_1, k_2; q, k_3). \quad (1.29)$$

We have defined the quantities

$$\mathcal{P}_{\text{ph}}^\Lambda(Q, p) = G^\Lambda(Q + p)S^\Lambda(p) + G^\Lambda(p)S^\Lambda(Q + p), \quad (1.30a)$$

$$\mathcal{P}_{\text{pp}}^\Lambda(Q, p) = G^\Lambda(Q - p)S^\Lambda(p) + G^\Lambda(p)S^\Lambda(Q - p). \quad (1.30b)$$

In Fig. 1.2, we report the diagrammatic representation of the flow equations.

As in the case of the self-energy, the SU(2) symmetry implies  $G^\Lambda(k) \equiv G_\uparrow^\Lambda(k) = G_\downarrow^\Lambda(k)$  and  $S^\Lambda(k) \equiv S_\uparrow^\Lambda(k) = S_\downarrow^\Lambda(k)$ . Eqs. (1.23) and (1.25) do not constitute a closed set of equations, since the term (1.29) depends on  $V^{(6)\Lambda}$ ; its flow equation can be computed by taking higher functional derivatives of Wetterich's equation (1.22) and can be found in Ref. [20]. In general, we obtain an infinite hierarchy of equations where  $\dot{V}^{(n)\Lambda}$  depends also on  $V^{(n+2)\Lambda}$ ; as a consequence, to come up with a closed set of equations, a truncation is necessary. In this thesis, we use the so called level-2 truncation, defined by the approximation  $\mathcal{T}^{\text{V}_6} \simeq 0$ . However, the remaining terms  $\mathcal{T}^{\text{pp}}$ ,  $\mathcal{T}^{\text{ph}}$  and  $\mathcal{T}^{\text{phc}}$  capture the unbiased competition of particle-particle and particle-hole fluctuations. With this truncation, the resulting fRG equations are able to fully describe the interplay between antiferromagnetism and  $d$ -wave superconductivity at weak-to-intermediate coupling [25, 55, 56, 20].

On the other hand, neglecting the term  $\mathcal{T}^{\text{V}_6}$  has physical consequences that go beyond the scope of this thesis. For example, an approximate inclusion of  $\mathcal{T}^{\text{V}_6}$  improves the fulfilment of the Ward identities [57] and allows for a continuation of the flow into the symmetry broken phase [58, 59] in the fermionic fRG. We will see that our truncation violates the Mermin-Wagner theorem [39], stating that, in case of a short range interaction, continuous symmetries cannot be spontaneously broken at finite temperature in two-dimensional systems and at any temperature in one dimension.

So far, we did not discuss the details of the  $\Lambda$ -dependence in the function  $G_0^\Lambda$ , important for the flow of the vertex and of the self-energy. The derivation of flow equations is valid for any choice of the function  $G_0^\Lambda$ , providing the following properties are fulfilled [20]: proper initial (discussed below) condition and final condition as  $G_0^{\Lambda_{\text{fin}}} = G_0$ ; the regularization of the infrared divergences, when present in  $G_0$ ; the differentiability (with respect to  $\Lambda$ ) of all the functions involved in the flow; finally, as stated above,

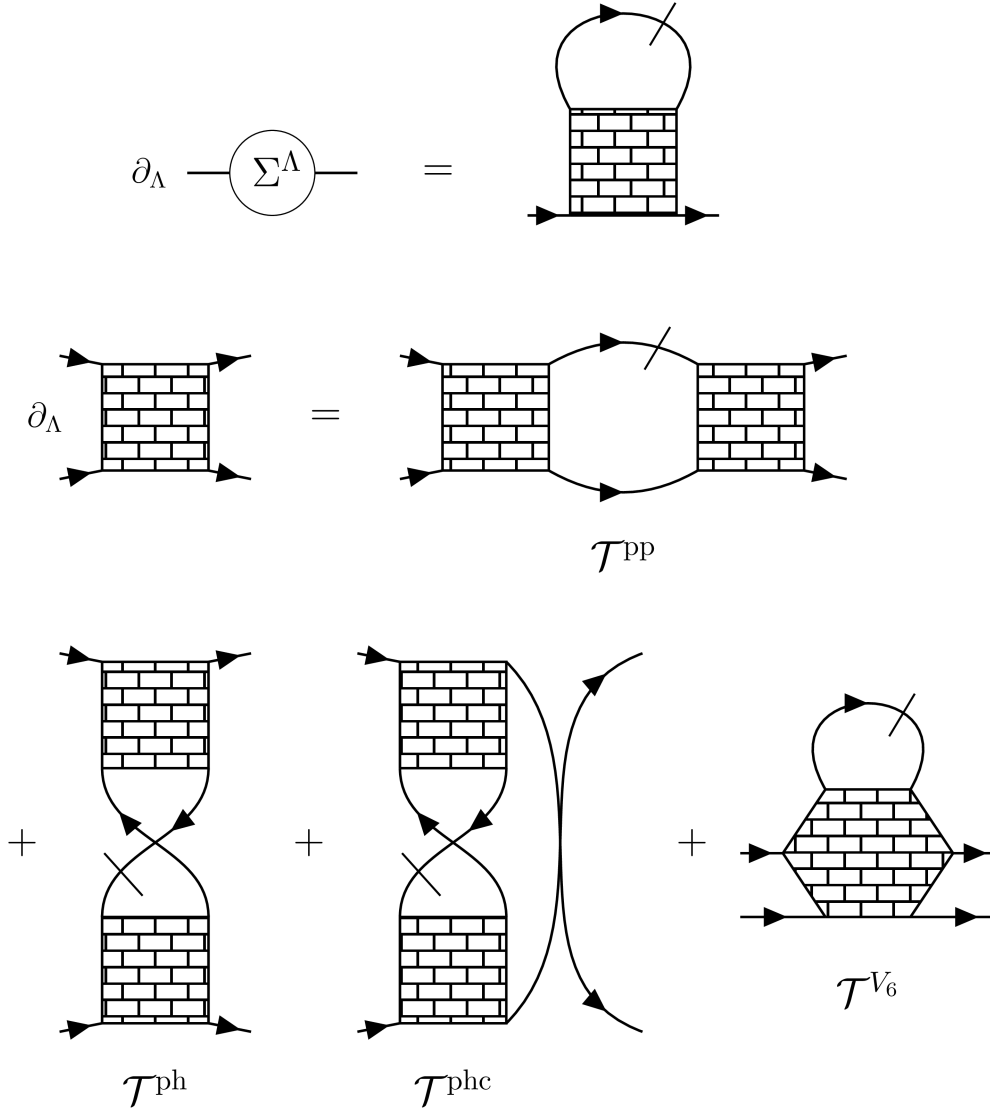


Figure 1.2: Diagrammatic representation of self-energy and vertex flow equations, Eqs. (1.25) and (1.23). The internal line with a cut refers to the single-scale propagator  $S^\Lambda$ . For the vertex equation, center and bottom rows, the fermionic internal lines accounts for the definitions (1.30), *i.e.* combinations of propagator  $G^\Lambda$  and single-scale prop.  $S^\Lambda$ .

the fulfilment of the symmetries of the action. Besides these requirements, there is a remaining arbitrariness in the  $\Lambda$ -dependence of  $G_0^\Lambda$  that one can exploit for convenience. In this thesis, when discussing the specific  $\Lambda$ -dependence of  $G_0^\Lambda$  we use the term *flow scheme*.

The specific choice of the flow scheme, and in particular the value  $G_0^{\Lambda_{\text{ini}}}$ , determines the initial condition for the self-energy  $\Sigma^{\Lambda_{\text{ini}}}$  and the vertex  $V^{\Lambda_{\text{ini}}}$ . For our scope, we introduce two classes of flow schemes, depending on the initial value  $G_0^{\Lambda_{\text{ini}}}$  leading to *correlated* or *uncorrelated* initial conditions. First, we analyze the case of an uncorrelated starting point, when  $\Gamma^{\Lambda_{\text{ini}}}[\psi, \bar{\psi}]$  does not include fluctuations at all. For instance, momentum and frequency cutoff [20], temperature flow [56], and interaction scheme [60] belong to this class. While the physical meaning of the parameter  $\Lambda$  varies for different schemes, this category shares the starting condition  $G_0^{\Lambda_{\text{ini}}} = 0$ . In this case, at  $\Lambda_{\text{ini}}$  the path integral (1.10) leads to the initial values for the self-energy and the vertex

$$\Sigma^{\Lambda_{\text{ini}}}(k) = 0, \quad (1.31a)$$

$$V_{\sigma_1, \sigma_2, \sigma_3, \sigma_4}^{\Lambda_{\text{ini}}}(k_1, k_2, k_3) = U[\delta_{\sigma_1, \uparrow} \delta_{\sigma_2, \downarrow} \delta_{\sigma_3, \uparrow} \delta_{\sigma_4, \downarrow} + \delta_{\sigma_1, \downarrow} \delta_{\sigma_2, \uparrow} \delta_{\sigma_3, \downarrow} \delta_{\sigma_4, \uparrow} - \delta_{\sigma_1, \downarrow} \delta_{\sigma_2, \uparrow} \delta_{\sigma_3, \uparrow} \delta_{\sigma_4, \downarrow} - \delta_{\sigma_1, \uparrow} \delta_{\sigma_2, \downarrow} \delta_{\sigma_3, \downarrow} \delta_{\sigma_4, \uparrow}], \quad (1.31b)$$

$$V^{(n)\Lambda_{\text{ini}}}(k_1, \dots, k_{n-1}) = 0, \quad n \geq 6. \quad (1.31c)$$

Moreover, due to the approximation  $\mathcal{T}^{V_6} \simeq 0$ , the higher order vertices  $V^{(n)\Lambda}$ , for  $n \geq 6$ , are completely neglected during the flow; this approximation restricts the calculations to the weak-to-intermediate coupling regime [61], making inaccessible strong coupling physics. In this thesis, unless specified, we use the nomenclature 'fRG' in connection to the case of an uncorrelated starting condition.

In the second class of flow schemes the function  $G_0^{\Lambda_{\text{ini}}}$  is nonzero and allows for an exactly solvable effective action  $\Gamma^{\Lambda_{\text{ini}}}[\psi, \bar{\psi}]$  containing already correlation effects. The possibility for a correlated starting point has been analyzed in Refs. [53, 62], and will be addressed addressed in the last part of this chapter, where we introduce the DMF<sup>2</sup>RG. In this case, the initial conditions (1.31) are no longer true, and the effects of higher order vertices are included, for instance in DMF<sup>2</sup>RG, at the local level by the DMFT, mitigating the consequences of the truncation  $\mathcal{T}^{V_6} \simeq 0$ .

### 1.1.3 Vertex properties and flow equations

Since the two-particle vertex function is a key mathematical object throughout this thesis, we discuss in this section a few specific properties that are needed later on. We first underline the symmetries that reduce the number of independent components of the vertex; these are: U(1) charge, SU(2) spin and the crossing symmetries. The crossing symmetry is a consequence of the Pauli principle, indeed, the exchange of two derivatives in (1.8) with respect to the same field  $\psi$  (or  $\bar{\psi}$ ) leads to a sign change. By applying this symmetry to the vertex function we obtain the following relation

$$V_{\sigma_1, \sigma_2, \sigma_3, \sigma_4}^\Lambda(k_1, k_2, k_3) = V_{\sigma_2, \sigma_1, \sigma_4, \sigma_3}^\Lambda(k_2, k_1, k_1 + k_2 - k_3). \quad (1.32)$$

Regarding, instead, the SU(2) spin symmetry, the vertex function  $V_{\sigma_1, \sigma_2, \sigma_3, \sigma_4}^\Lambda(k_1, k_2, k_3)$  consists of 16 spin components, that are not independent. In fact, when three spins are equal, e.g.  $\sigma_1 = \sigma_2 = \sigma_3 \neq \sigma_4$ , or when  $(\sigma_1 = \sigma_2) \neq (\sigma_3 = \sigma_4)$  with  $\sigma_1 = \uparrow, \downarrow$ , the spin conservation is violated; hence, the relative 10 components of the vertex are zero.

We can further reduce the remaining 6 components as a function of  $V_{\uparrow\downarrow\uparrow\downarrow}^\Lambda(k_1, k_2, k_3)$  only [54] by using  $V_{\uparrow\uparrow\uparrow\uparrow}^\Lambda = V_{\downarrow\downarrow\downarrow\downarrow}^\Lambda$ ,  $V_{\uparrow\uparrow\downarrow\downarrow}^\Lambda = V_{\downarrow\downarrow\uparrow\uparrow}^\Lambda$ ,  $V_{\uparrow\downarrow\uparrow\downarrow}^\Lambda = V_{\downarrow\uparrow\downarrow\uparrow}^\Lambda$ ,

$$\begin{aligned} V_{\uparrow\uparrow\uparrow\uparrow}^\Lambda(k_1, k_2, k_3) &= V_{\uparrow\downarrow\uparrow\downarrow}^\Lambda(k_1, k_2, k_3) \\ &\quad - V_{\uparrow\downarrow\uparrow\downarrow}^\Lambda(k_1, k_2, k_1 + k_2 - k_3), \end{aligned} \quad (1.33)$$

$$V_{\uparrow\downarrow\downarrow\uparrow}^\Lambda(k_1, k_2, k_3) = -V_{\uparrow\downarrow\uparrow\downarrow}^\Lambda(k_1, k_2, k_1 + k_2 - k_3). \quad (1.34)$$

Note that it is not possible to write all components as functions of  $V_{\uparrow\uparrow\uparrow\uparrow}^\Lambda$  or of combinations like the charge and magnetic components  $V_{c,m} = V_{\uparrow\uparrow\uparrow\uparrow}^\Lambda \pm V_{\uparrow\downarrow\uparrow\downarrow}^\Lambda$  [54].

Now we are able to rewrite the fRG equations [33] in terms of the component  $V^\Lambda \equiv V_{\uparrow\downarrow\uparrow\downarrow}^\Lambda$  only

$$\partial_\Lambda V^\Lambda(k_1, k_2, k_3) = \mathcal{T}^{\text{pp}}(k_1, k_2, k_3) + \mathcal{T}^{\text{ph}}(k_1, k_2, k_3) + \mathcal{T}^{\text{phc}}(k_1, k_2, k_3), \quad (1.35a)$$

where

$$\mathcal{T}^{\text{pp}}(k_1, k_2, k_3) = - \int_p \mathcal{P}_{\text{pp}}^\Lambda(k_1 + k_2, p) V^\Lambda(k_1, k_2, k_1 + k_2 - p) V^\Lambda(k_1 + k_2 - p, p, k_3), \quad (1.35b)$$

$$\begin{aligned} \mathcal{T}^{\text{ph}}(k_1, k_2, k_3) = \int_p \mathcal{P}_{\text{ph}}^\Lambda(k_3 - k_1, p) & \left\{ 2V^\Lambda(k_1, k_3 - k_1 + p, k_3) V^\Lambda(p, k_2, k_3 - k_1 + p) \right. \\ & - V^\Lambda(k_1, k_3 - k_1 + p, p) V^\Lambda(p, k_2, k_3 - k_1 + p) \\ & \left. - V^\Lambda(k_1, k_3 - k_1 + p, k_3) V^\Lambda(k_2, p, k_3 - k_1 + p) \right\}, \quad (1.35c) \end{aligned}$$

$$\mathcal{T}^{\text{phc}}(k_1, k_2, k_3) = - \int_p \mathcal{P}_{\text{ph}}^\Lambda(k_2 - k_3, p) V^\Lambda(k_1, k_2 - k_3 + p, p) V^\Lambda(p, k_2, k_3). \quad (1.35d)$$

that, together with the self-energy flow equation

$$\partial_\Lambda \Sigma^\Lambda(k) = \int_p S^\Lambda(p) [2V^\Lambda(k, p, p) - V^\Lambda(k, p, k)], \quad (1.36)$$

constitutes a closed set of differential equations. The functions  $\mathcal{P}_{\text{pp}}^\Lambda$  and  $\mathcal{P}_{\text{ph}}^\Lambda$  are defined in Eqs. (1.30).

### 1.1.4 Hubbard model: instabilities at weak coupling

In this section, we summarize on previous selected applications of the fRG equations to the 2D Hubbard model and the approximations involved. Starting the equations from an initial scale  $\Lambda_{\text{ini}}$ , the flow has to be stopped before the vertex diverges at the scale  $\Lambda_{\text{cri}}$ , named critical scale, and by looking at the dominant interaction, which governs the tendency towards a specific order, one can reconstruct the phase diagram of the system. This procedure is known as *instability analysis* [20]. The physical meaning of the critical scale  $\Lambda_{\text{cri}}$  varies according to the chosen flow scheme.

In the context of the instability analysis, the functional RG methods were first applied by Halboth and Metzner [25], Honerkamp *et al.* [26] and Zanchi and Schulz [27, 28],

the latter by using the Polchinski RG equations. Away from half-filling, a  $d$ -wave pairing instability, driven by antiferromagnetic fluctuations, has been found at weak to moderate coupling, showing that the interplay between magnetism and superconductivity is captured by the Hubbard model. In this way, the fRG method showed its suitability in the unbiased treatment of channel competitions, and in particular in the application of the Hubbard model, at least for weak interaction. Over the years the fRG calculations have been improved and extended [55, 37, 63, 33, 35]. For instance, Baier *et al.* [37] showed, in the context of the fRG, that the inclusion of the order parameter fluctuations restores the symmetric solution at finite temperature in accordance with the Mermin-Wagner theorem.

Before discussing the improvements of the vertex parametrization in the flow equations, we illustrate the superconducting instability as seen by the flow equation by selecting a more recent calculation performed by Eberlein and Metzner [35], shown in Fig. 1.3. This figure shows the flows of the magnetic and  $d$ -wave pairing channels; the latter is written in terms of amplitude and phase coupling functions [35]. A frequency cutoff has been used and, hence, the  $\Lambda$  parameter can be interpreted as an energy scale. At the beginning of the flow, *i.e.*, for large values of  $\Lambda$ , only one-loop diagrams contribute to the flow [61] and the magnetic channel is the leading interaction. In the intermediate part of the flow, where also nested loop diagrams [61] are generated, the effective magnetic interaction generates a  $d$ -wave channel which diverges at the critical scale. This picture supports the idea of  $d$ -wave superconductivity as spin fluctuation driven phenomenon. Moreover, the figure shows also the continuation of the flow towards the symmetry broken phase, below the critical scale, where the vertex and the self-energy acquire anomalous contributions.

An important topic in this thesis is, however, the role of the frequency dependence of the vertex function. The numerical solution of the vertex flow equation is challenging and further approximations on the momentum and frequency dependence are necessary. In Ref. [55], Honerkamp and Salmhofer derived the flow for a static, *i.e.* frequency independent, vertex while keeping all the momentum dependence. The momentum dependence of the vertex has been studied since the first application of the fRG. On the other hand, the role of the frequency dependence has been first analyzed for the single impurity Anderson model (SIAM) by Karrasch *et al.* [29], who suggested that the frequency dependence is *separable*, *i.e.* each channel depends only on a particular combi-

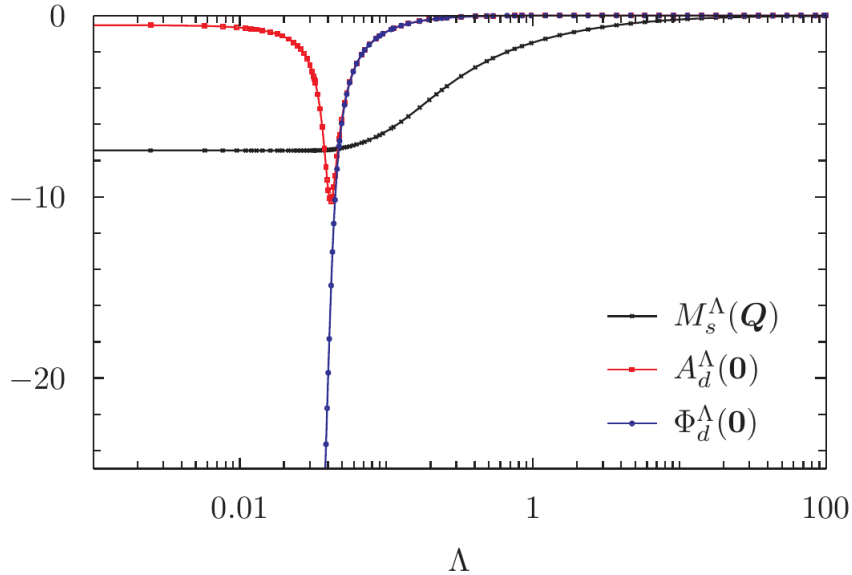


Figure 1.3: Flow of magnetic and  $d$ -wave (amplitude and phase modes) pairing channels. Figure taken from Ref. [35].

nation of two frequencies, depending on the relative channel. Regarding the 2D Hubbard model, the same approximate treatment of the vertex frequency dependence has been used in Ref. [34], based on a decomposition into magnetic, charge and pairing channels. Although simplified, this frequency dependence strongly affects the critical scales and also other physical quantities like the magnetic and pairing susceptibilities. Moreover, Husemann and Salmhofer [34] refined the decomposition by introducing the dependence on the two remaining frequencies, noticing a minor impact on the critical scale. At the same time, Uebelacker and Honerkamp [64] derived and solved the flow for both the frequency dependences of the vertex and the self-energy, but with a rough frequency grid involving only 10 points.

In Chapter 2, we analyze the role of the vertex frequency dependence with a high resolution and without any further simplifying assumption, as published in [65]. We show that a *nonseparable* frequency dependence appears already at moderate coupling; in fact, the vertex acquires a strong dependence on the two remaining frequencies, that can be explained by simple diagrams.

## 1.2 Dynamical mean field theory: strong correlation effects

In this section we introduce the dynamical mean field theory (DMFT), a method that is able to capture strong correlation effects, at least at the local level. Here we do not provide a detailed introduction to the method, which can be found in Refs. [42, 66], but rather an overview that addresses its physical aspects and prepares the way for the last part of this chapter, where we discuss the combination of DMFT with the fRG.

Metzner and Vollhardt [40] proposed a consistent way of performing the limit of infinite dimensions  $d \rightarrow \infty$  in the Hubbard Model. In this limit, to define a finite noninteracting density of states, the hopping amplitude should scale as  $t = t^*/(2d)^{1/2}$  with  $t^*$  fixed. With this proper rescaling, Metzner and Vollhardt [40] found that for  $d \rightarrow \infty$  nontrivial correlation effects are present, and the skeleton expansion for the self-energy is local at any order. A few years later, Georges and Kotliar [41] showed that the Hubbard Model in infinite dimensions can be mapped onto a self-consistent impurity model (IM).

We first introduce the main approximation of DMFT, where the self-energy is constrained to be a local function. We then proceed with the consequent mapping onto an impurity model and show the DMFT self-consistent condition as the fundamental relation between the impurity and the original lattice model. The DMFT procedure becomes exact for  $d \rightarrow \infty$ ; in finite dimensions, the DMFT is an approximation but still includes all local correlations. Towards the end, we analyze the physical picture of the Hubbard model at half-filling as seen by the inclusion of strong local fluctuations.

### 1.2.1 Dynamical mean field

In this section we discuss the basic ideas of DMFT for the Hubbard model, defined by the Hamiltonian

$$\mathcal{H} = \sum_{i,j,\sigma} t_{ij} c_{i,\sigma}^\dagger c_{j,\sigma} + U \sum_i n_{i,\uparrow} n_{i,\downarrow}. \quad (1.37)$$

Here  $c_{i,\sigma}^\dagger$  ( $c_{i,\sigma}$ ) creates (annihilates) a fermion on site  $i$  with spin orientation  $\sigma$  ( $\uparrow$  or  $\downarrow$ ). The second term represents a local interaction, while in the first term  $t_{ij}$  refers to the hopping amplitude between lattice sites  $i$  and  $j$ .

The fundamental idea is to keep track of the *local* physics at each site, by reducing, in the smartest way, the lattice degrees of freedom. Hence, we consider the key quantity of DMFT, which is the *local* Green's function at the given lattice site  $i$ :

$$G_{ii}(\tau - \tau') \equiv -\langle \mathcal{T} c_{i,\sigma}(\tau) c_{i,\sigma}^\dagger(\tau') \rangle. \quad (1.38)$$

With this quantity, we do not concentrate on correlations at different sites but rather on correlations at different times,  $\tau$  and  $\tau'$ . In connection to this idea, we present the main approximation of the DMFT, *i.e.*, we approximate the self-energy to be a local function

$$\Sigma_{ij}(\omega) \approx \Sigma(\omega) \delta_{ij}, \quad (1.39)$$

In the limit of infinite dimensions  $d \rightarrow \infty$ , the self-energy is indeed local and the approximation (1.39) becomes exact [40, 67, 41].

To show the implication of the DMFT approximation (1.39) we consider the *skeleton* expansion for the self-energy. In this particular expansion for  $\Sigma_{ij}(\omega)$ , all the internal lines correspond to the full interacting fermionic propagator  $G_{ij}(\omega)$ . In this way, the self-energy can be seen as a functional of the Green's function  $\Sigma_{ij}(\omega) = \Sigma_{ij}^{\text{skel}}[\{G_{kl}\}]$  [42]. The Luttinger-Ward free energy  $\Phi[\{G_{kl}\}]$ , built from all vacuum-to-vacuum skeleton diagrams, obeys the relation [68]

$$\Sigma_{ij}(\omega) = \frac{\delta \Phi}{\delta G_{ij}(\omega)}. \quad (1.40)$$

When the DMFT approximation (1.39) is taken into account, the relation (1.40) implies that the Luttinger-Ward and the  $\Sigma^{\text{skel}}$  functionals depend only on the local Green's function  $G_{ii}$ :  $\Phi = \sum_i \phi[G_{ii}]$  and  $\Sigma^{\text{skel}}[G_{ii}]$ . As a consequence, it must be possible to generate  $\phi[G_{ii}]$  and  $\Sigma^{\text{skel}}[G_{ii}]$  from a purely local theory.

For our scope, we introduce the effective action of an impurity problem as

$$S_{\text{imp}}[\psi, \bar{\psi}] = -\frac{1}{\beta} \int_0^\beta d\tau \int_0^\beta d\tau' \sum_\sigma \bar{\psi}_\sigma(\tau) \mathcal{G}_0^{-1}(\tau - \tau') \psi_\sigma(\tau') + U \int_0^\beta d\tau n_\uparrow(\tau) n_\downarrow(\tau), \quad (1.41)$$

where  $\mathcal{G}_0$  plays the role of the bare Green's function for the action (1.41) and should not be confused with the bare Green's function of the lattice system.

The action (1.41) represents the dynamics of the impurity, which feels the presence of a dynamical external field through the function  $\mathcal{G}_0$ . We interpret, in this way,  $\mathcal{G}_0^{-1}(\tau - \tau')$  as a quantum generalisation of the Weiss effective field in the classical case, which is now a function of time and plays the role of a *dynamical mean-field* in which the impurity is embedded. For this reason,  $\mathcal{G}_0^{-1}$  is sometimes called *Weiss field*. As discussed in the next section, the impurity action (1.41) can be solved numerically for a given function  $\mathcal{G}_0$ . We are also able to define the interacting Green's function of the impurity  $G_{\text{imp}}(\tau - \tau') \equiv -\langle \psi_\sigma(\tau) \bar{\psi}_\sigma(\tau') \rangle$ , as described by the model (1.41) and the relative self-energy of the impurity

$$\Sigma_{\text{imp}}(\omega) = \mathcal{G}_0^{-1}(\omega) - G_{\text{imp}}^{-1}(\omega). \quad (1.42)$$

It is possible to establish a connection between the original lattice system and the impurity problem through their respective free energies  $\Omega$  and  $\Omega_{\text{imp}}$  [42, 69], when the DMFT approximation (1.39) is taken into account. In this case, the two models have equivalent free energies if the following condition is satisfied

$$\int_{\mathbf{k}} \frac{1}{i\omega + \mu - \epsilon_{\mathbf{k}} - \Sigma(\omega)} = [\mathcal{G}_0^{-1}(\omega) - \Sigma(\omega)]^{-1}, \quad (1.43)$$

where the notation  $\int_{\mathbf{k}} = \int \frac{d\mathbf{k}}{(2\pi)^2}$  is understood. Note that in Eq. (1.43) the left-hand side is the local Green's function,  $G_{ii}(\omega) = \int_{\mathbf{k}} G(\mathbf{k}, \omega)$ , of the lattice system and equals the impurity Green's function on the right-hand side. The relation (1.43) is also called DMFT self-consistency condition. With self-consistency, we mean the convergence of the following loop:

1. Start with a local initial guess for the self-energy.
2. By inverting Eq. (1.43), compute the Weiss field  $\mathcal{G}_0$ .
3. Solve the impurity model (1.41) with  $\mathcal{G}_0$  given in point 2 with the help of a numerical solver, compute the impurity self-energy and go back to point 2.

Once self-consistency is reached for a given accuracy, such an iterative procedure, called DMFT self-consistency loop, provides the DMFT solution for the lattice system. The IM that fulfils the DMFT loop is sometimes called self-consistent IM. Thanks to the mapping onto the impurity model and the self-consistency procedure, the DMFT captures, at the local level, strong correlation effects.

Before proceeding, here we mention a few cases of the Hubbard model where the DMFT solution becomes exact. First, the *non-interacting* case  $U = 0$ , since the action (1.41) gives  $\Sigma(\omega) = 0$  and the self-consistency condition (1.43) implies  $G_{ii}(\omega) = \mathcal{G}_0(\omega)$ . Then, the *atomic limit*  $t_{ij} = 0$ , representing a collection of independent, hence uncorrelated, sites, where Eq. (1.43) gives  $\mathcal{G}_0^{-1}(\omega) = i\omega + \mu$ . As already discussed above, another limit where the DMFT becomes exact is the infinite dimension limit  $d \rightarrow \infty$  [40, 41].

So far we addressed the key ideas of the DMFT with the introduction of an impurity model able to capture the local physics of the full lattice system. In the next part, we discuss the specific method we use in order to solve the impurity problem with the help of exact diagonalization.

## 1.2.2 Anderson impurity model

An important step in the calculation of the DMFT self-consistency loop is represented by the solution the impurity model, defined by the action (1.41), which can be treated numerically with a variety of techniques. Examples are: quantum Monte Carlo (QMC) [70], iterated perturbation theory (IPT) [41], numerical renormalization group (NRG) [71] and exact diagonalization (ED) [72]. In our calculations we use the ED. This method requires a Hamiltonian formalism equivalent to the effective action (1.41). For this scope we consider the Anderson impurity model (AIM), defined by the following Hamiltonian

$$\mathcal{H}_{\text{AIM}} = \mathcal{H}_{\text{atom}} + \mathcal{H}_{\text{bath}} + \mathcal{H}_{\text{coupling}}. \quad (1.44)$$

The first term describes the interaction at the impurity

$$\mathcal{H}_{\text{atom}} = U n_{\uparrow} n_{\downarrow}, \quad (1.45)$$

here  $n_{\sigma} = c_{\sigma}^{\dagger} c_{\sigma}$ , and  $c_{\sigma}^{\dagger}$  ( $c_{\sigma}$ ) being creation (annihilation) operator of the impurity. The other two terms in the Hamiltonian (1.44) describe the properties of the bath

$$\mathcal{H}_{\text{bath}} = \sum_{\mathbf{k}, \sigma} \tilde{\epsilon}_{\mathbf{k}} a_{\mathbf{k}, \sigma}^{\dagger} a_{\mathbf{k}, \sigma}, \quad (1.46a)$$

and the coupling between the bath and the impurity

$$\mathcal{H}_{\text{coupling}} = \sum_{\mathbf{k},\sigma} V_{\mathbf{k}}(a_{\mathbf{k},\sigma}^\dagger c_\sigma + c_\sigma^\dagger a_{\mathbf{k},\sigma}), \quad (1.46b)$$

where the operators  $(a_{\mathbf{k},\sigma}, a_{\mathbf{k},\sigma}^\dagger)$  together with the dispersion  $\tilde{\epsilon}_{\mathbf{k}}$  defines the bath as a “conduction band”.  $V_{\mathbf{k}}$  represents a hopping amplitude between the impurity and the bath. The parameters  $\tilde{\epsilon}_{\mathbf{k}}$  and  $V_{\mathbf{k}}$  are also called *Anderson parameters*.

Similar to a mean field calculation, the single site feels the effect of the other sites through a bath governed by the Hamiltonian (1.46). The main difference with a static mean field is that the bath is fully dynamical and, hence, possesses non-trivial time-dependent correlations.

The connection with the impurity model in the DMFT is revealed when considering the action formalism for the AIM. The bath degrees of freedom can be integrated out, leading to the following effective action for the impurity [73, 74]

$$S_{\text{AIM}}[\psi, \bar{\psi}] = -\frac{1}{\beta} \int_0^\beta d\tau \int_0^\beta d\tau' \sum_{\sigma} \bar{\psi}_{\sigma}(\tau) (-\partial_{\tau'} + \mu - \Delta(\tau - \tau')) \psi_{\sigma}(\tau') + U \int_0^\beta d\tau n_{\uparrow}(\tau) n_{\downarrow}(\tau). \quad (1.47)$$

Here we introduced the so-called *hybridization function*

$$\Delta(\omega) = \sum_{\mathbf{k}} \frac{|V_{\mathbf{k}}|^2}{i\omega - \tilde{\epsilon}_{\mathbf{k}}}, \quad (1.48)$$

which results from the integration of bath degrees of freedom. The two actions (1.47) and (1.41) are equivalent with

$$\mathcal{G}_0^{-1}(\omega) = i\omega + \mu - \Delta(\omega). \quad (1.49)$$

We use the ED by following the Ref. [72]. There, the continuous energy spectrum  $\tilde{\epsilon}_{\mathbf{k}}$  is replaced by a finite number  $n_s$  of energy levels:  $\tilde{\epsilon}_l$ , with  $l = 1, \dots, n_s$ . In the same way, the continuous function  $V_{\mathbf{k}}$  is replaced by the parameters  $V_l$ . The strict self-consistency can only be obtained in the limit  $n_s \rightarrow \infty$ . The representation of the hybridization

function now has the form

$$\Delta_{\text{ED}}(\omega) = \sum_{l=1}^{n_s} \frac{|V_l|^2}{i\omega - \tilde{\epsilon}_l}. \quad (1.50)$$

Caffarel and Krauth [72] proposed a way to determine  $\tilde{\epsilon}_l$  and  $V_l$  by minimizing the difference between Eqs. (1.48) and (1.50). We calculate the Green's function and the vertex of the impurity by using the Lehmann representation; the impurity self-energy is then determined by Eq. (1.42). In Appendix B, we provide few more details in the application of the ED method to DMFT calculations.

### 1.2.3 Hubbard model at half-filling: Mott transition vs Antiferromagnetism

In this section, we discuss the physical picture of the half-filled Hubbard model in infinite dimensions as seen by DMFT. As a matter of fact, for  $d \rightarrow \infty$  the DMFT provides two solutions depending on whether we allow for spin symmetry breaking or not. In the first case, when we impose the symmetric solution with  $\Sigma_{\uparrow} = \Sigma_{\downarrow}$ , the DMFT shows a first order Mott transition [42]. In the second case, by modifying the DMFT procedure, introduced above, to allow for an antiferromagnetic symmetry broken solution, the DMFT shows a second order phase transition towards an antiferromagnetic state below the Néel temperature  $T_{\text{N}}$ .

The Mott metal-to-insulator (MIT) transition has been proposed by the Nobel laureate Nevill Mott in the 1950s [75, 76]. Certain materials, like  $\text{V}_2\text{O}_3$ , predicted to be conducting by the bandstructure theory, show a transition from a metallic to an insulating state due to strong correlation effects.

One of the successes of DMFT was to capture and to better understand the Mott physics [42]. When not allowing for symmetry breaking, the DMFT solution of the Hubbard model at half-filling shows a first order metal-to-insulator transition driven by the coupling strength. From Ref. [42], we take a picture of the Mott transition as observed by DMFT, see Fig. 1.4. In the following, we describe the physical properties characterizing the metallic and the insulating state. In the weak coupling regime, the system is a *Fermi liquid*. This state is characterized by the presence of fermionic quasi-particles, whose quasi-particle weight  $Z$  is  $\mathbf{k}$ -independent and  $0 < Z < 1$ . Hence, the system is in a metallic state. When we increase the coupling  $U$ , for some critical value

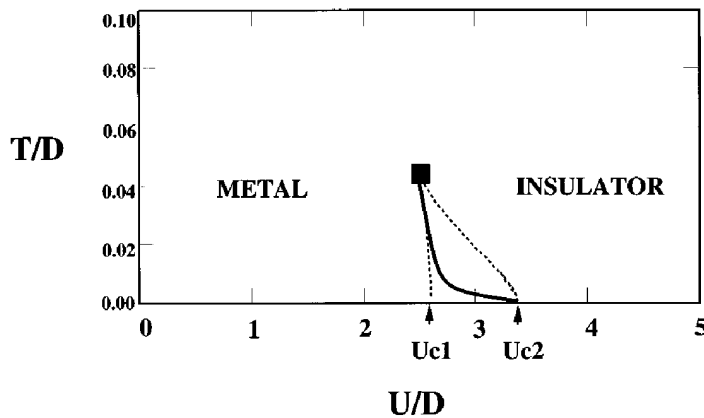


Figure 1.4: Mott transition as observed in DMFT. Figure taken from Ref.[42].

$U_c$ , we encounter a first order transition towards an *insulating state*, with a gap in the single particle energy spectrum. This state is characterized by the presence of *unscreened local moments*, which obey the Curie law for the local spin susceptibility,  $\sum_{\mathbf{q}} \chi_{\mathbf{q}} \sim 1/T$ .

However, the picture changes when we allow for spontaneous symmetry breaking (SSB) in the DMFT calculation. In this case, the solution predicts a second order transition towards an *antiferromagnetic long range order* at a finite Néel temperature [42]. Hence, applied to low dimensional systems, ( $d \leq 2$ ), the DMFT approximation violates the Mermin-Wagner theorem [39]. A sketch of the phase diagram at half-filling  $n = 1$  and  $t' = 0$  is reported in Fig. 1.5 taken from Ref. [12]. With a nearest neighbor hopping only, strong antiferromagnetic correlations lead to a transition at finite temperature for any finite value of the coupling  $U$ . With a finite  $t'$ , the antiferromagnetic order appears only above a certain value of the coupling  $U_c$ , which separates the ordered state from the Fermi liquid solution at weak coupling. However, we have different properties regarding the antiferromagnetic solutions in the weak and in the strong coupling regimes. At weak coupling, the antiferromagnetic state is determined by the perfect nesting of the Fermi surface and the Néel temperature shows an exponential behaviour as a function of the coupling. In this regime, the antiferromagnetic state is preferred to the paramagnetic one due to a lower potential energy [77, 50] and is named *Slater* antiferromagnet. In the strong coupling regime, the antiferromagnetic solution is determined by an effective *Heisenberg* interaction and is preferred due to a lower kinetic energy. The Néel tempera-

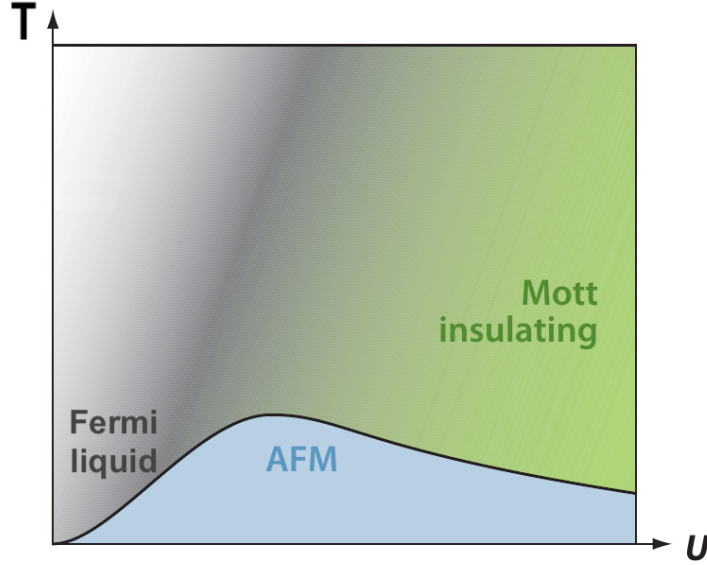


Figure 1.5: Sketch of the solution of DMFT with antiferromagnetic symmetry breaking at half-filling  $n = 1$  and  $t' = 0$ . Figure taken from Ref.[12].

ture shows the behaviour  $T_N \approx J \equiv 4t^2/U$ , where  $J$  is the Heisenberg coupling constant between spins.

When considering the finite dimensional case, the DMFT solution becomes an approximation. In finite dimensions, the two DMFT solutions described above do not qualitatively change and constitute, at this level, our starting point in understanding the physics in two dimensions. We point out that the paramagnetic solution in 2D is quite important in our calculations as it determines the starting point for the DMF<sup>2</sup>RG calculation.

Although with different properties, the antiferromagnetic solution extends away from half-filling, as we will see in Chapter 3 for the two-dimensional case, where we analyze the nonlocal spin correlation function.

#### 1.2.4 Vertex function and ladder-DMFT

In this section, we discuss the two-particle vertex in DMFT [54]. The DMFT loop, as presented above, involves the calculation of single-particle quantities, like the local

Green's function and the local self-energy, while the higher order vertex functions are not involved in the calculation. On the other hand, many physical observables, such as magnetic properties and collective excitation spectra, require the explicit calculation of two-particle quantities. Besides this, the DMFT vertex function [54] is also a key ingredient for diagrammatic extensions of the DMFT [44], e.g., the DMF<sup>2</sup>RG method introduced later in this chapter and applied to the Hubbard model in Chapter 4. In this section we focus on the definition of the local DMFT vertex and how to generate a momentum dependence with a ladder summation.

We define the DMFT vertex function as the local vertex of the self-consistent impurity model [42, 54]

$$V_{\sigma_1, \sigma_2, \sigma_3, \sigma_4}(\nu_1, \nu_2, \nu_3) \equiv V_{\sigma_1, \sigma_2, \sigma_3, \sigma_4}^{\text{imp}}(\nu_1, \nu_2, \nu_3). \quad (1.51)$$

The notation of the vertex function follows Fig. 1.1. To be precise, after having reached the convergence in the DMFT loop, as introduced in the previous sections, we calculate the vertex function of the IM associated with the self-consistent bath. As stated above, the DMFT self-energy is exact in the limit of infinite dimensions. The vertex function (1.51) coincides with the local vertex in infinite dimensions. In this limit, the vertex differs from the impurity vertex (1.51) only for special choices of momenta. The details on the computation of the impurity vertex with a numerical solver are reported in Appendix B.

Here, we report a few properties of the frequency structure of the DMFT vertex for the 2D Hubbard model, relevant for the DMF<sup>2</sup>RG calculations presented in Chapter 4. A detailed study of the frequency dependence of the DMFT vertex in the 2D Hubbard model can be found in Ref. [54].

In Fig. 1.6 we show the vertex  $V_\omega(\nu_1, \nu_2) \equiv V_{\uparrow\downarrow\uparrow\downarrow}(\nu_1, \nu_2, \omega + \nu_1)$  as a function of the two incoming frequencies  $\nu_1$  and  $\nu_2$  for fixed particle-hole frequency  $\omega = \nu_3 - \nu_1 = 0$  at half-filling  $n = 1$  and  $t' = 0$ . In this case, due to particle-hole symmetry, the DMFT self-energy is purely imaginary and the DMFT vertex is real. On the left, the vertex is shown in the intermediate coupling regime  $U = 4t$  at temperature  $T = 0.31t$ . The vertex shows pronounced structures both on the diagonals and on the central cross that extend to large frequencies; these structures are explained by perturbative contributions in Ref. [54], at second order for the diagonals, and at third order for the central cross. A nonperturbative and general understanding of the frequency structures can be found

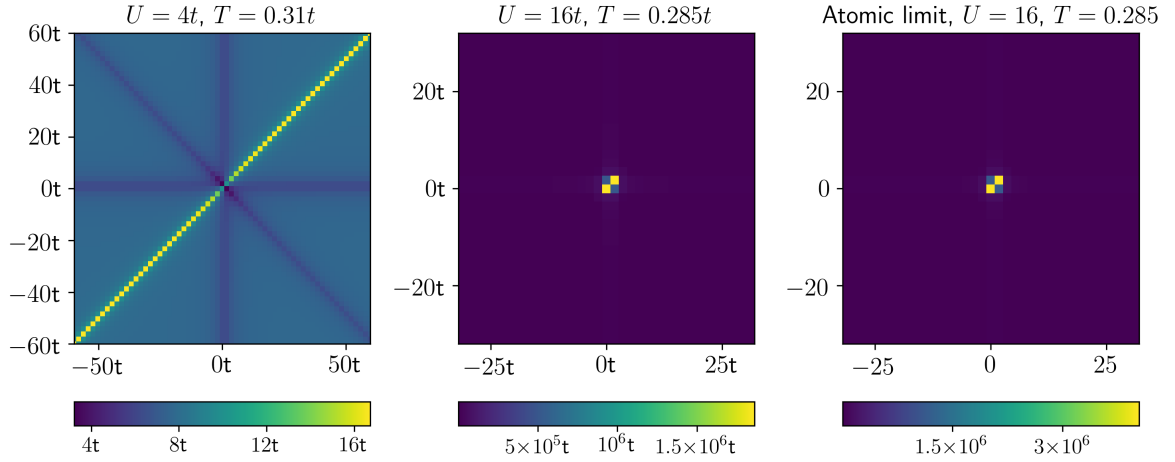


Figure 1.6: Vertex function  $V_\omega(\nu_1, \nu_2)$  with  $\omega = 0$  at half-filling  $n = 1$  and  $t' = 0$ . Left: DMFT vertex for  $U = 4t$ ,  $T = 0.31t$ . Center: DMFT vertex for  $U = 16t$ ,  $T = 0.285t$ . Right: Atomic limit Vertex function for  $U = 16$ ,  $T = 0.285t$ .

in Ref. [31].

At the center of Fig. 1.6, we show the vertex in the Mott regime at strong coupling  $U = 16t$  and temperature  $T = 0.285t$ . Here the structures differ from the intermediate coupling case; the most pronounced one is strongly localized and reaches values of the order  $\sim 10^6$ . To understand the origin of this effect, we plot on the right of Fig. 1.6 the vertex in the atomic limit, defined with  $t = 0$ , for the coupling value  $U = 16$ . The exact formulae for the vertex and the self-energy in the atomic limit can be found in Refs. [78, 79] at particle-hole symmetry, and in Ref. [80] for the general case. The atomic limit vertex, on the right, captures the frequency structure characteristic of the Mott regime. For a better understanding we introduce the following function [54]

$$\begin{aligned} \chi_{\omega, \sigma_1 \sigma_2}(\nu_1, \nu_2) = & -\beta G(\nu_1) G(\nu_1 + \omega) \delta_{\nu_1 \nu_2} \delta_{\sigma_1 \sigma_2} \\ & - G(\nu_1) G(\nu_1 + \omega) V_{\sigma_1, \sigma_2, \sigma_1, \sigma_2}(\nu_1, \nu_2, \omega + \nu_1) G(\nu_2) G(\nu_2 + \omega), \end{aligned} \quad (1.52)$$

where, in this context,  $G(\nu)$  is the local DMFT Green's function. The function defined as  $\chi_\omega = \sum_{\nu_1, \nu_2} \chi_{\omega, \uparrow \uparrow}(\nu_1, \nu_2) - \chi_{\omega, \uparrow \downarrow}(\nu_1, \nu_2)$  is the local spin susceptibility [54]. At strong

coupling, its diagonal part  $\nu_1 = \nu_2$  for  $\omega = 0$  follows the Curie-Weiss law  $\chi_{\omega=0} \sim \beta U^{-2}$  [42, 54]. Since the aim is to give insights on the localized structure in Fig. 1.6, referring to the function  $V_{\uparrow\downarrow\uparrow\downarrow}$ , we consider in Eq. (1.52) the combination  $\sigma_1 = \uparrow$ ,  $\sigma_2 = \downarrow$  and frequencies  $\nu_1 = \nu_2 = \pi T$ ,  $\omega = 0$ . From the behaviour of  $\chi_{\omega=0}$  we can extract the estimated proportionality of the vertex by supposing that the low frequency Green's function obeys the atomic limit formula  $G(\pi T) \sim \beta^{-1} U^{-2}$  (for  $T \ll U$ )

$$V_{\omega=0, \text{dmft}}(\nu_1 = \pi T, \nu_2 = \pi T) \sim \beta^5 U^6, \quad (1.53)$$

which is the leading behaviour of the vertex function in the atomic limit for large  $U$  and low temperatures [78].

Hence, the central structure of the DMFT vertex is a consequence of the insulating Green's function and the Curie-Weiss law for the susceptibility. This law is, however, connected with the formation of long-living magnetic moments, a characteristic of the Mott insulating phase. As a consequence, the low frequency component of the vertex (1.53) strongly diverges in the zero temperature limit  $\beta \rightarrow \infty$ .

## 1.3 DMF<sup>2</sup>RG: Combining the fRG with the DMFT

In the previous section, we introduced the DMFT as a method able to include local correlations nonperturbatively. As explained, in the limit of infinite lattice dimensions, where correlations are local [40], the DMFT becomes exact. In finite dimension the DMFT is an approximation, since it cannot take into account nonlocal correlations, which become crucial in low-dimensional systems, for instance, in the 2D Hubbard model considered in this thesis. Fortunately, the DMFT formalism allows for extensions that include, in different ways, nonlocal correlation effects [43, 46, 44, 48]. Here we concentrate on the DMF<sup>2</sup>RG, which combines the DMFT with the fRG.

As explained in the previous sections, the truncation in the fRG together with the uncorrelated starting conditions (1.31) introduces important limitations, for instance, the inability to access the strong coupling regime. Taranto *et al.* [53] proposed for the first time the DMF<sup>2</sup>RG idea, a way to overcome this limitation by starting the fRG flow from the DMFT solution. This technique is able to combine the two main aspects of the parents' methods: the strong but *local* correlation effects of DMFT and the unbiased channel competition at the *nonlocal* level of the fRG.

In Chapter 4 we show the application of the DMF<sup>2</sup>RG to the 2D Hubbard model with a particular focus on the interplay between antiferromagnetic and superconducting fluctuations at strong coupling.

### 1.3.1 Formalism and implementation

In this section we formalize the idea of starting the fRG flow from the DMFT solution. This formalism, first introduced in Ref. [53], has been extended to general correlated starting points by Wentzell *et al.* [62].

To formalize the DMF<sup>2</sup>RG idea, we benefit from the derivation of the fRG given in the first part of this chapter. To fix the initial effective action  $\Gamma^{\Lambda_{\text{ini}}}[\psi, \bar{\psi}]$  in Wetterich's equation (1.16), we consider the function  $G_0^\Lambda(\omega, \mathbf{k})$ , whose  $\Lambda$ -dependence determines the initial condition. Its final value is always the bare Green's function,  $G^{\Lambda_{\text{fin}}}(\omega, \mathbf{k}) = G_0^{-1}(\omega, \mathbf{k}) = i\omega + \mu - \epsilon_{\mathbf{k}}$ , implying that the final solution for  $\Gamma^\Lambda[\psi, \bar{\psi}]$  is the full quantum effective action.

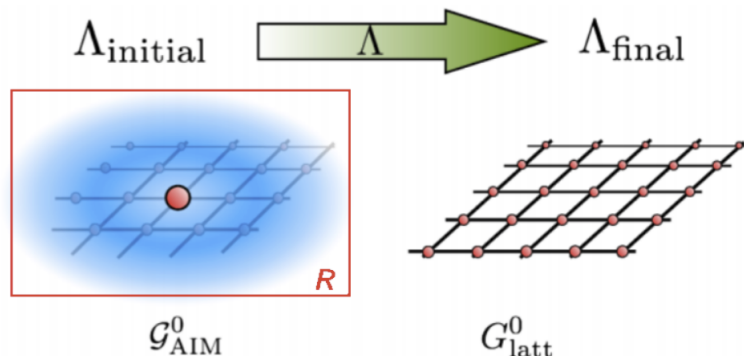


Figure 1.7: Graphical representation of DMF<sup>2</sup>RG idea. For  $\Lambda = \Lambda_{\text{ini}}$  we start from an impurity problem determined by the DMFT solution, while with the flowing of  $\Lambda$  we turn the lattice degrees of freedom on. Figure taken from [53].

To start from the DMFT solution, we can impose

$$G_0^{\Lambda_{\text{ini}}}(\omega, \mathbf{k}) = \mathcal{G}_0(\omega) \xrightarrow{\Lambda \rightarrow \Lambda_{\text{fin}}} G_0^{\Lambda_{\text{fin}}}(\omega, \mathbf{k}) = G_0(\omega, \mathbf{k}), \quad (1.54)$$

where  $\mathcal{G}_0(\omega)$  is the Weiss field determined by the DMFT solution of the lattice problem. In other words, we start from a  $\mathbf{k}$ -independent solution and turn on the nonlocal degrees of freedom during the flow. In Fig. 1.7 we show a graphical representation of Eq. (1.54). At the beginning of the flow, the  $G_0^\Lambda$  is local and each lattice site sees the others as an effective, time dependent, Weiss field. While solving the fRG flow, the lattice degrees of freedom are adiabatically turned on, restoring the bare lattice Green's function  $G_0$  at the end of the flow.

Let us discuss more on the implication of condition (1.54) to the action formalism of the fRG. At  $\Lambda_{\text{ini}}$  the action in the path integral (1.2) is  $S^{\Lambda_{\text{ini}}}[\psi, \bar{\psi}] = S_{\text{dmft}}[\psi, \bar{\psi}]$ , with

$$S_{\text{dmft}}[\psi, \bar{\psi}] = -\frac{1}{\beta} \int_0^\beta d\tau \int_0^\beta d\tau' \sum_{\mathbf{k}, \sigma} \bar{\psi}_{\mathbf{k}, \sigma}(\tau) \mathcal{G}_0^{-1}(\tau - \tau') \psi_{\mathbf{k}, \sigma}(\tau') + U \int_0^\beta d\tau \sum_i n_{\uparrow, i}(\tau) n_{\downarrow, i}(\tau). \quad (1.55)$$

Since the function  $\mathcal{G}_0$  is local, the action (1.55) decouples into a series of single site actions, each representing an impurity problem governed by the AIM action. As a consequence,

we write the resulting effective action as

$$\Gamma^{\Lambda\text{ini}}[\psi, \bar{\psi}] = \Gamma_{\text{dmft}}[\psi, \bar{\psi}], \quad (1.56)$$

which determines the initial condition for the fRG flow.

A comment on the meaning of  $\Gamma_{\text{dmft}}$  here is necessary. The DMFT procedure, as discussed in the previous sections, involves the calculation of the local self-energy  $\Sigma_{\text{dmft}}(\omega)$  and not of the full sequence of 1PI vertices that compose the effective action (1.56). As advertised in Section 1.2.4, here  $\Gamma_{\text{dmft}}[\psi, \bar{\psi}]$  is the effective action of the Anderson impurity model with a self-consistent Weiss field. Hence, for the 1PI functions of DMFT, at any order, we intend the *local* 1PI functions resulting from the self-consistent IM.

As in the fRG calculations, we concentrate on the flow of the vertex  $V^\Lambda(k_1, k_2, k_3)$  and of the self-energy  $\Sigma^\Lambda(k)$ , whose initial conditions can be determined by expanding Eq. (1.56)

$$\Sigma^{\Lambda\text{ini}}(\omega, \mathbf{k}) = \Sigma_{\text{dmft}}(\omega), \quad (1.57)$$

$$V^{\Lambda\text{ini}}(\omega_1, \omega_2, \omega_3, \mathbf{k}_1, \mathbf{k}_2, \mathbf{k}_3) = V_{\text{dmft}}(\omega_1, \omega_2, \omega_3), \quad (1.58)$$

where  $\Sigma_{\text{dmft}}$  is the self-energy of the DMFT and  $V_{\text{dmft}}$  is the local vertex of the self-consistent AIM.

The flow equations of the DMF<sup>2</sup>RG are formally identical to those of the fRG, Eq. (1.36) for the self-energy and Eq. (1.35a) for the vertex, with the difference that the function  $G_0^\Lambda$  must fulfil the property (1.54). We recall that Eqs. (1.36) and (1.35a) are derived by using explicitly SU(2) spin and U(1) charge symmetry relations; hence, like in the fRG case, the present formulation of the flow equations cannot access phases with SU(2) spin or U(1) charge symmetry breaking. Moreover, the underlying flow equations truncate the term  $\mathcal{T}^{\text{V}6}$ . We discuss later the effects of this truncation in DMF<sup>2</sup>RG compared to the conventional fRG.

To sum up, the DMF<sup>2</sup>RG calculation is composed by the following steps:

1. Find the DMFT solution of the lattice problem.
2. Extract the vertex function from the self-consistent AIM determined by point 1.
3. Solve the fRG flow by starting from  $\Sigma_{\text{dmft}}$  and  $V_{\text{dmft}}$ , with the function  $G_0^\Lambda$  following the property (1.54).

We briefly mention here the results of the application of this method that has been presented for the first time in Ref. [53], where Taranto *et al.* showed numerical results for the 2D Hubbard model at half-filling. In this case, the  $G_0^\Lambda$  function has been chosen as a linear interpolation between the Weiss field and the lattice bare Green's function

$$G_0^{\Lambda^{-1}}(\omega, \mathbf{k}) = \Lambda \mathcal{G}_0^{-1}(\omega) + (1 - \Lambda) G_0^{-1}(\omega, \mathbf{k}), \quad (1.59)$$

that automatically fulfils condition (1.54) when  $\Lambda_{\text{ini}} = 1$  and  $\Lambda_{\text{fin}} = 0$ . This relation can be rewritten in terms of the hybridization function  $\Delta(\omega) = i\omega + \mu - \mathcal{G}_0^{-1}(\omega)$ , and by using  $G_0^{-1}(\omega, \mathbf{k}) = i\omega + \mu - \epsilon_{\mathbf{k}}$ , as

$$G_0^{\Lambda^{-1}}(\omega, \mathbf{k}) = i\omega + \mu - \Lambda \Delta(\omega) - (1 - \Lambda) \epsilon_{\mathbf{k}}. \quad (1.60)$$

Here, the idea of the DMF<sup>2</sup>RG is more transparent. The hybridization function (1.48) represents the connection between the impurity and the bath. Hence, during the flow from  $\Lambda_{\text{ini}} = 1$  to  $\Lambda_{\text{fin}} = 0$  the effect of the hybridization  $\Delta(\omega)$  is slowly turned off, while at the same time the lattice dispersion  $\epsilon_{\mathbf{k}}$  is restored.

To reduce the numerical effort of the flow, Taranto *et al.* [53] decomposed the vertex function into channels, each function of a single frequency. As we will see in Chapter 4, in order to access the strong coupling regime the full frequency dependence for each channel is required. However, in Ref. [53] as a test case only the intermediate coupling  $U = 4t$  case has been treated. In Fig. 1.8 we report from Ref. [53] the imaginary part of the self-energy shown as a function of frequency for a specific set of  $\mathbf{k}$ -points. The case reported refers to half-filling  $n = 1$ , with  $t' = 0$  and  $T = 0.1t$ . In the inset the static spin correlation function shows strong antiferromagnetic fluctuations.

Before commenting on the role of the truncation, we mention here the absence of the double counting problem that might affect an extension of the DMFT, *i.e.*, the possibility for a double inclusion of the local correlations already taken into account in DMFT. In principle, the DMF<sup>2</sup>RG in its functional formulation is exact, since, as in the conventional fRG, the final value of the functional  $\Gamma^\Lambda[\psi, \bar{\psi}]$  is the exact quantum effective action. When considering the flow of the vertex and the self-energy, the only approximation involved is the truncation, that takes the form  $\mathcal{T}^{V_6} \simeq 0$  (1.29), containing the six-points vertex  $V^{(6)}$ . While in the fRG this truncation translates into neglecting

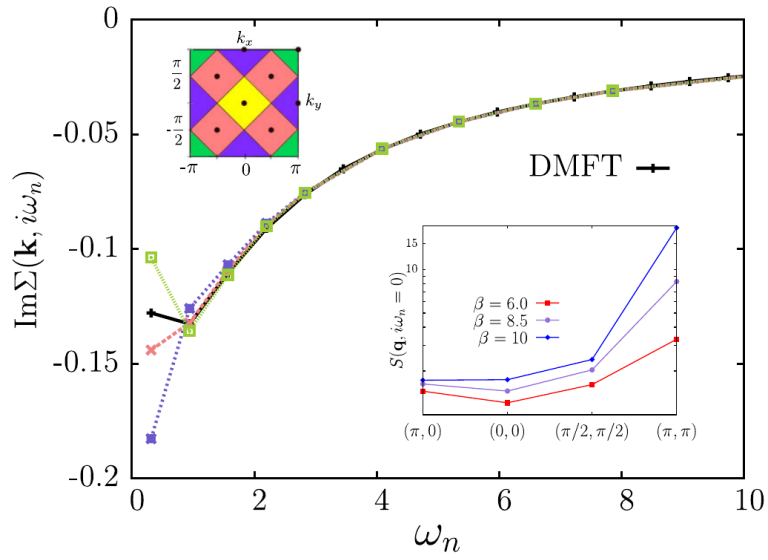


Figure 1.8: Imaginary part of the self-energy ( $n = 1$ ,  $t' = 0$  and  $T = 0.1t$ ) in frequency space for specific set of  $\mathbf{k}$ -points in units of  $4t = 1$ . In the inset the static spin correlation functions along a path in the BZ is shown for different inverse temperature  $\beta$ . Figure taken from [53].

---

completely the effects of higher order 1PI vertices  $V^{(n)}$  with  $n \geq 6$ , in the DMF<sup>2</sup>RG the DMFT solution captures their effects at least at the local level. Hence, the truncation must be understood at the level of nonlocal contributions beyond DMFT.

More insights on the truncation effects in DMF<sup>2</sup>RG are discussed in Chapter 4, where we apply this method to the 2D Hubbard model at strong coupling. As we shall see, already at half-filling the DMF<sup>2</sup>RG is able to capture important strong coupling physics, e.g., antiferromagnetic correlations described by the Heisenberg coupling. We also shall apply the DMF<sup>2</sup>RG to the case with finite doping and with a next-to-nearest neighbor hopping amplitude at strong coupling, where the interplay of antiferromagnetic fluctuations with other channels becomes more interesting.



# Frequency dependent interaction with the functional RG

As stated in the introduction, in this thesis we address the role of the frequency dependence in the vertex function, particularly important when accessing the strong coupling regime in the DMF<sup>2</sup>RG. In the fRG a comprehensive understanding of a fully dynamical interaction has not been addressed so far for the 2D Hubbard model. It has been already analyzed in a quantum impurity model by Karrasch *et al.* [29], who suggested that the frequency dependence can be simplified with the introduction of three interaction channels, each depending only on a specific combination of frequencies. In the Holstein-Hubbard model, as shown by RG studies [32, 81, 82], the phonon exchange generates an effective electron-electron interaction whose frequency dependence is physically relevant, since it describes the retardation of these interactions.

In the 2D Hubbard model, the channel decomposition has been used in combination with a form-factor expansion in momentum space [33, 36, 35]. Husemann *et al.* [34] and, at about the same time, Uebelacker and Honerkamp [64] introduced the dependence on the two remaining frequencies and observed a minor impact on the critical scale. Husemann *et al.* [34] also observed a singularity in the charge channel that cannot be interpreted as a standard instability. In this chapter, we derive and solve numerically the flow equations for the self-energy and the vertex at finite temperature without any assumption on the frequency dependence and with a high resolution. We perform a detailed analysis of the frequency dependence by specifically focusing on the understanding and interpretation of important frequency structures arising already in the intermediate coupling region. The results shown in this chapter are also presented in the peer reviewed paper [65].

## 2.1 Full dynamical decomposition

In Chapter 1, we derived the flow equations for the self-energy  $\Sigma^\Lambda(k)$ , (1.36), and the vertex  $V^\Lambda(k_1, k_2, k_3)$ , (1.35). For a better parametrization of the vertex function in terms of momentum and frequency dependence, we use the channel decomposition introduced by Husemann and Salmhofer [33]

$$\begin{aligned} V^\Lambda(k_1, k_2, k_3) &= U - \dot{\phi}_p^\Lambda(k_1 + k_2; k_1, k_3) + \dot{\phi}_m^\Lambda(k_2 - k_3; k_1, k_2) \\ &+ \frac{1}{2}\dot{\phi}_m^\Lambda(k_3 - k_1; k_1, k_2) - \frac{1}{2}\dot{\phi}_c^\Lambda(k_3 - k_1; k_1, k_2). \end{aligned} \quad (2.1)$$

We introduced the *pairing* channel  $\phi_p$ , the *charge* channel  $\phi_c$  and the *magnetic* channel  $\phi_m$ . We use a mixed notation where the first argument of  $\phi_x$  is a linear combination of frequency and momentum, contrary to the second and the third arguments.

To derive the flow equations for  $\phi_x$ , we substitute the decomposition (2.1) into the fRG flow equation for the vertex (1.35)

$$\begin{aligned} -\dot{\phi}_p^\Lambda(k_1 + k_2; k_1, k_3) + \dot{\phi}_m^\Lambda(k_2 - k_3; k_1, k_2) + \frac{1}{2}\dot{\phi}_m^\Lambda(k_3 - k_1; k_1, k_2) - \frac{1}{2}\dot{\phi}_c^\Lambda(k_3 - k_1; k_1, k_2) \\ = \mathcal{T}_{pp}^\Lambda(k_1, k_2, k_3) + \mathcal{T}_{ph}^\Lambda(k_1, k_2, k_3) + \mathcal{T}_{phc}^\Lambda(k_1, k_2, k_3). \end{aligned} \quad (2.2)$$

We associate the total momentum argument of  $\mathcal{P}_{pp}$  and the total momentum transfer argument of  $\mathcal{P}_{ph}$  in Eqs. (1.35) to the corresponding argument of  $\phi_x$ , on the right-hand side of Eq. (2.1). This way, it is easy to attribute  $\mathcal{T}_{pp}^\Lambda$  to the flow equation of the only function in Eq. (2.1) that depends explicitly on  $k_1 + k_2$ :  $-\dot{\phi}_p^\Lambda = \mathcal{T}_{pp}^\Lambda$ . The same is true for the particle-hole crossed channel:  $\mathcal{T}_{phc}^\Lambda = \dot{\phi}_m^\Lambda$ . We associate to the particle-hole diagram, the third and fourth term on the left-hand side of Eq.(2.2):  $\mathcal{T}_{ph}^\Lambda(k_1, k_2, k_3) = \frac{1}{2}\dot{\phi}_m^\Lambda(k_3 - k_1; k_1, k_2) - \frac{1}{2}\dot{\phi}_c^\Lambda(k_3 - k_1; k_1, k_2)$ . We note that this procedure, based on the above channel decomposition (2.1), applies for any truncation that separates between particle-particle, particle-hole direct and crossed contributions.

The flow equations for the  $\phi_x$  then read

$$\dot{\phi}_p^\Lambda(Q; k_1, k_3) = -\mathcal{T}_{pp}^\Lambda(k_1, Q - k_1, k_3), \quad (2.3a)$$

$$\dot{\phi}_c^\Lambda(Q; k_1, k_2) = \mathcal{T}_{phc}^\Lambda(k_1, k_2, k_2 - Q) - 2\mathcal{T}_{ph}^\Lambda(k_1, k_2, Q + k_1), \quad (2.3b)$$

$$\dot{\phi}_m^\Lambda(Q; k_1, k_2) = \mathcal{T}_{phc}^\Lambda(k_1, k_2, k_2 - Q). \quad (2.3c)$$

As discussed in the introduction, our scope is to treat the frequency dependence without any further assumption; hence, we keep the full frequency dependence in all the channels  $\phi_x$ . To parametrize the dependence on the fermionic momenta, we use a decomposition of unity by means of a set of orthonormal form factors  $\{f_i(\mathbf{k})\}$  [33]. We then project each channel on a subset of form factors, based on physical assumptions. In particular, for the magnetic and charge channel we consider only the  $s$ -wave component  $f_s(\mathbf{k}) = 1$ , while for the pairing channel we allow for both  $s$ -wave and  $d$ -wave components with  $f_d(\mathbf{k}) = \cos(k_x) - \cos(k_y)$  [33]

$$\phi_p^\Lambda(Q; k_1, k_3) = \mathcal{S}_{\mathbf{Q},\Omega}^\Lambda(\nu_1, \nu_3) + f_d\left(\frac{\mathbf{Q}}{2} - \mathbf{k}_1\right) f_d\left(\frac{\mathbf{Q}}{2} - \mathbf{k}_3\right) \mathcal{D}_{\mathbf{Q},\Omega}^\Lambda(\nu_1, \nu_3), \quad (2.4a)$$

$$\phi_c^\Lambda(Q; k_1, k_2) = \mathcal{C}_{\mathbf{Q},\Omega}^\Lambda(\nu_1, \nu_2), \quad (2.4b)$$

$$\phi_m^\Lambda(Q; k_1, k_2) = \mathcal{M}_{\mathbf{Q},\Omega}^\Lambda(\nu_1, \nu_2). \quad (2.4c)$$

A divergence in the channel  $\mathcal{S}^\Lambda$  ( $\mathcal{D}^\Lambda$ ) represents an instability towards a  $s$ -wave ( $d$ -wave) superconducting state, while a divergence in the channels  $\mathcal{C}$  and  $\mathcal{M}$  represent an instability in the  $s$ -wave magnetic and  $s$ -wave charge channels. [33] The equations for  $\mathcal{S}^\Lambda$ ,  $\mathcal{D}^\Lambda$ ,  $\mathcal{C}^\Lambda$  and  $\mathcal{M}^\Lambda$  can be derived by substituting definitions (2.4) into Eqs. (2.3) and (1.35) and by projecting onto the form factors. The final equations together with the derivation details are reported in Appendix A.

Each channel  $\phi_x$  in Eq. (2.1) contains a (bosonic) linear combination of momenta and frequencies, and two remaining independent fermionic momentum and frequency variables. The choice of the mixed notation is natural since the bosonic momenta and frequencies play a special role in the diagrammatics. Indeed, it is the only dependence generated in second-order perturbation theory and the main dependence in finite order perturbation theory. Although the dependence on the bosonic frequency becomes more and more dominant when approaching the weak-coupling limit  $U \rightarrow 0$ , we will show that the dependence on the two remaining fermionic frequencies becomes strong and non-negligible already at moderate coupling.

## 2.2 Interaction scheme

To apply the flow equations we need to specify the  $\Lambda$  dependence of the noninteracting propagator  $G_0^\Lambda$ . Here we use the *interaction flow*, introduced by Honerkamp *et al.* [60]

$$G_0^\Lambda(k) = \frac{\Lambda}{i\nu + \mu^\Lambda - \varepsilon_{\mathbf{k}}}, \quad (2.5)$$

where the scale-parameter  $\Lambda$  flows from  $\Lambda_{\text{ini}} = 0$  to  $\Lambda_{\text{fin}} = 1$ . We have introduced a  $\Lambda$ -dependent chemical potential to maintain the density fixed during the flow. In Eq. (2.5), the flow parameter  $\Lambda$  cannot be interpreted as a *scale* and, hence, in this case the flow does not represent a scale-selective inclusion of fluctuations.

For a better understanding of the interaction scheme, we explicitly write the  $\Lambda$ -dependent action as

$$S^\Lambda[\psi, \bar{\psi}] = -\Lambda^{-1} (\bar{\psi}, G_0^{-1}\psi) + U \sum_i \int d\tau n_{i,\uparrow}(\tau) n_{i,\downarrow}(\tau). \quad (2.6)$$

In terms of the new rescaled fields  $\eta = \Lambda^{-\frac{1}{2}}\psi$  and  $\bar{\eta} = \Lambda^{-\frac{1}{2}}\bar{\psi}$ , action (2.6) has the form

$$S^\Lambda[\eta, \bar{\eta}] = -(\bar{\eta}, G_0^{-1}\eta) + U_{\text{eff}}^\Lambda \sum_i \int d\tau \tilde{n}_{i,\uparrow}(\tau) \tilde{n}_{i,\downarrow}(\tau), \quad (2.7)$$

where we defined  $\tilde{n}_\sigma(\tau) = \bar{\eta}_\sigma(\tau)\eta_\sigma(\tau)$  and  $U_{\text{eff}}^\Lambda = \Lambda^2 U$ . Eq. (2.7) represents the action of the Hubbard model with interaction strength  $U_{\text{eff}}^\Lambda$ . Hence, in the interaction flow, the vertex  $V^\Lambda$  and the self-energy  $\Sigma^\Lambda$ , can be interpreted as final solutions of the flow with rescaled interaction  $U_{\text{eff}}^\Lambda = \Lambda^2 U$ .

The flow starts from a noninteracting condition, since  $\Lambda_{\text{ini}} = 0$  implies  $U_{\text{eff}}^\Lambda = 0$ . While solving the flow for  $\Lambda > 0$ , the effective interaction correspondingly increases,  $U_{\text{eff}}^\Lambda > 0$ . When possible, we reach the end of the flow at  $\Lambda_{\text{fin}} = 1$ , the rescaled fields equal the original ones  $\eta = \psi$  and  $\bar{\eta} = \bar{\psi}$  and the bare coupling  $U_{\text{eff}}^\Lambda = U$  is restored. Instead, when encountering an instability at  $\Lambda_c$ , the self-energy  $\Sigma^{\Lambda_c}$  and the vertex  $V^{\Lambda_c}$  are interpreted as solutions of the Hubbard model at the critical coupling  $U_c = \Lambda_c^2 U$ .

From the Dyson equation we calculate the interacting Green's function in the form

$$G^\Lambda(k) = \frac{\Lambda}{i\nu - \varepsilon_{\mathbf{k}} + \mu^\Lambda - \Lambda\Sigma^\Lambda(k)}. \quad (2.8)$$

The corresponding single-scale propagator is given by

$$S^\Lambda(k) = \frac{i\nu - \varepsilon_{\mathbf{k}} + \mu^\Lambda - \Lambda\partial\mu^\Lambda/\partial\Lambda}{(i\nu - \varepsilon_{\mathbf{k}} + \mu^\Lambda - \Lambda\Sigma^\Lambda(k))^2}. \quad (2.9)$$

The  $\Lambda$ -dependent chemical potential  $\mu^\Lambda$  has to be determined from the equation

$$n = 2 \int_k e^{i\nu 0^+} \frac{G^\Lambda(k)}{\Lambda} = 2 \int_k \frac{e^{i\nu 0^+}}{i\nu - \varepsilon_{\mathbf{k}} + \mu^\Lambda - \Lambda\Sigma^\Lambda(k)}. \quad (2.10)$$

The factor 2 accounts for the spin degree of freedom. We specifically choose the filling associated to the rescaled fields since, unlike  $\langle\bar{\psi}\psi\rangle$ ,  $\langle\bar{\eta}\eta\rangle$  is well defined also at the initial value  $\Lambda_{\text{ini}} = 0$ , where the chemical potential  $\mu^{\Lambda_{\text{ini}}}$  is the noninteracting one, and it has a precise interpretation at any  $\Lambda$  value. While different at the intermediate steps, at the final value  $\Lambda = 1$  the fillings (2.10) and  $\langle\bar{\psi}\psi\rangle$  coincide.

In the interaction flow, contributions to pairing which are discarded by our truncation at the two-particle level are more important than in the more commonly used flows with a momentum or frequency cutoff. Unlike magnetism,  $d$ -wave pairing is generated exclusively by diagrams with (at least two) overlapping loops. In fact, the  $d$ -wave pairing channel is the most affected, since it is the only channel generated by nested loop diagrams only.

As an example, we consider the perturbative diagram shown in Fig. 2.1a, which is a renormalization of the particle-particle interaction due to particle-hole bubble inclusions. For our scope, we associate the internal line with the  $\Lambda$ -dependent propagator  $G_0^\Lambda$ , as given in the interaction scheme, and consider the derivative with respect to  $\Lambda$  of the diagram 2.1a. The  $\Lambda$  derivative is composed by three terms, diagrams (b), (c) and (d) of Fig. 2.1, the only difference being the position of the noninteracting single-scale propagator  $S_0^\Lambda = \partial_\Lambda G_0^\Lambda$ . We represent by a long cut, for example in diagram (b), the combination  $S_0^\Lambda(q-k)G_0^\Lambda(k) + G_0^\Lambda(q-k)S_0^\Lambda(k)$  coming from the  $\Lambda$ -derivative.

In the level-2 truncation, only the diagram (b) is taken into account while the dia-

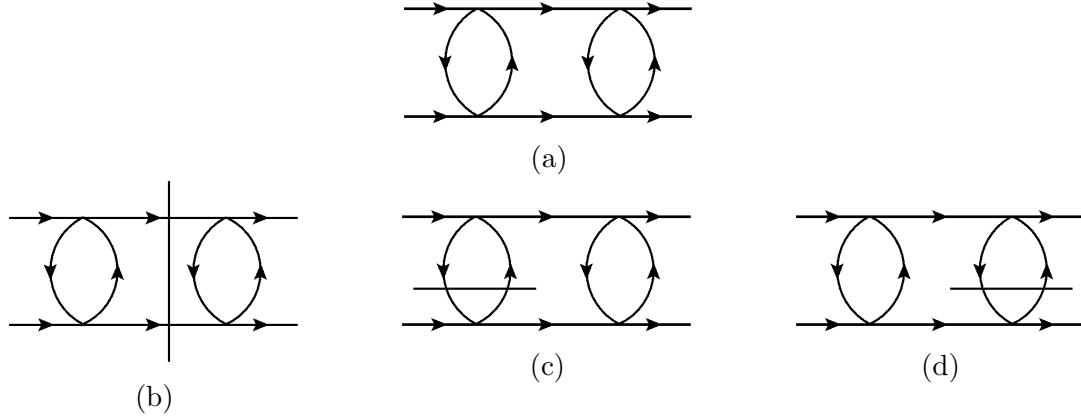


Figure 2.1: (a): Perturbative diagram contributing to the renormalization of the pairing channel due to the particle-hole bubble. (b), (c) and (d):  $\Lambda$  derivatives of diagram (a). The internal lines refers to the propagator  $G_0^\Lambda$ . The long cut represents the combination, e.g.,  $S_0^\Lambda(q-k)G_0^\Lambda(k) + G_0^\Lambda(q-k)S_0^\Lambda(k)$ , arising from the  $\Lambda$ -derivative.

grams (c) and (d) are neglected. While the total sum (b)+(c)+(d) is independent of the flow scheme, the single contribution is not. Hence, the choice of the flow scheme  $G_0^\Lambda$ , in level-2 truncation, can be exploited to mitigate, in principle, the effects of the diagrams not included in the flow equations, for instance in this case (c) and (d), by making these contributions subleading. Binz *et al.* [83] showed that, in the presence of an infrared cutoff and in the case of the perfect nesting of the Fermi surface, the diagrams arising from the derivative of the internal loop lines are negligibly small compared to the contribution coming from the derivative of the external loop, see also Ref. [74]. However, this is not the case for the interaction flow, where  $G_0^\Lambda = \Lambda G_0$  implies  $S_0^\Lambda = G_0$ . In fact, all the three diagrams (b), (c) and (d) are equal and the level-2 truncation accounts only for 1/3 of the full diagram (a).

## 2.3 Instability analysis and phase diagram

In this section we present the numerical solution of the flow equations together with the resulting instability analysis. The numerical setup is discussed in Appendix B. The divergence of the vertex in a particular channel signals the presence of an instability in the given channel. We refer to the value  $\Lambda_c$  at which this happens as the critical flow parameter. In the interaction flow, the critical value  $\Lambda_c$  corresponds to a critical

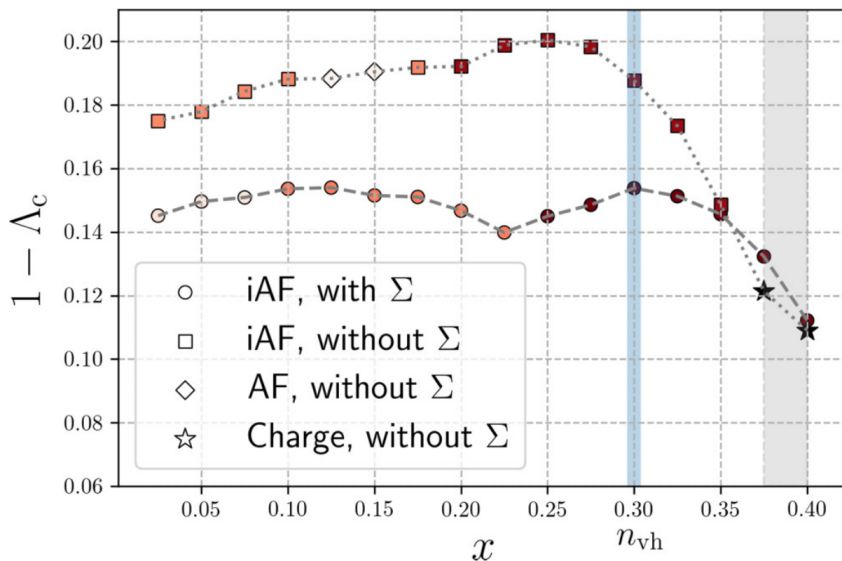


Figure 2.2: Critical flow parameter as a function of doping  $x = 1 - n$ , for  $T = 0.08t$ ,  $t' = -0.32t$  and  $U = 4t$ . The black stars refer to a divergence in the charge channel at  $\mathbf{Q} = (0, 0)$ . The color of squares, circles and diamonds encodes the distance of the incommensurate magnetic vector  $\mathbf{Q} = (\pi, \pi - 2\pi\eta)$  from  $(\pi, \pi)$ : darker color corresponds to a larger distance. The darkest color corresponds to  $\eta = 0.18$ . The vertical light blue line marks van Hove filling.

interaction  $U_c = \Lambda_c^2 U$ , see Section 2.2. In Fig. 2.2 we show  $1 - \Lambda_c$  as a function of the doping  $x = 1 - n$ . The critical value  $\Lambda_c$  is determined as the flow parameter where one of the channels exceeds the value of  $200t$ . The temperature is  $T = 0.08t$ , the next-to-nearest neighbor hopping amplitude  $t' = -0.32t$ , and the bare interaction strength  $U = 4t$ .

A divergence of the vertex at finite temperature is associated with spontaneous symmetry breaking, in violation of the Mermin-Wagner theorem [39]. This is a consequence of the truncation of the flow equations. Instead, we should interpret the finite temperature vertex divergence as the signal of the appearance of strong bosonic fluctuations that cannot be treated within the approximation scheme we are using [61]. Even though in our framework the flow cannot be continued beyond the critical flow parameter, from the analysis of vertex and self-energy we can identify the relevant effective interactions of the system.

The figure shows the cases with and without self-energy feedback. In the first case

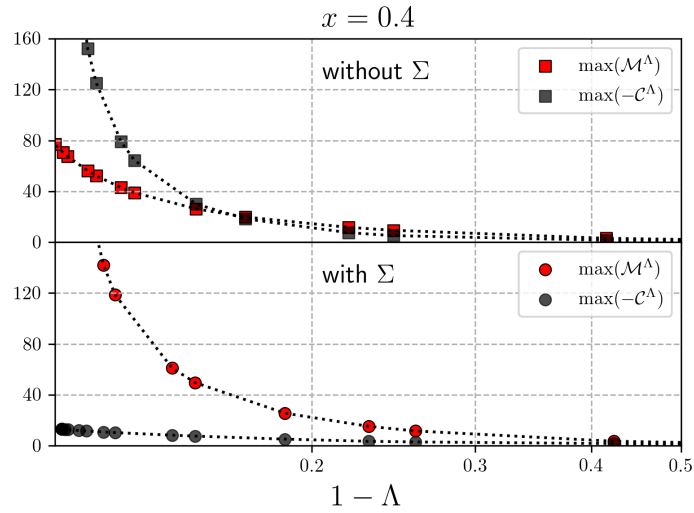
we have only an antiferromagnetic instability, commensurate (AF) or incommensurate (iAF) depending on the value of the doping  $x$ . The magnetic channel, as well as the spin susceptibility, has its maximum value at zero exchange frequency  $\Omega = 0$  at momentum  $\mathbf{Q} = (\pi, \pi - 2\pi\eta)$ , where  $\eta$  is the incommensurability factor. The region  $0.125 \leq x \leq 0.150$  shows a commensurate peak with  $\eta = 0$ . However, we rather observed a degeneracy of the commensurate and the incommensurate peaks in the spin susceptibility due to a large plateau around  $(\pi, \pi)$  observed in the bare bubble.

In the case without self-energy feedback an antiferromagnetic instability has been observed apart from the dopings  $x = 0.375$  and  $x = 0.4$ , where a peculiar divergence in the charge channel has been observed. This cannot be interpreted as a standard instability, since the charge channel becomes negatively divergent for the finite particle-hole frequency  $\Omega = 2\pi T$  and momentum  $\mathbf{Q} = (0, 0)$ . This feature has already been observed by Husemann *et al.* [34] and was named *scattering instability*. We also checked that the charge susceptibility becomes negatively divergent at finite frequency  $\Omega = 2\pi T$ . However, this divergence disappears when including the self-energy feedback. Its origin will be addressed in the Section 2.4.

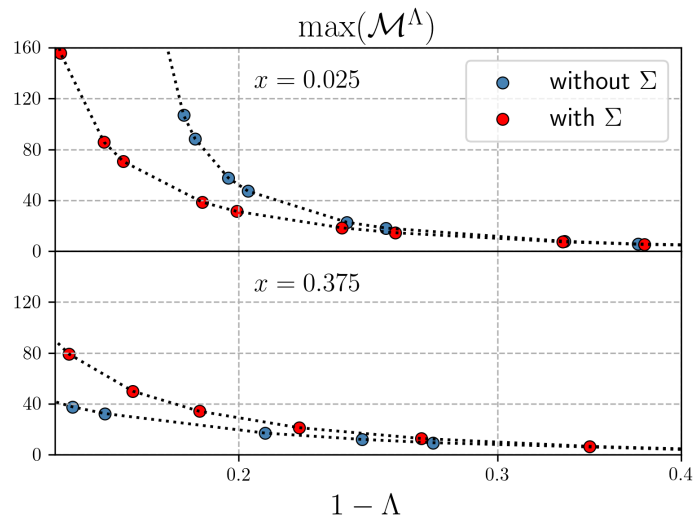
We did not find a pairing instability at any doping. While  $d$ -wave pairing has been persistently obtained in most earlier fRG studies of the two-dimensional Hubbard model at sufficiently strong doping, [20] the  $d$ -wave pairing interaction in our calculation remains rather small.

We attribute this seeming discrepancy to three reasons. First, we chose a relatively high temperature to be able to accurately parametrize the frequency dependence, while the pairing interaction is expected to increase substantially only for temperatures close to the pairing scale [35]. Second, as already observed by Husemann *et al.*, [34] previous fRG calculations with a static vertex overestimate the  $d$ -wave pairing channel, since the contributing effective interactions decay at large frequencies. Hence, taking the frequency dependence of the vertex into account one obtains a lower pairing scale. Third, as discussed in the previous section, the interaction flow underestimates the  $d$ -wave pairing contributions.

The self-energy feedback has three effects on the critical value  $\Lambda_c$ . First, it increases  $\Lambda_c$ , that is, it suppresses the instabilities. Second, the incommensurability vector is affected, the region of commensurate antiferromagnetism disappears, and one can observe a more regular trend of increasing  $\eta$  with  $x$ . Third, the divergence in the charge channel is



(a)



(b)

Figure 2.3: (a) Flow of the maximal values of the charge ( $\mathcal{C}$ ) and magnetic ( $\mathcal{M}$ ) channels as functions of  $1 - \Lambda$ , for  $x = 0.4$ ,  $t' = -0.32$ ,  $U = 4t$  and  $T = 0.08t$ . Top: without self-energy feedback; bottom: with self-energy feedback.

(b) Flow of the maximal values of the magnetic ( $\mathcal{M}$ ) channel as functions of  $1 - \Lambda$ , for  $x = 0.025$  (top) and  $x = 0.375$  (bottom). The other parameters are  $t' = -0.32$ ,  $U = 4t$  and  $T = 0.08t$ . Red symbols: with self-energy feedback; blue symbols: without self-energy feedback.

completely suppressed, and the leading instability in the doping region  $0.375 \leq x \leq 0.4$  remains incommensurate antiferromagnetism. This can be also seen from Fig. 2.3a, where we compare the flow of the maximum (of the absolute value) of magnetic and charge channels with and without the self-energy feedback for doping  $x = 0.4$ . Without self-energy feedback, the charge channel reaches large and negative values. The presence of such a large (and negative) charge channel inhibits the magnetic channel. The effect of the self-energy in the flow is evident: the charge channel is strongly suppressed. At the same time the magnetic channel is enhanced.

This is confirmed by Fig. 2.3b, where we show the maximum of  $\mathcal{M}$  with and without self-energy feedback for  $x = 0.025$  (top) and  $x = 0.375$  (bottom). One can see that the enhancement of  $\mathcal{M}$  due to the self-energy is specific of the large doping region, while, in the small doping region the self energy decreases  $\mathcal{M}$ . The self-energy affects the magnetic channel directly by reducing the particle-hole bubble, and indirectly through the feedback of other channels, that is, reducing the charge channel. The former effect dominates for small doping, the latter at large doping.

The suppression of instabilities, and in particular the elimination of the artificial charge instability by dynamical self-energy feedback was already observed by Husemann et al. [34] In that work, however, the momentum dependence of the self-energy was approximated by its value at the van Hove points, where it is particularly large. The suppression effects are thereby likely somewhat overestimated.

Trying to understand the self-energy feedback effects, we look for possible changes in the Fermi surface. To this end we analyze the momentum distribution

$$n^\Lambda(\mathbf{k}) = 2T \sum_{\nu} e^{i\nu 0^+} \frac{G^\Lambda(\mathbf{k}, \nu)}{\Lambda} = 2T \sum_{\nu} \frac{e^{i\nu 0^+}}{i\nu - \varepsilon_{\mathbf{k}} + \mu^\Lambda - \Lambda \Sigma^\Lambda(\mathbf{k}, \nu)}. \quad (2.11)$$

In our calculations, we get rid of the convergence factor  $e^{i\nu 0^+}$  by adding and subtracting the non-interacting distribution  $n_0(\mathbf{k}) = 2T \sum_{\nu} e^{i\nu 0^+} G_0(\mathbf{k}, \nu)$  and by using the contour integration method [84]. Note that we defined the momentum distribution with respect to the rescaled fields  $\eta$  and  $\bar{\eta}$ , introduced in Section 2.2.

In Fig. 2.4 we show the non-interacting (top left) and interacting (top right) momentum distribution in the first quadrant of the Brillouin zone for doping  $x = 0.025$ . The latter is computed at the critical value  $\Lambda_c$ . Comparing the two panels, one does not ob-

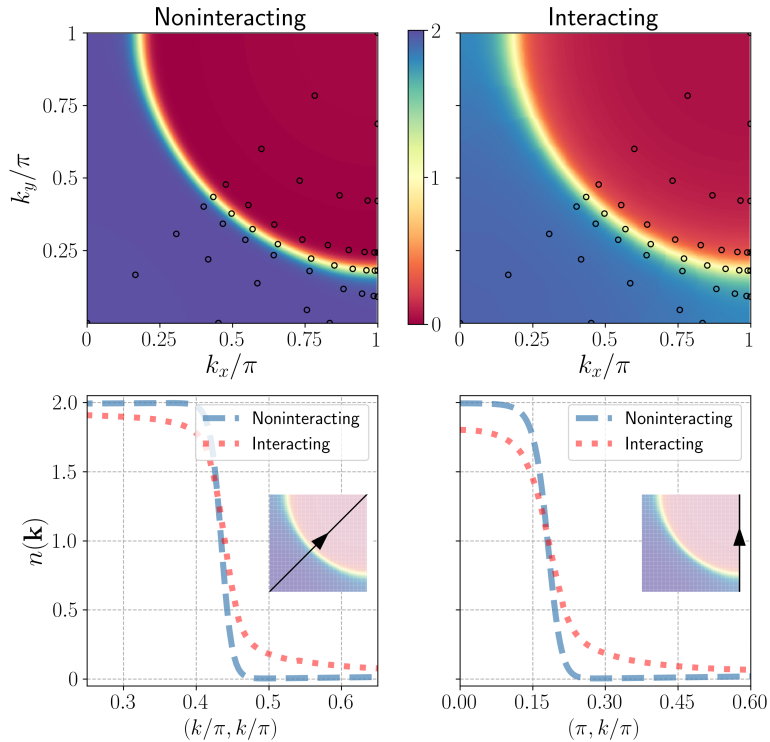


Figure 2.4: Top row: momentum distribution for  $t' = -0.32t$ ,  $T = 0.08t$  and doping  $x = 0.025$ . Left panel: non-interacting case. Right panel: interacting case for  $U = 4t$ . The black circles mark the points used to patch the self-energy. Bottom row: cut of the occupation along the Brillouin zone paths reported as arrows in the insets. Blue dashed curves are results for the non-interacting system, while red dotted curves are for  $U = 4t$ .

serve any relevant shift of the Fermi surface position, but the Fermi surface broadening is appreciably larger in the interacting case, due to the self-energy.

To observe the effects of the frequency dependence on the critical value  $\Lambda_c$ , we now compare our full dynamical approach with an approximation scheme often used in the fRG literature [33, 35]. In particular, for this scope we introduce the *bosonic* approximation scheme for the channels as  $\mathcal{X}_{\mathbf{Q},\Omega}(\nu, \nu') \simeq \mathcal{X}_{\mathbf{Q},\Omega}$ , with  $\mathcal{X} = \{\mathcal{S}, \mathcal{D}, \mathcal{C}, \mathcal{M}\}$ . In this approximation, the resulting flow equation, for instance for the magnetic channel has the form

$$\dot{\mathcal{M}}_{\mathbf{Q},\Omega}^{\Lambda} = \int_{\mathbf{k}_1, \mathbf{k}_2} \mathcal{T}_{\text{phc}}^{\Lambda}(k_1, k_2, k_2 - Q). \quad (2.12)$$

Contrary to the left-hand side, the right-hand side still depends on  $\nu_1$  and  $\nu_2$ , which has to be fixed to some value.

In Fig. 2.5, we compare the critical value  $\Lambda_c$  for different approximations on the vertex frequency dependence: our fully dynamic approach, the bosonic approximation scheme and a static approximation. In none of these results we took the self-energy feedback into account. The static approximation is obtained by completely neglecting the frequency structures of the channels, assuming the vertex to be constant in frequency space. Following Ref. [33], for the bosonic approximation we evaluate the flow equations only for  $\Omega = 0$ , as transfer frequency, and  $\pm\pi T$  as fermionic arguments. However, as shown in the next section, already at moderate coupling the effective interactions have strong dependences on the other two frequency arguments, too. For this reason, there is an ambiguity in the way the interaction channels are projected to a function of a single bosonic frequency. Different projection schemes lead to quantitatively different results. In Fig. 2.5 we show the results from a low-frequency projection that leads to the critical flow parameter most consistent with the one of the fully frequency dependent scheme.

We observe that  $\Lambda_c$  is higher in the static case, that is, the instability occurs at a larger  $U^\Lambda$ . This is due to two reasons, first, by taking  $\nu_1 = -\nu_2 = \pi T$  the leading magnetic channel (at fixed bosonic frequency) is approximated by its minimal value, as will be shown in the next paragraph. Second, in the static approximation the feedback of the other channels is overestimated, see below. For  $x \geq 0.34$  there is no divergence in any channel in the static approximation for the temperature considered.

In Fig. 2.5 we also show the maximal value of the  $d$ -wave pairing interaction  $\mathcal{D}^\Lambda$  at  $\Lambda_c$  in the static, bosonic and fully dynamic parametrizations. In none of these results  $d$ -wave pairing is the leading instability at the temperature under consideration, but in the static approximation  $\mathcal{D}^{\Lambda_c}$  is orders of magnitude larger than in the other two cases. At lower temperatures (not shown here) we do observe a  $d$ -wave pairing instability in the static approximation. This suppression of pairing by the frequency dependence of the vertex, already observed by Husemann et al. [34], has been explained above in this section.

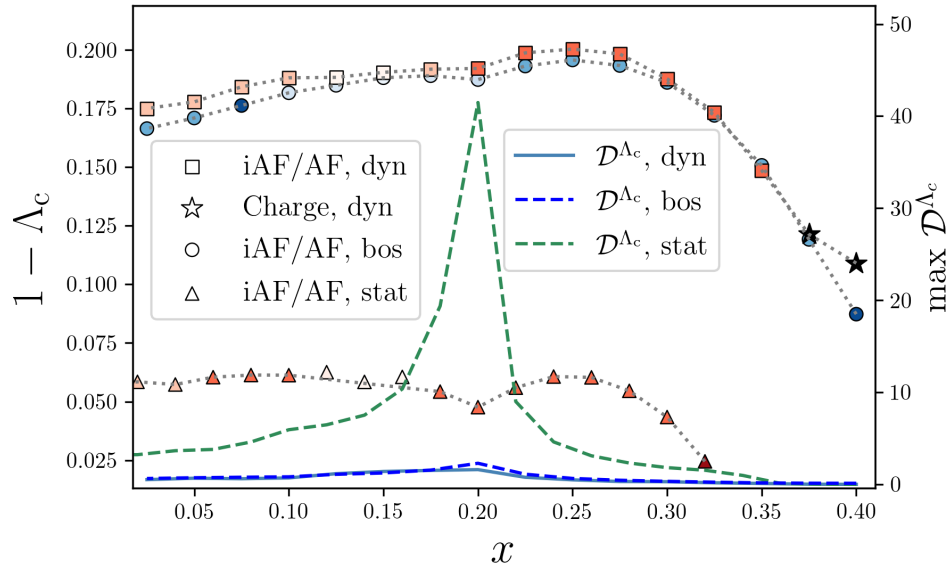


Figure 2.5: Critical flow parameter as a function of doping  $x = 1 - n$ , for  $T = 0.08t$ ,  $t' = -0.32t$  and  $U = 4t$ . Squares, circles and triangles refer to leading couplings in the magnetic channel for dynamic, bosonic, and static implementations respectively. The black stars refer to a divergence in the charge channel at  $\mathbf{Q} = (0, 0)$ . In all the implementations, no self-energy feedback has been used. The color of squares and circles encodes the distance of the incommensurate magnetic  $\mathbf{Q}$ -vector from  $(\pi, \pi)$ : darker color corresponds to a larger distance, as in Fig. 2.2. The maximal value of  $\mathcal{D}^\Lambda$  at the critical value  $\Lambda_c$  is marked by a solid blue line for the dynamic implementation, by a dashed light blue line for the bosonic approximation, and by a dashed green line for the static approximation.

## 2.4 Vertex frequency dependence and charge divergence

In this section we focus on the remarkable frequency dependence of the vertex. We will first look at the channels showing a divergence, that is, the charge and the magnetic instabilities observed in Fig. 2.2, and we will then discuss the pairing channels.

As mentioned in the previous section, the divergences of the charge and magnetic channels are quite different. The charge channel diverges for a finite frequency transfer, and only when we neglect the self-energy feedback. Since the dependence on the transfer

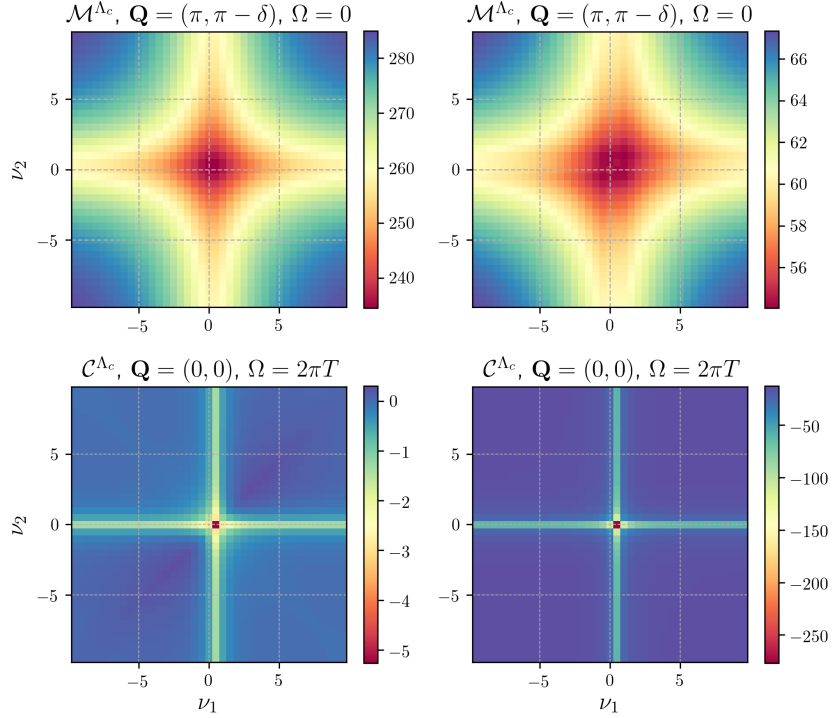


Figure 2.6: Frequency dependence of the magnetic (top) and charge (bottom) channel for  $t' = -0.32$ ,  $U = 4t$  and  $T = 0.08t$ . The left column corresponds to the doping value  $x = 0.025$  and with self-energy feedback, while the right column, instead, to  $x = 0.4$  and without self-energy feedback.

momentum and frequency  $(\mathbf{Q}, \Omega)$  has already been discussed in Ref. [34], we focus on the dependence on the fermionic frequencies. Therefore we present various color plots for fixed  $(\mathbf{Q}, \Omega)$ , showing the dependence on  $\nu_1$  and  $\nu_2$ .

In the top left panel of Fig. 2.6 we show the magnetic channel  $\mathcal{M}_{\mathbf{Q}, \Omega}^{\Lambda_c}(\nu_1, \nu_2)$  in the small doping region, where antiferromagnetism is the leading instability. The results shown have been calculated with self-energy feedback, but the frequency structures we discuss do not depend strongly on the presence of the self-energy. For clarity we restrict the plots to the first 20 positive and negative Matsubara frequencies. When only one channel in the flow equations is taken into account, the fRG equations are equivalent to the RPA [85]. The magnetic channel calculated with RPA would depend only on the

frequency and momentum transfer. Hence any variation in the frequency structure has to be ascribed to the presence of the other channels in the fRG. The channel competition suppresses the magnetic channel: the largest value of  $\mathcal{M}$  is reduced compared to the RPA, and the frequency dependent structure at the center is further reduced compared to the asymptotic values at large  $\nu_1, \nu_2$ .

In the bottom left panel of Fig. 2.6 we show the frequency dependence of the charge channel  $\mathcal{C}_{\mathbf{Q},\Omega}^{\Lambda_c}(\nu_1, \nu_2)$  for a finite frequency transfer  $\Omega = 2\pi T$ , related to the charge instability discussed in Ref. [34] and above. The frequency structure is completely different from the magnetic channel. The charge channel has its maximum for frequencies  $\nu_1 = \pi T$  and  $\nu_2 = -\pi T$ . This structure cannot be explained in terms of standard ladder diagrams. It is related to the behavior of the retarded interaction described in Refs. [86, 87]. In the two right panels of Fig. 2.6 we show the same quantities but for  $x = 0.4$  and without self-energy feedback. In this case, the localized peak in the charge channel is the leading interaction. The position and shape of the frequency structures are similar to the one described above.

In Fig. 2.7 we display the frequency dependence of the pairing functions  $\mathcal{S}$  and  $\mathcal{D}$  for two distinct doping values  $x = 0.025$  and  $x = 0.4$ . One can see that  $\mathcal{D}^{\Lambda_c}$  is indeed asymptotically vanishing at large frequencies,[31] as can be understood from the frequency dependences in Eqs. (A.11) and (A.13).

Discussing the phase diagram in Fig. 2.2, we mentioned the presence of a spurious divergence in the charge channel, once the self-energy feedback is not taken into account. To gain insight into the origin of this singular frequency structure, we identify a simple set of Feynman diagrams reproducing the same features. The main idea is that the magnetic channel, which is generated first, is responsible for the singular structure in the charge channel.

To check this qualitatively, we first compute an effective interaction by means of an RPA in the magnetic channel, and then insert this effective magnetic interaction into a subsequent RPA equation for the charge channel. Of course one does not expect quantitative agreement with the fRG, since we overestimate both interactions, but the approximation is sufficient to reproduce and explain the qualitative features we are interested in.

We start by introducing an effective interaction that includes the magnetic fluctua-

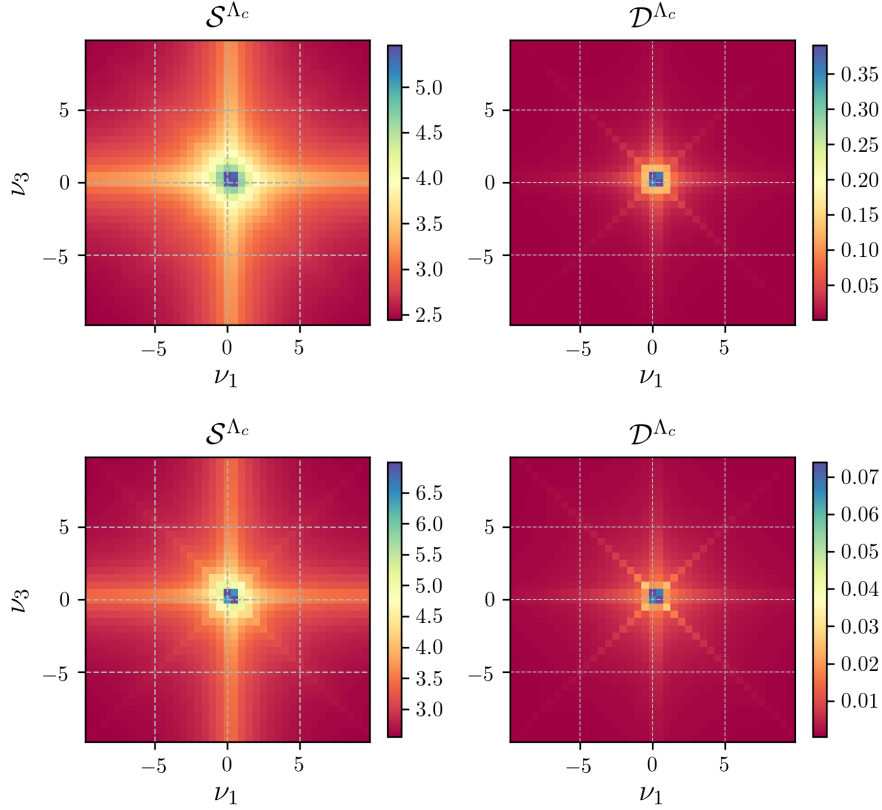


Figure 2.7: Frequency dependence of the pairing channels  $\mathcal{S}_{\mathbf{Q},\Omega}^{\Lambda_c}(\nu_1, \nu_3)$  and  $\mathcal{D}_{\mathbf{Q},\Omega}^{\Lambda_c}(\nu_1, \nu_3)$  for  $\mathbf{Q} = (0,0)$  and  $\Omega = 0$ . The doping is  $x = 0.025$  (top) and  $x = 0.4$  (bottom). The other parameters are  $T = 0.08t$ ,  $t' = -0.32t$ , and  $U = 4t$ .

tions as computed by RPA in the particle-hole crossed channel:

$$U_{\mathbf{Q},\Omega}^{\text{eff}} = \frac{U}{1 - U\Pi_{\mathbf{Q},\Omega}}. \quad (2.13)$$

Since the bare interaction  $U$  is local,  $U^{\text{eff}}$  depends only on the transfer momentum  $\mathbf{Q}$  and frequency  $\Omega$  of the particle-hole bubble

$$\Pi_{\mathbf{Q},\Omega} = -T \sum_{\nu} \int_{\mathbf{p}} G_0(\mathbf{p}, \nu) G_0(\mathbf{p} + \mathbf{Q}, \nu + \Omega). \quad (2.14)$$

The magnetic effective interaction in Eq. (2.13) will now be used to compute the RPA equation for the charge channel. Adopting the simplified momentum dependences of

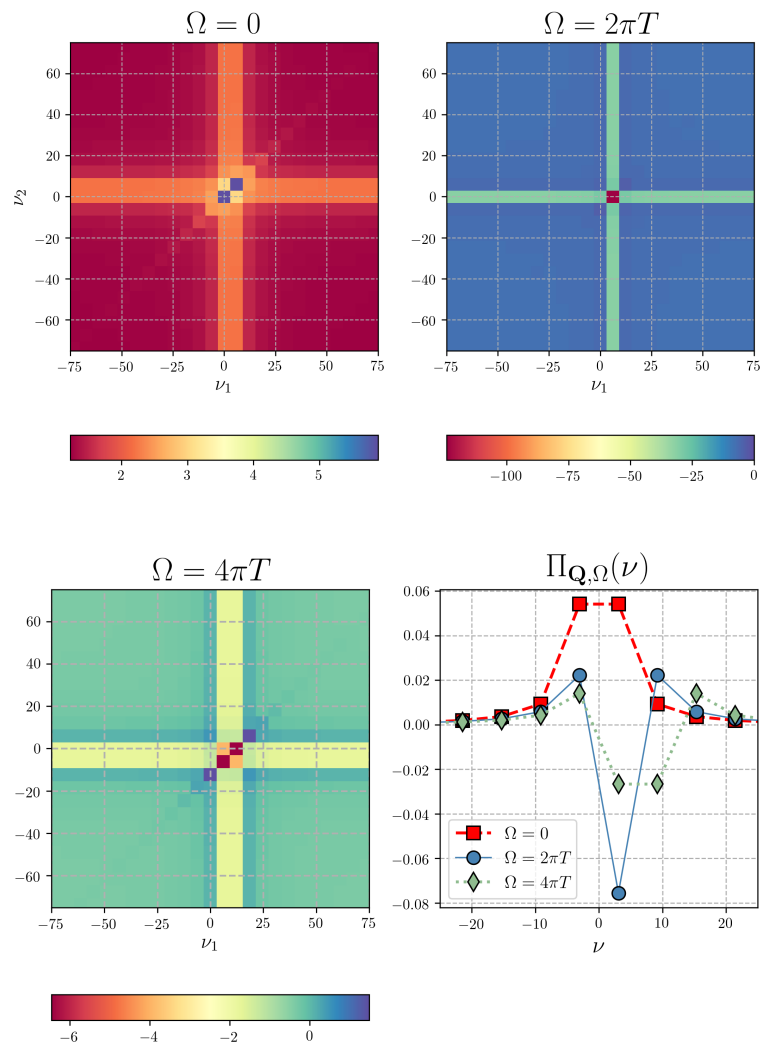


Figure 2.8: In the top row and bottom left panels, the charge channel  $\mathcal{C}_{\mathbf{Q},\Omega}(\nu_1, \nu_2) = \tilde{\mathcal{C}}_{\mathbf{Q}=(0,0),\Omega}(\nu_1, \nu_2 - \Omega)$  computed from Eq. (2.15) is shown as a function of  $\nu_1$  and  $\nu_2$  for transfer frequencies  $\Omega = 0$ ,  $\Omega = 2\pi T$  and  $\Omega = 4\pi T$ , respectively. In the bottom right panel, the bubble  $\Pi_{\mathbf{Q}=(0,0),\Omega}(\nu)$  is shown as a function of  $\nu$  for  $\Omega = 0$ ,  $\Omega = 2\pi T$  and  $\Omega = 4\pi T$ . The model parameters are  $t' = -0.32$  and  $U = 4$ , the doping  $x = 0.375$ , and the temperature  $T = t$ .

the effective interactions used in the fRG calculation, only the momentum integrated, that is, local part of the magnetic interaction  $U_{\Omega}^{\text{eff}} = \int_{\mathbf{Q}} U_{\mathbf{Q},\Omega}^{\text{eff}}$  contributes to the charge channel. We thus obtain  $\mathcal{C}_{\mathbf{Q},\Omega}(\nu_1, \nu_2) = \tilde{\mathcal{C}}_{\mathbf{Q},\Omega}(\nu_1, \nu_2 - \Omega)$ , where

$$\tilde{\mathcal{C}}_{\mathbf{Q},\Omega}(\nu_1, \nu_3) = -U_{\nu_1-\nu_3}^{\text{eff}} [\delta_{\nu_1, \nu_3} + U_{\nu_1-\nu_3}^{\text{eff}} \Pi_{\mathbf{Q},\Omega}(\nu_1)]^{-1}, \quad (2.15)$$

with

$$\Pi_{\mathbf{Q},\Omega}(\nu) = -T \int_{\mathbf{p}} G_0(\mathbf{p}, \nu) G_0(\mathbf{p} + \mathbf{Q}, \nu + \Omega). \quad (2.16)$$

Note that the fermion frequencies  $\nu$  are not summed in  $\Pi_{\mathbf{Q},\Omega}(\nu)$ , and the inverse in Eq. (2.15) is a matrix inverse of the matrix with indices  $\nu_1$  and  $\nu_3$ . Eq. (2.15) is nothing but an RPA equation with a frequency dependent interaction in the particle-hole channel. In the case of a frequency independent effective interaction  $U^{\text{eff}}$ , Eq. (2.15) becomes  $\nu_1$  and  $\nu_3$  independent and only the summed bubble  $\Pi_{\mathbf{Q},\Omega}$  appears. The frequency dependence of  $U^{\text{eff}}$  qualitatively affects the results.

In Fig. 2.8, we show the charge channel as computed from Eq. (2.15) for  $\mathbf{Q} = (0, 0)$  and different  $\Omega$  as a function of  $\nu_1$  and  $\nu_2 = \nu_3 + \Omega$ , for  $T = t$  and  $x = 0.375$ . We have to choose such a high temperature to stay in a stable paramagnetic phase, due to the above-mentioned overestimation of the fluctuations within the RPA. In the more accurate fRG calculation the magnetic instability occurs at lower temperatures. The frequency structure in Fig. 2.8 for  $\Omega = 2\pi T$  is very similar to the one shown in Fig. 2.6. The simple contributions considered here reproduce the position of the main structures, as well as the correct sign of the charge channel. This is true also for the other bosonic Matsubara frequencies shown here, for which we do not report the fRG results. Furthermore, upon lowering the temperature the charge channel diverges also for other finite bosonic Matsubara frequencies, while it does not diverge for  $\Omega = 0$ . From this we conclude that the frequency dependent effective magnetic interaction described above is responsible for the frequency structure of the charge channel observed in the fRG.

To understand why the divergence appears for a non-zero frequency  $\Omega$ , we notice that in Eq. (2.15) the  $\Omega$  dependence appears only through the bubble  $\Pi_{\mathbf{Q},\Omega}(\nu)$ . The frequency summed particle-hole bubble obeys the following relation:

$$\Pi_{\mathbf{Q} \rightarrow (0,0), \Omega} = \sum_{\nu} \Pi_{\mathbf{Q} \rightarrow (0,0), \Omega}(\nu) = C \delta_{\Omega,0}, \quad (2.17)$$

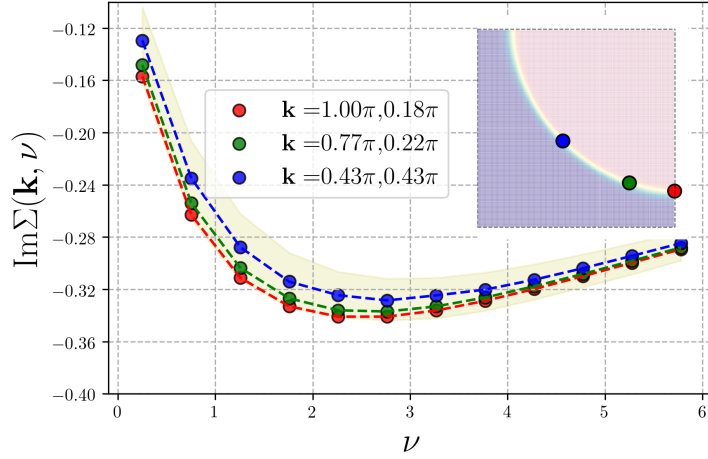
where  $C$  is a positive constant that, at low temperature, approaches the density of states at the Fermi level. In the bottom right panel of Fig. 2.8, we show the bubble  $\Pi_{\mathbf{Q}=(0,0),\Omega}(\nu)$  as a function of  $\nu$  for different values of  $\Omega$ . We note that it has a large negative peak for  $\Omega = 2\pi T$ . This is due to the property (2.17): the summed bubble must vanish for  $\Omega \neq 0$ , hence a large negative value is needed to cancel the positive contributions at large frequency. We have thus identified the origin of the frequency structure observed in the charge channel, which seems to be quite general since it arises from simple Feynman diagrams.

Including the self-energy in the calculation of the bubble, Eq. (2.17) does not evaluate to a  $\delta$ -function anymore, and the difference between the summed bubble at vanishing frequency and for frequency  $2\pi T$  is diminished. This is probably the reason why the inclusion of the self-energy feedback prevents the unphysical divergence of the charge channel.

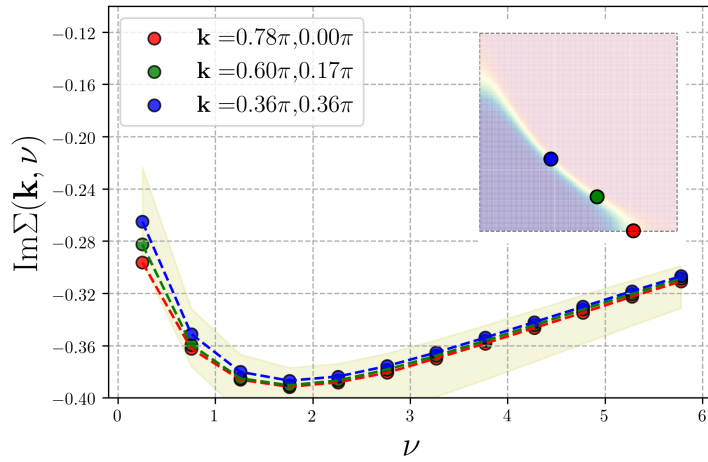
## 2.5 Self-energy and pseudogap

We now discuss the frequency and momentum dependence of the self-energy. In Fig. 2.9a we show the frequency dependence of the imaginary part of the self-energy at  $T = 0.08t$  and low doping  $x = 0.025$ . The spread between the maximal and minimal self-energy at each frequency is rather small, indicating that the self-energy did not develop a large momentum dependence even when the flow parameter reached the critical value  $\Lambda_c$ . At small frequencies the self-energy has a typical Fermi liquid behavior. One would generally expect the antinodal region to be more affected by correlation effects. However, there is only a slight increase of  $|\text{Im}\Sigma(\mathbf{k}, \nu)|$  in this region. At the temperature and interaction strength we are considering, we do not observe a tendency towards the opening of a momentum selective gap. In Fig. 2.9b we show the imaginary part of the self-energy for a larger doping  $x = 0.4$ . As in the previous case, we do not see much momentum differentiation.

The self-energy enters directly in the calculation of the momentum distribution through the Green's function, already discussed above, and shown in Figs. 2.4. In the bottom panels of these figures, we show how the momentum distribution evolves along two different cuts in the Brillouin zone, crossing the *nodal* and *antinodal* regions, respec-



(a)



(b)

Figure 2.9: Self-energy as a function of frequency for  $U = 4t$ ,  $t' = -0.32t$  at temperature  $T = 0.08t$ , for doping  $x = 0.025$  on the top and  $x = 0.4$  on the bottom. The location of the  $\mathbf{k}$ -point in the Brillouin zone is color coded in the inset. The position of all the patching points taken into account for the self-energy is calculated from the noninteracting Fermi-surface and is shown as black circles in the top row of Figs. 2.4, for instance, and does not change during the flow. The shaded area highlights the region between the maximal and minimal value of the self-energy for each frequency.

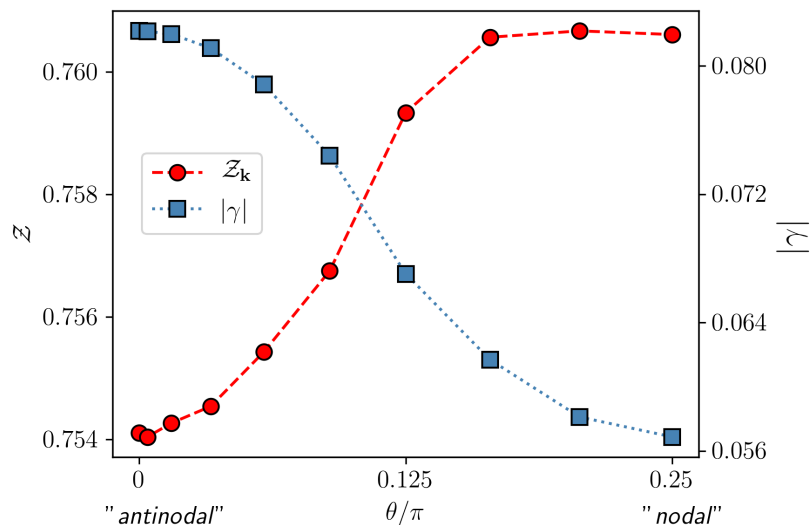


Figure 2.10: Quasiparticle weight  $Z_{\mathbf{k}}$  and decay rate  $\gamma_{\mathbf{k}}$  as function of the angle  $\theta$  for the same parameters as in Fig. 2.9a. The values on the left axis refer to the quasiparticle weight, the values on the right axis refer to the decay rate.

tively. The drop in the momentum distribution is sharper along the diagonal, and the self-energy effects are stronger along the antinodal cut. For doping  $x = 0.4$  the broadening of the Fermi surface, already larger at the non interacting level, is further enhanced by the self-energy.

To study further the difference between nodal and antinodal regions in the iAF regime, we studied the quasiparticle weight [68]  $Z_{\mathbf{k}}$ , and the decay rate  $\gamma_{\mathbf{k}}$ . Instead of relying on analytical continuation, we have extracted these parameters directly from the Matsubara frequencies data. We have fitted the first few frequencies of the imaginary part of the self-energy with a polynomial of degree  $l$ :  $\text{Im}\Sigma(\mathbf{k}, \nu) \approx a_0(\mathbf{k}) + a_1(\mathbf{k})\nu + \dots + a_l(\mathbf{k})\nu^l$  and we identified  $\gamma_{\mathbf{k}} = a_0(\mathbf{k})$  and  $Z_{\mathbf{k}} = [1 - a_1(\mathbf{k})]^{-1}$ . The procedure only works if the temperature is low enough, and if the frequencies used for the fit are not too high. We checked that the results were stable upon changing the number of frequencies and the order of the polynomial used for the fit. In Fig. 2.10 we plot  $Z_{\mathbf{k}}$  and  $\gamma_{\mathbf{k}}$  against the angle  $\theta$  along the Fermi surface,  $\theta = 0$  corresponding to the antinodal direction and  $\theta = \pi/4$  to the nodal one. The variation of the quasiparticle weight along the Fermi surface is extremely small with  $Z_{\mathbf{k}}$  assuming values between 0.754 and 0.760. On the other hand, the relative variation of the decay rate  $\gamma$  along the Fermi surface is sizable, varying from

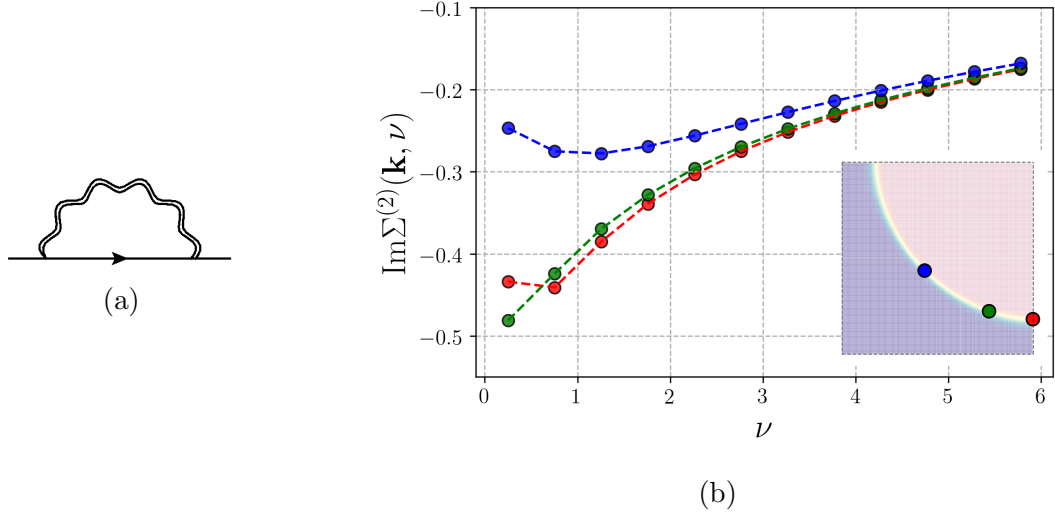


Figure 2.11: (a) Second order correction to the self-energy in spin fluctuations theories. The wavy line represents the spin susceptibility while the internal continuous line refers to the noninteracting propagator. (b) Self-energy computed with Eq. (2.18), or diagram (a). The spin susceptibility is computed with the vertex at the critical value  $\Lambda_c$ . The parameters are  $U = 4t$ ,  $T = 0.08t$ ,  $t' = -0.32t$  and doping  $x = 0.025$ , the same as in Fig. 2.9a. In the inset, the noninteracting momentum distribution is shown.

$\gamma \approx 0.056t$  to  $\gamma \approx 0.082t$ . These values are comparable to the temperature  $T = 0.08t$ .

Decay rates [88] and quasi-particle weights [89] were computed already in early fRG calculations from two-loop contributions to the self-energy, obtained by inserting the integrated one-loop equation for the vertex into the flow equation for the self-energy. In this way the computation of a frequency dependent vertex was avoided. The size and anisotropy of the decay rates obtained in these calculations are comparable to our results. The quasi-particle weight was even less reduced, but its anisotropy more pronounced, probably because the Fermi surface in Ref. [89] is more nested than ours and close to van Hove points.

We conclude that near the critical value  $\Lambda_c$  the system generically still has coherent quasiparticles along the Fermi surface, with a higher decay rate in the antinodal region. This is consistent with the results of Ref. [90], where non-Fermi liquid behavior of the self-energy was observed only very close to the pseudo-critical temperature and in the immediate vicinity of the magnetic hot spots.

We finally discuss the issue of pseudogap in our implementation of the flow equa-

tions. In fact, somewhat surprisingly, the self-energy in Fig. 2.9 does not show a significant momentum dependence. In both calculations the flow has been stopped due to an antiferromagnetic instability. In other methods, for instance the dynamical vertex approximation (D $\Gamma$ A) [91], diagrammatic Monte Carlo [92] and the dynamical cluster approximation (DCA) [46], close to an antiferromagnetic transition the quasi-particle spectral function shows a gap in the *antinodal* direction only, *i.e.* close to  $\mathbf{k} = (\pi, 0)$ . This specific momentum differentiation in the spectral function is associated with the pseudogap and has been observed in numerous experiments in cuprates [2, 5].

To understand the lack of pseudogap in our calculations, we mention here two particular approaches, the spin fluctuations theories [93, 94] and the two-particle self-consistent approach (TPSC) of Vilk and Tremblay [95], see also Ref. [96] in connection with the pseudogap. These approaches assume that the high energy spin fluctuations decouple and can be integrated out, leading to a low energy effective field theory. The second order correction for the self-energy for this effective model is given by [93, 96]

$$\Sigma^{(2)}(\mathbf{k}, i\nu) = U^2 \int_q G_0(\mathbf{q} + \mathbf{k}, i\omega + i\nu) \chi_s(\mathbf{q}, \omega). \quad (2.18)$$

The diagrammatic representation is shown in Fig. 2.11a. By using the Ornstein-Zernike form for the spin susceptibility [97, 98], Eq. (2.18) predicts a spectral gap only for momenta close to the hot-spots [95, 96].

Our results with the fRG flow, in Figs. 2.9a and 2.9b, show, instead, Fermi-liquid excitations on the whole Fermi-surface. In our implementation, the fRG involves two approximations: the level-2 truncation and the finite expansion in form factors. Although the self-energy flow equation is exact, an approximation to the vertex flow leads to a subsequent approximation to the self-energy flow.

For a better understanding, we can extract the spin susceptibility  $\chi_s(\mathbf{q}, \omega)$  from the fRG vertex function and substitute it in the second order self-energy (2.18). We use the vertex function at the critical value  $\Lambda_c$  and the standard diagrammatic expression for the susceptibilities. The resulting self-energy is shown in Fig. 2.11b, where we used the same parameter set used also in Fig. 2.9a. In this case, we can clearly see a tendency to a non Fermi-liquid behaviour for momenta  $\mathbf{k}$  close to the hot-spots and a strong reduction of the spectral weight in the antinodal direction. Moreover, we still observe Fermi-liquid excitations in the nodal direction, confirming the expected pseudogap picture.

However, the lack of pseudogap physics in the flow equation of the self-energy (1.36) remains, and this issue has still to be clarified.

# Dynamical effects on the nonlocal magnetic correlations

In the first chapter, we introduced the DMFT as a method able to investigate strong correlations effects at the local level. The DMFT self-consistency loop involves the calculation of one-particle quantities only, while many physical observables require the explicit calculation of the vertex function. In Section 1.2.4, we defined and discussed the local DMFT vertex function. Since the calculation of the DMFT vertex is computationally demanding, susceptibilities are often computed by a random-phase approximation (RPA) with DMFT propagators. This approach has frequently been applied to real materials, for example, to iron systems [99]. The importance of the vertex corrections for the frequency dependence of the *local* spin susceptibility has already been addressed in the context of iron pnictides [100, 101].

Here, we consider the 2D Hubbard model. The effects of the DMFT vertex on charge correlations has been studied at half-filling by Hafermann *et al.* [86], who focused also on gauge invariance from a more fundamental perspective. Instead, we concentrate on the nonlocal spin correlations away from half-filling. As we shall show, although being local in space, the DMFT vertex strongly changes the momentum dependence of the spin susceptibility.

The vertex corrections do not only affect the Néel temperature, but also the wave vector of the dominant magnetic instability. Via its frequency dependence, the DMFT vertex alters the momentum dependence of the susceptibility as compared to the momentum dependence of the RPA susceptibility with the particle-hole bubble dressed by the self-energy only. In large parts of the phase diagram, the RPA susceptibility is maximal at a wave vector  $(\pi, \pi)$ , predicting Néel-type commensurate antiferromagnetic order,

while the susceptibility computed with vertex corrections exhibits pronounced maxima at incommensurate wave vectors on the Brillouin zone (BZ) boundary away from  $(\pi, \pi)$ . The results reported in this chapter are also shown in the peer reviewed paper [102].

### 3.1 Bethe-Salpeter equations and nonlocal spin susceptibility

In Section 1.2.4 we discussed the local DMFT vertex function  $V_{\sigma_1, \sigma_2, \sigma_3, \sigma_4}(\nu_1, \nu_2, \nu_3)$ . Here, we introduce the Bethe-Salpeter equations as a method to generate the momentum dependence of the vertex by using a ladder summation. For our scope, we select the particle-hole direct channel and the magnetic component  $V^m = V_{\uparrow\uparrow\uparrow} - V_{\uparrow\downarrow\downarrow}$ . A generalization to pairing and charge components can be found in Refs. [54] and [86].

The local Bethe-Salpeter equation in the particle-hole channel reads [54]

$$V_{\omega}^m(\nu_1, \nu_2) = \Gamma_{\omega}^m(\nu_1, \nu_2) - T \sum_{\nu} \Gamma_{\omega}^m(\nu_1, \nu) \chi_{\omega}^{0, \text{loc}}(\nu) V_{\omega}^m(\nu, \nu_2), \quad (3.1)$$

where we used  $\chi_{\omega}^{0, \text{loc}}(\nu) = -G(\nu)G(\omega + \nu)$  and the notation  $V_{\omega}(\nu_1, \nu_2) \equiv V(\nu_1, \nu_2, \omega + \nu_1)$ . The new object  $\Gamma^m$  contains two-particle irreducible (2PI) diagrams in the particle-hole channel. We are now able to write the nonlocal version of the Bethe-Salpeter for the nonlocal vertex function  $V_{\mathbf{q}}^m$

$$V_{\mathbf{q}, \omega}^m(\nu_1, \nu_2) = \Gamma_{\omega}^m(\nu_1, \nu_2) - T \sum_{\nu} \Gamma_{\omega}^m(\nu_1, \nu) \chi_{\mathbf{q}, \omega}^0(\nu) V_{\mathbf{q}, \omega}^m(\nu, \nu_2), \quad (3.2)$$

with

$$\chi_{\mathbf{q}, \omega}^0(\nu) = - \int_{\mathbf{k}} G(\mathbf{k}, \nu) G(\mathbf{q} + \mathbf{k}, \omega + \nu). \quad (3.3)$$

Here,  $G^{-1}(\mathbf{k}, \nu) = i\nu - \epsilon_{\mathbf{k}} + \mu - \Sigma_{\text{dmft}}(\nu)$ . By solving Eqs. (3.1) and then (3.2), we obtain the nonlocal vertex function  $V_{\mathbf{q}}^m$ . From a diagrammatic point of view, the combination of the *local* and *nonlocal* Bethe-Salpeter equations, Eqs. (3.1) and (3.2), provides a consistent ladder summation without double counting of equivalent diagrams. The

relations (3.1) and (3.2) can be combined into a single equation

$$V_{\mathbf{q},\omega}^m(\nu_1, \nu_2) = V_{\omega}^m(\nu_1, \nu_2) - T \sum_{\nu} V_{\omega}^m(\nu_1, \nu) [\chi_{\mathbf{q},\omega}^0(\nu) - \chi_{\omega}^{0,\text{loc}}(\nu)] V_{\mathbf{q},\omega}^m(\nu, \nu_2). \quad (3.4)$$

In the next section, we show the effect of the local DMFT vertex to nonlocal magnetic properties. We discuss here the momentum dependent magnetic susceptibility with local vertex corrections. We start by mentioning the exact formula for the spin susceptibility as

$$\chi_{\mathbf{q},\omega} = \int_{\mathbf{k},\nu} \chi_{\mathbf{q},\omega}(\mathbf{k}, \nu), \quad (3.5)$$

where

$$\chi_{\mathbf{q},\omega}(\mathbf{k}, \nu) = \chi_{\mathbf{q},\omega}^0(\mathbf{k}, \nu) - \chi_{\mathbf{q},\omega}^0(\mathbf{k}, \nu) \int_{\mathbf{k}',\nu'} \Gamma_{\mathbf{k},\omega}^m(\nu, \nu', \mathbf{k}, \mathbf{k}') \chi_{\mathbf{q},\omega}(\mathbf{k}', \nu'). \quad (3.6)$$

We used the particle-hole notation of Rohringer *et al.* [54] and the summation  $\int_{\mathbf{k},\nu} = T \sum_{\nu} \int \frac{d\mathbf{k}}{(2\pi)^2}$  is understood.  $\Gamma^m$  is the two-particle irreducible vertex in the magnetic channel and corresponds to the magnetic antisymmetric spin combination  $\Gamma_{\uparrow\uparrow\uparrow\uparrow} - \Gamma_{\uparrow\downarrow\uparrow\downarrow}$ .

Due to the computationally demanding calculation of the DMFT vertex function, the spin susceptibility is often computed with a RPA formula, obtained by replacing the irreducible vertex with the lowest order in perturbation theory  $\Gamma_{\mathbf{k},\omega}^m(\nu, \nu', \mathbf{k}, \mathbf{k}') = -U$

$$\chi_{\mathbf{q},\omega}^{\text{RPA}} = \frac{\chi_{\mathbf{q},\omega}^0}{1 - U\chi_{\mathbf{q},\omega}^0}, \quad (3.7)$$

where

$$\chi_{\mathbf{q},\omega}^0 = T \sum_{\nu} \chi_{\mathbf{q},\omega}^0(\nu) = -T \sum_{\nu} \int_{\mathbf{k}} G(\mathbf{k}, \nu) G(\mathbf{q} + \mathbf{k}, \omega + \nu) \quad (3.8)$$

is the polarization function, or particle-hole bubble. In this context we consider the Green's function dressed by the DMFT self-energy. The symmetric phase is stable only if the denominator in Eq. (3.7) is positive. A vanishing denominator for  $\omega = 0$  at a certain wave vector  $\mathbf{q}$  signals a magnetic instability. The specific structure of the Eq. (3.7) implies that the RPA susceptibility  $\chi^{\text{RPA}}$  and the bubble  $\chi^0$  have the same maximum in momentum space. As a consequence, in a RPA approach the nonlocal spin correlations are completely determined by the momentum dependence of the bubble itself.

The RPA formula (3.7) can be improved by including the DMFT local vertex correc-

tion

$$\chi_{\mathbf{q},\omega} = T \sum_{\nu_1, \nu_2} (D_{\mathbf{q},\omega}^{-1})^{\nu_1, \nu_2} \chi_{\mathbf{q},\omega}^0(\nu_2) \quad (3.9)$$

where  $D_{\mathbf{q},\omega}^{\nu_1, \nu_2} = \delta_{\nu_1, \nu_2} + T \chi_{\mathbf{q},\omega}^0(\nu_1) \Gamma_{\omega}^m(\nu_1, \nu_2)$ .

As discussed in Section 1.2.3, contrary to the local susceptibility, the nonlocal spin response function (3.9) diverges at finite temperature signaling an antiferromagnetic instability.

In the next section, we calculate the spin susceptibility with the DMFT vertex corrections for different finite doping values and a finite  $t'$ . We will show that, although the DMFT includes only local contributions, the vertex strongly affects also the momentum dependence of the susceptibility.

## 3.2 Dynamical vertex corrections to magnetic susceptibility

In this section, we analyze how local corrections affect nonlocal magnetic properties. First, since we concentrate on the magnetic ordering wave vector  $\mathbf{q} = (\pi, \pi - 2\pi\eta)$ , we introduce the *incommensurability factor*  $\eta$  that is determined by the maximum in the BZ of the static spin susceptibility  $\chi_{\mathbf{q},\omega=0}$ .

We use the formula (3.7) to compute the RPA spin susceptibility  $\chi_{\mathbf{q},\omega}^{\text{RPA}}$ , where the particle-hole bubble  $\chi_{\mathbf{q},\omega}^0$  in Eq. (3.8) is computed with the DMFT self-energy feedback. Note that, due to the specific structure of Eq. (3.7), the RPA susceptibility  $\chi^{\text{RPA}}$  and the bubble  $\chi^0$  have the same maximum in momentum space. As a consequence, the incommensurability factor  $\eta$  in RPA is completely determined by the momentum dependence of the bubble itself.

We use Eq. (3.9) for the DMFT susceptibility  $\chi_{\mathbf{q},\omega}$ . Note that  $\chi_{\mathbf{q},\omega}$  in Eq. (3.9) includes local correlations both at the two-particle level with the DMFT vertex but also at the one-particle level with the inclusion of the DMFT self-energy in the bubble. Since the vertex is local, in Eq. 3.9 the momentum dependence of the susceptibility is generated by the particle-hole propagator. However, we will see that, due to the convolution with the frequency dependent vertex, the momentum dependence of the susceptibility does not simply trace the momentum dependence of the bubble as in the RPA.

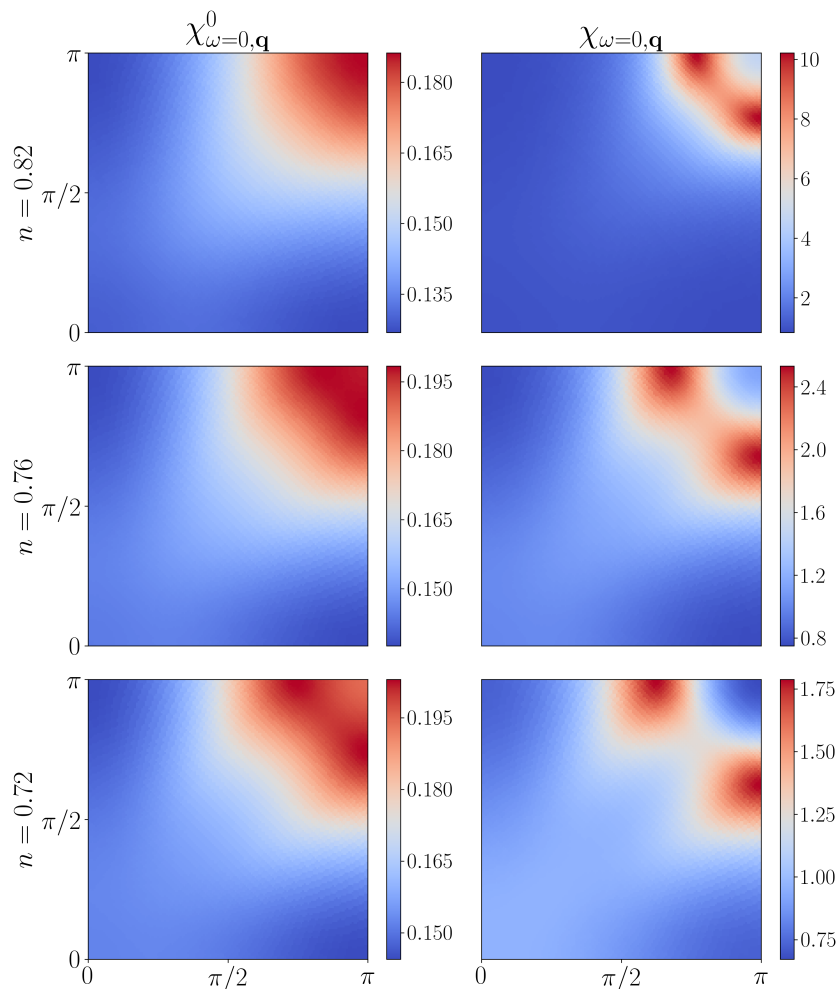


Figure 3.1: Static particle-hole bubble (left) and static susceptibility (right) as a function of momentum in the first quadrant of the BZ. From top to bottom results for various densities are shown:  $n = 0.82$ ,  $n = 0.76$  and  $n = 0.72$ . The other parameters are  $U = 8t$ ,  $t' = -0.2t$ , and  $T = 0.08t$ .

In Fig. 3.1 we show results for the static particle-hole bubble (left column) and the static DMFT susceptibility (right column) as a function of momentum in the first quadrant of the Brillouin zone (BZ) for various fermion densities  $n < 1$ . All quantities are computed for  $t = 1$ . The interaction is rather strong ( $U = 8t$ ), and the temperature  $T = 0.08t$  has been chosen within the paramagnetic regime, that is, above the critical temperature for a magnetic instability (within DMFT). One can clearly see that the positions of the maxima of the bubble and the susceptibility are generally distinct; in

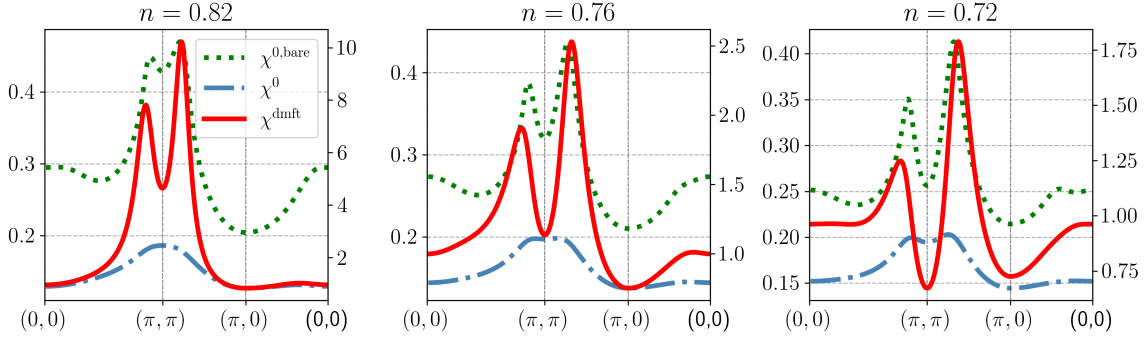


Figure 3.2: Bare bubble (dotted line), DMFT bubble (dot-dashed line) and DMFT susceptibility (continuous line) plotted along a specific path in the BZ for  $U = 8t$ ,  $t' = -0.2t$ , and  $T = 0.08t$ . From left to right:  $n = 0.82$ ,  $n = 0.76$  and  $n = 0.72$ . The numbers on the left y-axes refer to both bare and DMFT bubble, while the numbers on the right y-axes refer to the susceptibility.

particular, for  $n = 0.82$ , the maximum of the bubble is located at  $\mathbf{q} = (\pi, \pi)$ , while the DMFT susceptibility shows maxima for incommensurate vectors  $\mathbf{q} = (\pi, \pi - 2\pi\eta)$  and  $\mathbf{q} = (\pi - 2\pi\eta, \pi)$ , with  $\eta \approx 0.12$ .

Hence, for  $n = 0.82$ , the widely used RPA formula (3.7) yields dominant commensurate antiferromagnetic correlations, since the momentum dependence of the RPA susceptibility is entirely determined by the particle-hole bubble. In this approximation the local correlations are taken into account only at the one-particle level, through the inclusion of the self-energy. The behavior changes drastically when the local fluctuations are considered also at the two-particle level by including the DMFT vertex. The results for the susceptibility in the right panel of Fig. 3.1 exhibit dominant incommensurate spin correlations for all shown densities. For  $n = 0.76$ , both the particle-hole bubble and the susceptibility have incommensurate maxima, but at different positions. Reducing the filling further to  $n = 0.72$ , the momentum  $(\pi, \pi)$  becomes a marked local minimum for the bubble and even a global minimum for the DMFT susceptibility.

The peak structure of the bubble and the susceptibility can be seen more clearly when plotted along a specific path in the BZ, as shown in Fig. 3.2. Here, it is evident that  $(\pi, \pi)$  becomes a global minimum for the susceptibility at filling  $n = 0.72$ . In this plot we also show the *bare* bubble  $\chi_{0,\text{bare}}$ , which is computed without self-energy feedback and with the bare chemical potential.

Despite the fact that the bare bubble does not enter in Eqs. (3.7) and (3.9), since

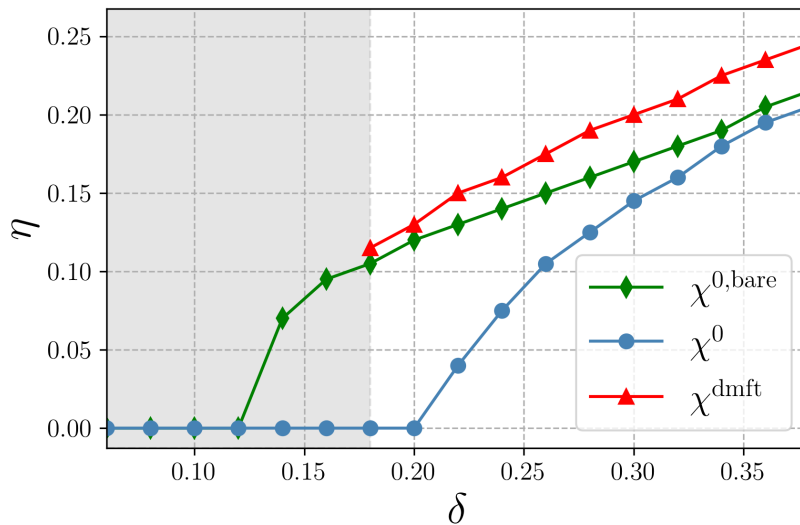


Figure 3.3: Incommensurability  $\eta$  as a function of the doping  $\delta = 1 - n$ , for  $U = 8t$ ,  $t' = -0.2t$ , and  $T = 0.08t$ . The different curves refer to the DMFT susceptibility, the DMFT bubble with self-energy, and the bare bubble, respectively. The grey area indicates the doping values where Eq. (3.9) has no solution, due to a magnetic instability in that regime.

$\chi_0$  is evaluated with self-energy feedback, the momentum dependence of the DMFT susceptibility resembles much more the one of the bare bubble rather than the bubble with dressed propagator. This is remarkable since the self-energy strongly affects the particle-hole bubble: first, as expected, the self-energy globally suppresses the bubble; second, and more importantly, it smears the peaks in momentum space and thus reduces or even eliminates the shift  $\eta$ . By contrast, the two-particle vertex has the opposite effect: it sharpens the peak and increases  $\eta$ .

To study further the relation between the particle-hole bubble and the DMFT susceptibility, in Fig. 3.3 we show the corresponding incommensurabilities  $\eta$  as function of the doping  $\delta = 1 - n$ . The maximum of the dressed particle-hole bubble stays at  $(\pi, \pi)$  for doping smaller than 0.2, and moves away from  $(\pi, \pi)$  only for  $\delta > 0.2$ . On the other hand, the incommensurability vector of the DMFT susceptibility is finite already for doping  $x = 0.14$ , and is always larger than the one of the particle-hole bubble. In the paramagnetic regime where the DMFT susceptibility is well defined, the incommensurability vector of  $\chi$  is quite close to the one obtained from the *bare* bubble. When

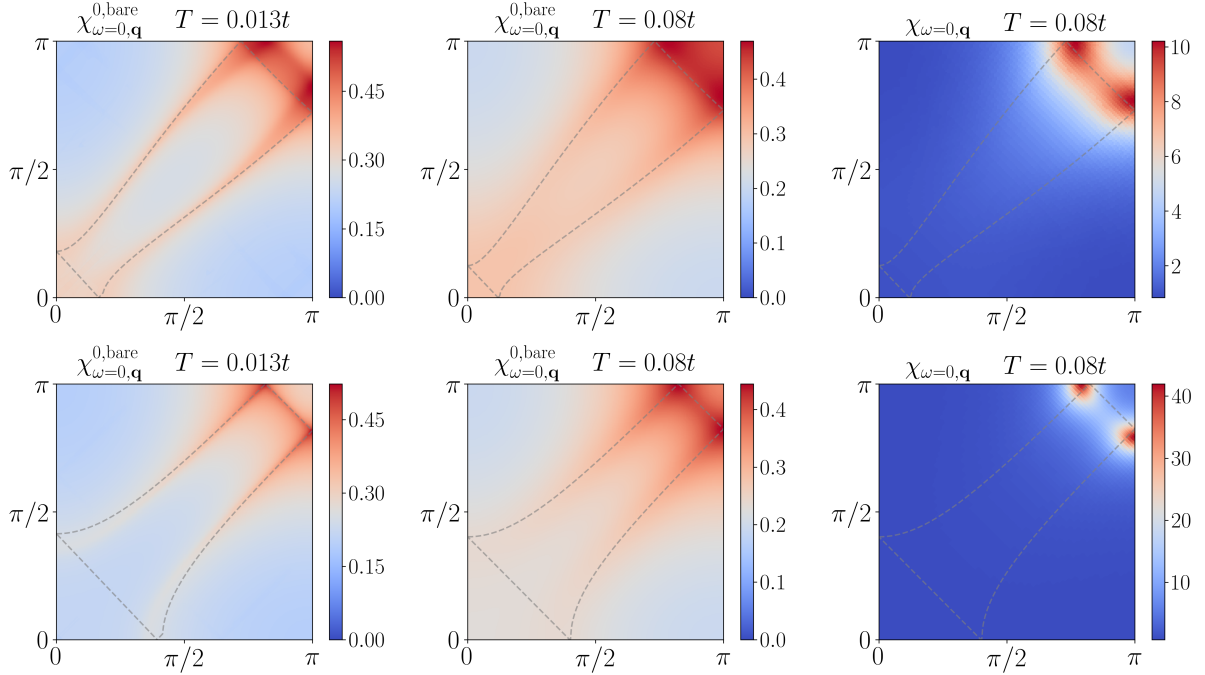


Figure 3.4: From left to right, bare bubble at  $T = 0.013t$ , bare bubble at  $T = 0.08t$ , and susceptibility at  $T = 0.08t$  as a function of momentum for  $U = 8t$  and  $n = 0.82$ . Top:  $t' = -0.2t$ , bottom:  $t' = -0.08t$ . The dashed lines represent the nesting vectors of the Fermi surface as explained in Ref. [103].

the doping is increased, the difference between the incommensurability of the dressed bubble and of the susceptibility is gradually reduced. Similar results are obtained for  $t' = -0.08t$ .

The position of the peaks of the bare particle-hole bubble at low temperatures is determined by crossing points of *nesting-lines* (or " $2k_F$ -lines") in the BZ (see, for example, Ref. [103]). The latter are lines formed by the set of all nesting vectors of the Fermi surface, which connect Fermi momenta with collinear Fermi velocities. The smearing effect of the self-energy on the bubble spoils the connection with the Fermi surface geometry. Since the vertex correction strongly affects the momentum dependence of the susceptibility, the question arises whether the vertex restores a connection between the susceptibility and the Fermi surface.

To further investigate this point, in Fig. 3.4 we plot the susceptibility at  $T = 0.08t$ , already shown in previous plots, together with the bare bubble at the same temperature,

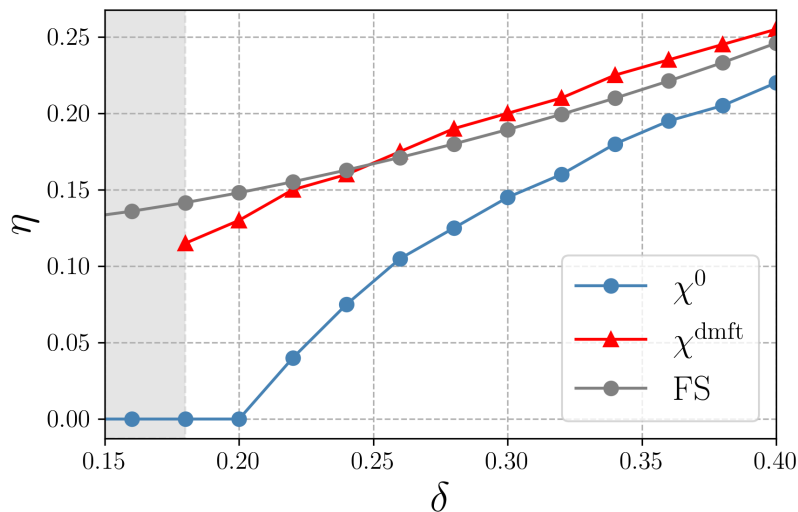


Figure 3.5: Incommensurability  $\eta$  as a function of the doping  $\delta = 1 - n$ , for  $U = 8t$ ,  $t' = -0.2t$ , and  $T = 0.08t$ . The different curves refer to the DMFT susceptibility, the bubble  $\chi^0$  with DMFT self-energy, and the  $\eta_{\text{FS}}$  as in Eq. (3.10).

and also at a lower temperature  $T = 0.013t$ , where the signature of the Fermi surface is more pronounced. Structures along the nesting-lines parallel to the BZ diagonals are visible only in the bubble, not in the susceptibility. However, the positions of the incommensurate peaks near the crossing points of nesting lines on the BZ boundary are quite similar in both quantities. This similarity suggests a connection between the peaks in the DMFT susceptibility and the Fermi surface geometry.

By following Ref. [103], we calculate analytically the incommensurability factor  $\eta$  predicted by the Fermi surface geometry as

$$\eta_{\text{FS}} = \frac{1}{2} - \frac{1}{\pi} \arccos\left(-\frac{\mu}{2t}\right). \quad (3.10)$$

In Fig. 3.5 we compare the doping dependence of  $\eta_{\text{FS}}$  with the incommensurability factors extracted from the DMFT susceptibility and the DMFT bubble, shown also in Fig. 3.3. The incommensurability  $\eta_{\text{FS}}$ , represented with grey points, follows the doping dependence of the peak positions in the DMFT susceptibility. This comparison supports the connection between the DMFT susceptibility with vertex corrections and the Fermi surface geometry.



# Magnetic and superconducting correlations with the fRG at strong coupling

As explained in Chapter 1, Taranto *et al.* [53] managed to combine the strengths of the DMFT and the fRG in a new computational method, the DMF<sup>2</sup>RG. Due to the truncated field expansion, the fRG is limited to weak-to-moderate interactions [20]. For instance, the fRG equations used so far do not capture the Mott metal-insulator transition, which plays a crucial role in the strongly interacting Hubbard model. On the other side, this transition is well described by the DMFT, which captures strong *local* correlations effects.

In this chapter, we apply the DMF<sup>2</sup>RG to the 2D Hubbard model. Taranto *et al.* [53] used a channel decomposition [29, 34] to simplify the frequency dependence of the vertex function to one frequency variable in each channel. This approximation limited the application of the DMF<sup>2</sup>RG to the weak-to-moderate coupling regime. The momentum dependences of the vertex and the self-energy were computed only at half-filling for moderate coupling strengths [53].

At strong coupling, the vertex exhibits frequency dependences which cannot be reduced to one frequency per interaction channel [54]. In the fRG, non-separable frequency dependences are generated even at moderate coupling, see Chapter 2. Hence, we apply the DMF<sup>2</sup>RG by requiring an accurate parametrization of the full frequency dependence of the vertex.

In the first part of this chapter, we focus on methodological aspects. Here we describe our parametrization of the two-particle vertex and the flow equations for the interacting channels. In addition to a more accurate parametrization of the vertex, a major advance

compared to the first version of the DMF<sup>2</sup>RG is a setup of the flow that conserves local correlations (already captured by the DMFT). In other words, only nonlocal correlations are generated by the flow. This substantially improves the accuracy of the unavoidable truncation of the flow hierarchy.

In the second part, we present results obtained from the DMF<sup>2</sup>RG for the two-dimensional Hubbard model at strong coupling, in the parameter regime that applies to cuprates. The fRG hierarchy is truncated at the two-particle level, that is, only the influence of nonlocal three-particle interactions (and beyond) is neglected. The momentum dependence of the two-particle vertex is approximated by *s*-wave and *d*-wave form factors. All calculations are carried out at finite temperature, the lowest temperatures reached are two orders of magnitude smaller than the band width. Antiferromagnetic fluctuations dominate over a wide doping range. They are of Néel type at half-filling, but incommensurate for a sizable doping. Strong *d*-wave pairing correlations emerge at the edge of the antiferromagnetic regime. For the lowest temperature we can reach, the model is very close to a superconducting instability. The pairing mechanism is clearly magnetic, similar to the mechanism at weak coupling as seen in the plain fRG [20].

## 4.1 Vertex parametrization

In Chapter 1, we derived the flow equations for the self-energy  $\Sigma^\Lambda(k)$ , (1.36), and the vertex  $V^\Lambda(k_1, k_2, k_3)$ , (1.35), whose initial conditions are determined by the DMFT solution. These are the DMFT self-energy, Eq. (1.57), and the DMFT vertex, Eq. (1.58). We parametrize the vertex function by extending the channel decomposition introduced by Husemann and Salmhofer[33].

The function  $V^\Lambda(k_1, k_2, k_3)$  is decomposed as

$$\begin{aligned}
 V^\Lambda(k_1, k_2, k_3) = & V_{\text{dmft}}(\nu_1, \nu_2, \nu_3) - \phi_p^\Lambda(k_1 + k_2; k_1, k_3) + \phi_m^\Lambda(k_2 - k_3; k_1, k_2) \\
 & + \frac{1}{2}\phi_m^\Lambda(k_3 - k_1; k_1, k_2) - \frac{1}{2}\phi_c^\Lambda(k_3 - k_1; k_1, k_2), \quad (4.1)
 \end{aligned}$$

in terms of the DMFT vertex, the *pairing* channel  $\phi_p$ , the *magnetic* channel  $\phi_m$  and the *charge* channel  $\phi_c$ . Note that in Ref. [53] the vertex has been decomposed in terms of the bare interaction and fluctuating channels, each with a simplified frequency depen-

dence. In this way, the frequency dependence of the DMFT vertex is not fully captured, restricting the validity to the weak-to-intermediate coupling range. Here we overcome this limitation by considering the full frequency dependence of the DMFT vertex. As a consequence, the functions  $\phi_x$  are associated with nonlocal fluctuations beyond the DMFT solution, since the local pairing, magnetic and charge fluctuations are already captured by the DMFT vertex. The initial condition for the vertex determines the starting conditions for the channels as  $\phi_p^{\Lambda\text{ini}} = \phi_c^{\Lambda\text{ini}} = \phi_m^{\Lambda\text{ini}} = 0$ .

To derive the flow equations for the interacting channels, we substitute Eq. (4.1) into Eq. (1.35a) and derive the equations for  $\phi_x$  as

$$\dot{\phi}_p^\Lambda(Q; k_1, k_3) = -\mathcal{T}_{pp}^\Lambda(k_1, Q - k_1, k_3), \quad (4.2)$$

$$\dot{\phi}_c^\Lambda(Q; k_1, k_2) = \mathcal{T}_{phc}^\Lambda(k_1, k_2, k_2 - Q) - 2\mathcal{T}_{ph}^\Lambda(k_1, k_2, Q + k_1), \quad (4.3)$$

$$\dot{\phi}_m^\Lambda(Q; k_1, k_2) = \mathcal{T}_{phc}^\Lambda(k_1, k_2, k_2 - Q). \quad (4.4)$$

While keeping the entire frequency dependence for each channel, we treat the  $\mathbf{Q}$  momentum dependence with a patch scheme, see Appendix B, and the momenta  $\mathbf{k}_1$ ,  $\mathbf{k}_2$  and  $\mathbf{k}_3$  by using an orthonormal set of form factors  $f_l(\mathbf{k})$ . For the charge and magnetic channels we keep only  $f_s(\mathbf{k}) = 1$ , while for the pairing channel we use  $f_s(\mathbf{k}) = 1$  and  $f_d(\mathbf{k}) = \cos k_x - \cos k_y$

$$\phi_p^\Lambda(Q; k_1, k_3) = \mathcal{S}_{\mathbf{Q},\Omega}^\Lambda(\nu_1, \nu_3) + f_d\left(\frac{\mathbf{Q}}{2} - \mathbf{k}_1\right) f_d\left(\frac{\mathbf{Q}}{2} - \mathbf{k}_3\right) \mathcal{D}_{\mathbf{Q},\Omega}^\Lambda(\nu_1, \nu_3), \quad (4.5)$$

$$\phi_c^\Lambda(Q; k_1, k_2) = \mathcal{C}_{\mathbf{Q},\Omega}^\Lambda(\nu_1, \nu_2), \quad (4.6)$$

$$\phi_m^\Lambda(Q; k_1, k_2) = \mathcal{M}_{\mathbf{Q},\Omega}^\Lambda(\nu_1, \nu_2). \quad (4.7)$$

As we shall see, simplifying the channels to functions of a single linear combination of frequencies restricts the validity to the weak-to-intermediate coupling range, while the aim of the present formalism is to describe strong coupling correlation effects. The flow equations for  $\mathcal{C}$ ,  $\mathcal{M}$ ,  $\mathcal{S}$  and  $\mathcal{D}$  can now be derived by inserting Eqs. (4.5), (4.6) and (4.7) into Eqs. (4.2), (4.3) and (4.4), respectively, and then by projecting onto form factors. The final equations for all the channels are derived and shown in Appendix A. For later

use, we report here the flow equation for the magnetic channel  $\mathcal{M}$

$$\dot{\mathcal{M}}_{\mathbf{Q},\Omega}^{\Lambda}(\nu_1, \nu_2) = -T \sum_{\nu} L_{\mathbf{Q},\Omega}^{\text{m},\Lambda}(\nu_1, \nu) P_{\mathbf{Q},\Omega}^{\Lambda}(\nu) L_{\mathbf{Q},\Omega}^{\text{m},\Lambda}(\nu, \nu_2 - \Omega), \quad (4.8)$$

with

$$P_{\mathbf{Q},\Omega}^{\Lambda}(\omega) = \int_{\mathbf{p}} G^{\Lambda}(\mathbf{p}, \omega) S^{\Lambda}(\mathbf{Q} + \mathbf{p}, \Omega + \omega) + G^{\Lambda}(\mathbf{Q} + \mathbf{p}, \Omega + \omega) S^{\Lambda}(\mathbf{p}, \omega), \quad (4.9)$$

and

$$\begin{aligned} L_{\mathbf{Q},\Omega}^{\text{m},\Lambda}(\nu_1, \nu_2) = & V_{\text{dmft}}(\nu_1, \nu_2, \nu_2 - \Omega) + \mathcal{M}_{\mathbf{Q},\Omega}^{\Lambda}(\nu_1, \nu_2) \\ & + \int_{\mathbf{p}} \left\{ -\mathcal{S}_{\mathbf{p},\nu_1+\nu_2}^{\Lambda}(\nu_1, \nu_1 + \Omega) - \frac{1}{2} \mathcal{D}_{\mathbf{p},\nu_1+\nu_2}^{\Lambda}(\nu_1, \nu_1 + \Omega) [\cos(Q_x) + \cos(Q_y)] \right. \\ & \left. + \frac{1}{2} \left[ \mathcal{M}_{\mathbf{p},\nu_2-\nu_1-\Omega}^{\Lambda}(\nu_1, \nu_2) - \mathcal{C}_{\mathbf{p},\nu_2-\nu_1-\Omega}^{\Lambda}(\nu_1, \nu_2) \right] \right\}. \end{aligned} \quad (4.10)$$

## 4.2 DMFT conserving scheme

In order to compute the flow equations, we have to specify the  $\Lambda$  dependence of the bare propagator  $G_0^{\Lambda}$ . In the DMF<sup>2</sup>RG,  $G_0^{\Lambda}$  has to fulfil condition (1.54), *i.e.* it has to interpolate between the Weiss propagator  $\mathcal{G}_0(\nu)$  and the lattice noninteracting Green's function  $G_0(\mathbf{k}, \nu)$ . Here, we choose  $G_0^{\Lambda}$  such that

$$G_{\text{loc}}^{\Lambda}(\nu)|_{\Sigma^{\Lambda}=\Sigma_{\text{dmft}}} = \int_{\mathbf{k}} G^{\Lambda}(\mathbf{k}, \nu)|_{\Sigma^{\Lambda}=\Sigma_{\text{dmft}}} = G_{\text{dmft}}(\nu) \quad (4.11)$$

is independent of  $\Lambda$ , and thus determined by the local propagator as obtained from the DMFT. Note that in Ref. [53] the condition (4.11) is satisfied only at initial and final steps. Instead, we require here that the DMFT self-consistency relation is conserved also during the flow.

Condition (4.11) can be achieved by the following ansatz

$$G_0^{\Lambda}(\mathbf{k}, \nu) = \frac{1}{i\nu + \mu - (1 - \Lambda)\epsilon_{\mathbf{k}} - g_{\Lambda}(\nu)\Delta(\nu)}, \quad (4.12)$$

where we introduced the hybridization function  $\Delta(\nu) = i\nu + \mu - \mathcal{G}_0^{-1}(\nu)$  and the function

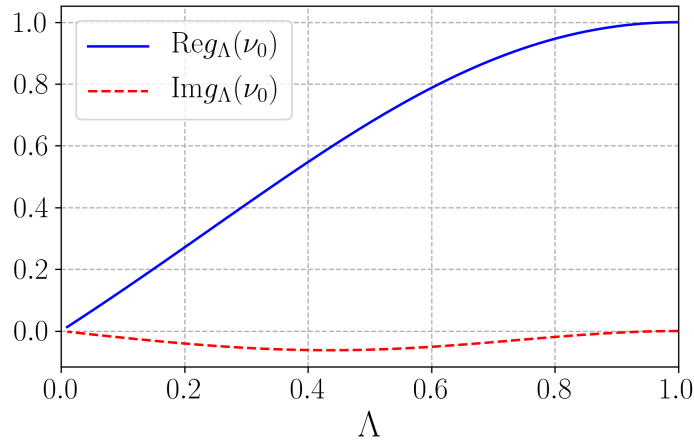


Figure 4.1:  $g_\Lambda(\nu)$  as a function of  $\Lambda$  for the first Matsubara frequency  $\nu_0 = \pi T$ . Parameters are  $n = 0.82$ ,  $U = 8t$ ,  $T = 0.08t$  and  $t' = -0.2t$ .

$g_\Lambda(\nu)$  which has to be determined from Eq. (4.11). The initial and final flow parameters are  $\Lambda_{\text{ini}} = 1$  and  $\Lambda_{\text{fin}} = 0$ ; in these cases, we have  $g_{\Lambda_{\text{ini}}}(\nu) = 1$  and  $g_{\Lambda_{\text{fin}}}(\nu) = 0$ . The value of the chemical potential  $\mu$  is fixed during the flow and is determined by the DMFT solution. The simple choice, for instance,  $g_\Lambda(\nu) = \Lambda$ , yields the flow scheme used in Ref. [53].

By inserting Eq. (4.12) into Eq. (4.11), we have

$$\int_{\mathbf{k}} \frac{1}{i\nu + \mu - (1 - \Lambda)\epsilon_{\mathbf{k}} - g_\Lambda(\nu)\Delta(\nu) - \Sigma_{\text{dmft}}(\nu)} = [\mathcal{G}_0^{-1}(\nu) - \Sigma_{\text{dmft}}(\nu)]^{-1}, \quad (4.13)$$

which represents an equation for  $g_\Lambda(\nu)$  and can be solved numerically by the bisection method for a given  $\Lambda$ .

In Fig. 4.1, we show  $g_\Lambda(\nu)$  as a function of  $\Lambda$  for the first Matsubara frequency  $\nu_0 = \pi T$  and filling  $n = 0.82$ . We observed that  $g_\Lambda(\nu)$  at fixed  $\Lambda$  is almost constant in frequency space.  $g_\Lambda(\nu)$  fulfils the same symmetry properties of the self-energy.

From Eq. (4.12), we are able to calculate the single-scale propagator as

$$S^\Lambda = -G^\Lambda \frac{dG_0^{\Lambda^{-1}}}{d\Lambda} G^\Lambda = -G^\Lambda \left[ \epsilon_{\mathbf{k}} - \Delta \frac{dg_\Lambda}{d\Lambda} \right] G^\Lambda. \quad (4.14)$$

The function  $dg_\Lambda/d\Lambda$  can be easily determined by taking the  $\Lambda$ -derivative of Eq. (4.11).

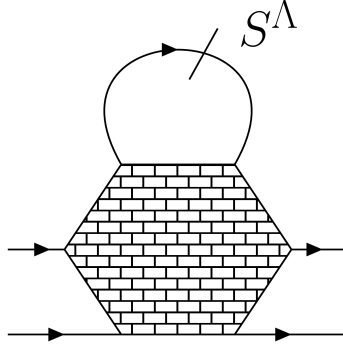


Figure 4.2: Diagram contributing to the vertex flow equation neglected in the level-2 truncation. The fermionic internal line refers to the single-scale propagator  $S^\Lambda$ . The hexagon corresponds to the three-particle vertex  $V^{(6)\Lambda}$ .

We now comment on the necessity of fixing the DMFT self-consistency relation during the flow. This condition conserves the DMFT solution and reduces the truncation error of the flow equations. To clarify this point, we mention here, in a more compact form, the neglected contribution to the vertex flow equation, Eq. (1.29), as

$$\mathcal{T}^{V_6} = -S^\Lambda \circ V^{(6)\Lambda}, \quad (4.15)$$

where  $V^{(6)\Lambda}$  is the three-particle vertex. Its diagrammatic representation is shown in Fig. 4.2.

In this context, we separate the self-energy and the three-particle vertex into DMFT contribution and a nonlocal part as

$$\Sigma^\Lambda = \Sigma_{\text{dmft}} + \delta\Sigma^\Lambda, \quad (4.16)$$

$$V^{(6)\Lambda} = V_{\text{dmft}}^{(6)} + \delta V^{(6)\Lambda}. \quad (4.17)$$

By expanding the Green's function in a geometric series ( $G_{\text{dmft}}^\Lambda = G^\Lambda|_{\Sigma=\Sigma_{\text{dmft}}}$ )

$$G^\Lambda = \frac{1}{G_0^{\Lambda-1} - \Sigma_{\text{dmft}} - \delta\Sigma^\Lambda} = G_{\text{dmft}}^\Lambda \sum_{l=0}^{\infty} [G_{\text{dmft}}^\Lambda \delta\Sigma^\Lambda]^l, \quad (4.18)$$

we write the single-scale propagator as

$$S^\Lambda = S_{\text{dmft}}^\Lambda + \delta S^\Lambda, \quad (4.19a)$$

where

$$S_{\text{dmft}}^\Lambda = S^\Lambda \Big|_{\Sigma=\Sigma_{\text{dmft}}} = \frac{dG_{\text{dmft}}^\Lambda}{d\Lambda} \quad (4.19b)$$

does not contain  $\delta\Sigma^\Lambda$ . The second term in Eq. (4.19a) can be derived by substituting Eq. (4.18) into Eq. (4.14) and has the form

$$\delta S^\Lambda = \sum_{l>0} a_l [\delta\Sigma^\Lambda]^l, \quad (4.19c)$$

where the coefficients  $a_l$  depend on  $G_{\text{dmft}}$  but not on  $\delta\Sigma^\Lambda$ .

The tadpole (4.15) can now be rewritten as

$$\mathcal{T}^{V_6} = -S_{\text{dmft}}^\Lambda \circ V_{\text{dmft}}^{(6)} - \delta S^\Lambda \circ V_{\text{dmft}}^{(6)} - S_{\text{dmft}}^\Lambda \circ \delta V^{(6)\Lambda} - \delta S^\Lambda \circ \delta V^{(6)\Lambda}. \quad (4.20)$$

The first term does not contribute to the final solution of the vertex  $V^{\Lambda_{\text{fin}}}$ . In fact, since  $V_{\text{dmft}}^{(6)}$  is a local function and by using Eq. (4.19b) we have

$$\int_{\Lambda_{\text{ini}}}^{\Lambda_{\text{fin}}} d\Lambda S_{\text{dmft}}^\Lambda \circ V_{\text{dmft}}^{(6)} = T \sum_{\nu} V_{\text{dmft}}^{(6)} \int_{\mathbf{k}} [G_{\text{dmft}}^{\Lambda_{\text{fin}}} - G_{\text{dmft}}^{\Lambda_{\text{ini}}}] = 0. \quad (4.21)$$

Here we used  $G_{\text{dmft}}^{\Lambda_{\text{ini}}} = [\mathcal{G}_0^{-1} - \Sigma_{\text{dmft}}]^{-1}$ ,  $G_{\text{dmft}}^{\Lambda_{\text{fin}}} = [G_0^{-1} - \Sigma_{\text{dmft}}]^{-1}$  and the DMFT self-consistency condition (1.43). We note that relation (4.21) is valid for any flow scheme  $G_0^\Lambda$  fulfilling condition (1.54). This term represents local contributions that are already included at the DMFT level and, in the case of DMFT conserving scheme (4.12), is zero at every step during the flow. The other terms in Eq. (4.20) contribute only after nonlocal correlations are generated. At the initial state of the flow,  $\delta\Sigma^\Lambda$  and  $\delta V^{(6)\Lambda}$  are zero and, hence, the three-particle tadpole  $\mathcal{T}^{V_6}$  vanishes.

### 4.3 Single-channel approximation

In the conventional fRG, when restricting the flow of the two-particle vertex to a single channel, particle-particle or direct/crossed particle-hole, and when neglecting the self-energy feedback, the solution of the flow equation is equivalent to a random phase approximation (RPA) in that particular channel [20]. A similar statement holds for the DMF<sup>2</sup>RG: neglecting the self-energy flow, the single-channel DMF<sup>2</sup>RG is equivalent to a RPA with the irreducible DMFT vertex instead of the bare interaction. The latter is required for the calculation of response functions within DMFT [42]. We now demonstrate this equivalence explicitly for the case of the crossed particle-hole channel.

Within DMFT, the momentum dependent vertex function for the calculation of magnetic response functions is obtained from the Bethe-Salpeter equation in the crossed particle-hole channel as [42, 54]

$$V_{\mathbf{q},\omega}^{\text{rpa}}(\nu_1, \nu_3) = \sum_{\nu} V_{\text{dmft},\omega}(\nu_1, \nu) A_{\mathbf{q},\omega}^{-1}(\nu, \nu_3), \quad (4.22)$$

with  $V_{\text{dmft},\omega}(\nu_1, \nu_3) = V_{\text{dmft}}(\nu_1, \omega + \nu_3, \nu_3)$ , and

$$A_{\mathbf{q},\omega}(\nu_1, \nu_3) = \delta_{\nu_1, \nu_3} - T[\chi_{\mathbf{q},\omega}^0(\nu_1) - \chi_{\text{loc},\omega}^0(\nu_1)]V_{\text{dmft},\omega}(\nu_1, \nu_3). \quad (4.23)$$

$A_{\mathbf{Q},\Omega}^{-1}(\nu_1, \nu_3)$  is the matrix inverse of  $A_{\mathbf{Q},\Omega}(\nu_1, \nu_3)$  viewed as matrix with the fermionic Matsubara frequencies  $\nu_1$  and  $\nu_3$  as matrix indices. We also introduced the momentum integrated particle-hole propagator

$$\chi_{\mathbf{q},\omega}^0(\nu) = - \int_{\mathbf{k}} G_{\text{dmft}}(\mathbf{k}, \nu) G_{\text{dmft}}(\mathbf{q} + \mathbf{k}, \omega + \nu), \quad (4.24)$$

with  $G_{\text{dmft}}^{-1}(\mathbf{k}, \nu) = i\nu + \mu - \epsilon_{\mathbf{k}} - \Sigma_{\text{dmft}}(\nu)$ , and the local particle-hole propagator  $\chi_{\text{loc},\Omega}^0(\nu) = -G_{\text{loc}}(\nu)G_{\text{loc}}(\Omega + \nu)$  with  $G_{\text{loc}}(\nu) = \int_{\mathbf{k}} G_{\text{dmft}}(\mathbf{k}, \nu)$ .

To prove the equivalence between DMFT-RPA and single channel DMF<sup>2</sup>RG, we show that Eq. (4.22) is the solution of the vertex flow equation, once we neglect the flow of the self-energy and take only the crossed particle-hole channel into account. To this end, we introduce the  $\Lambda$  dependent particle-hole propagator  $\chi_{\mathbf{Q},\Omega}^{0,\Lambda}(\nu)$  by promoting  $G_{\text{dmft}}$  in Eq. (4.24) to the  $\Lambda$  dependent propagator  $G_{\text{dmft}}^{\Lambda} = [G_0^{\Lambda-1} - \Sigma_{\text{dmft}}]^{-1}$ , where  $G_0^{\Lambda}$  can be

any continuous function fulfilling the conditions  $G_0^{\Lambda_{\text{ini}}} = \mathcal{G}_0$  and  $G_0^{\Lambda_{\text{fin}}} = G_{0,\text{latt}}$ . The matrix  $A_{\mathbf{Q},\Omega}$  in Eq. (4.23) becomes  $\Lambda$  dependent through  $\chi_{\mathbf{Q},\Omega}^{\Lambda,0}(\nu)$ , and Eq. (4.22) reads

$$V_{\mathbf{q},\Omega}^{\text{rpa},\Lambda}(\nu_1, \nu_3) = \sum_{\nu} V_{\text{dmft},\Omega}(\nu_1, \nu) (A_{\mathbf{q},\Omega}^{\Lambda})^{-1}(\nu, \nu_3). \quad (4.25)$$

Defining the function  $\phi^{\text{rpa},\Lambda} = V^{\text{rpa},\Lambda} - V_{\text{dmft}}$  and taking the  $\Lambda$  derivative of Eq. (4.25) yields

$$\begin{aligned} \frac{d\phi_{\mathbf{q},\Omega}^{\text{rpa},\Lambda}}{d\Lambda} &= T \sum_{\nu} [V_{\text{dmft},\Omega}(\nu_1, \nu) + \phi_{\mathbf{q},\Omega}^{\text{rpa},\Lambda}(\nu_1, \nu)] \\ &\times \frac{d\chi_{\mathbf{q},\Omega}^{\Lambda,0}(\nu)}{d\Lambda} [V_{\text{dmft},\Omega}(\nu, \nu_3) + \phi_{\mathbf{q},\Omega}^{\text{rpa},\Lambda}(\nu, \nu_3)]. \end{aligned} \quad (4.26)$$

Eq. (4.26) is equivalent to Eq. (4.8) with  $\mathcal{M}^{\Lambda} = \phi^{\text{rpa},\Lambda}$ , once the feedback of the self-energy is neglected and only the first line of Eq. (4.10) is taken into account. Hence, the solution of the single-channel approximation of the DMF<sup>2</sup>RG is equivalent to the RPA with the DMFT vertex in that given channel. We have selected the particle-hole crossed channel as a concrete example. A similar equivalence between single-channel DMF<sup>2</sup>RG and RPA also holds for the particle-particle and the direct particle-hole channels.

## 4.4 Flow at strong coupling: the role of the frequency dependence

We will now discuss our results obtained by means of DMF<sup>2</sup>RG in its full frequency dependent implementation. In the first part of this section we test the method at half-filling for both weak and strong interactions. We will show that the DMF<sup>2</sup>RG is able to access the strong coupling regime, once the vertex frequency dependence is properly taken into account. The second part of the section is dedicated to the more interesting parameter regime away from half-filling, relevant for high temperature superconductivity in cuprates. We will focus on the interplay between the two key players in this regime, strong magnetic fluctuations and emerging  $d$ -wave pairing fluctuations. Numerical details are described in Appendix B.

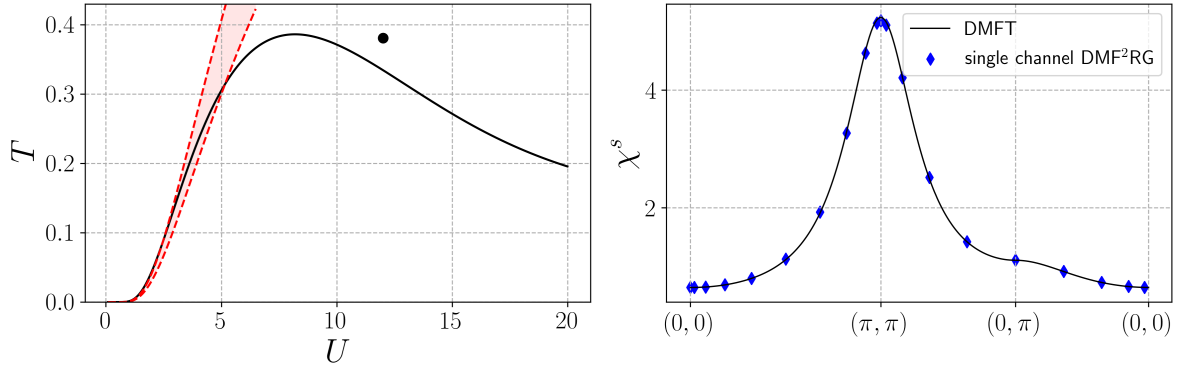


Figure 4.3: Left panel: DMFT Néel temperature as a function of  $U$  (black line) for  $n = 1$  and  $t' = 0$ . The shadowed area depicts the range of transition temperatures obtained from a simplified parametrization of the vertex with a single bosonic frequency variable in each channel. Right panel: Spin susceptibility  $\chi^s$  along a path in the BZ zone as computed from RPA with DMFT vertex and self-energy (black solid line), and by the single-channel DMF<sup>2</sup>RG (blue symbols). Here  $U = 12t$  and  $T = 0.038t$ , corresponding to the black dot in the left panel.

The spin susceptibility  $\chi_q^s$  with  $q = (\mathbf{q}, \Omega)$  is obtained from the two-particle vertex as

$$\chi_q^s = \int_k \chi_q^0(k) + \int_{k,k'} \chi_q^0(k) V(k, k' + q, k') \chi_q^0(k'), \quad (4.27)$$

where  $\chi_q^0(k) = -G(k)G(k+q)$ . We set  $t = 1$  in all plots of quantities with dimension energy.

In this section we focus on the special case of pure nearest neighbor hopping ( $t' = 0$ ) at half-filling ( $n = 1$ ), where particle-hole symmetry leads to several simplifications. Due to perfect nesting, the physics is dominated by magnetic fluctuations peaked at  $(\pi, \pi)$  for any coupling strength  $U$ . We will present results for the magnetic properties of the half-filled 2D Hubbard model, and show that taking the full frequency dependence of the vertex into account is crucial at strong coupling.

In the left panel of Fig. 4.3, we show the  $U$ -dependence of the Néel temperature as obtained from the DMFT. The smooth curve is a fit to data points obtained previously by Kunes [104], which are consistent with our own calculations. We have checked numerically that the Néel temperature predicted by the single-channel DMF<sup>2</sup>RG described in Sec. 4.3 indeed agrees with the Néel temperature computed from the RPA suscep-

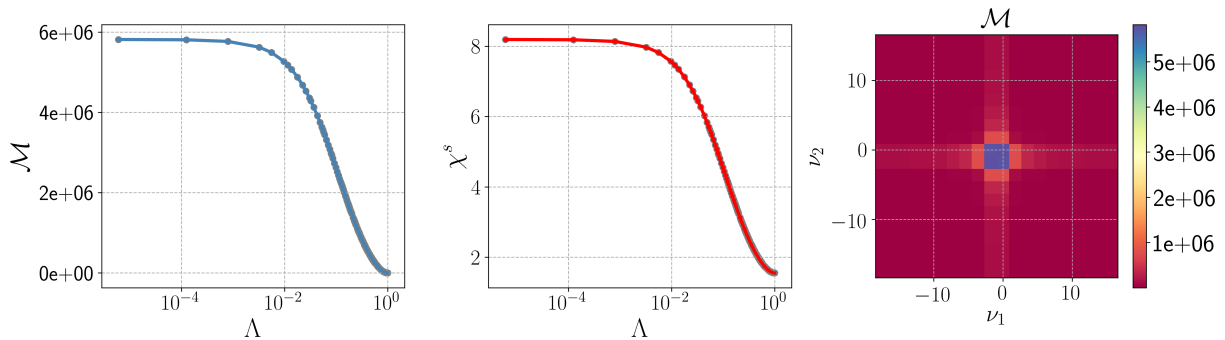


Figure 4.4: Left panel: Flow of the maximum of the magnetic fluctuation term as function of the flow parameter  $\Lambda$ . Center panel: Flow of the magnetic susceptibility at  $\mathbf{Q} = (\pi, \pi)$  and  $\Omega = 0$ . Right panel: Frequency dependence of the magnetic fluctuation term for momentum  $\mathbf{Q} = (\pi, \pi)$  and vanishing bosonic frequency  $\Omega = 0$ . Parameters:  $U = 16t$ ,  $T = 0.29t$ ,  $t' = 0$  and  $n = 1$ .

tibility with the local DMFT vertex. The red shadowed area, instead, shows the Néel temperature as obtained from the single-channel DMF<sup>2</sup>RG with an approximate ansatz for the frequency dependence, where only the bosonic frequency dependence of the magnetic fluctuation term  $\mathcal{M}^\Lambda$  is taken into account, while the two fermionic frequencies are projected to some arbitrary value [53, 65]. Different choices for the projection lead to different estimates for the transition temperature – hence the shadowed area instead of a single transition line. As the interaction is increased the difference between the upper and the lower transition temperatures increases, reflecting the fact that the quality of the single-frequency approximation deteriorates. As a matter of fact, the error is sizable already for intermediate coupling. Eventually, the approximation fails to reproduce the maximum of the Néel temperature as a function of  $U$  and its decrease at large  $U$ .

On the other hand, we have verified numerically that the single-channel DMF<sup>2</sup>RG with full frequency dependence reproduces exactly the DMFT results, where the susceptibility is computed from a RPA (ladder sum) with the DMFT vertex. While this agreement is dictated by the analytic proof in Sec. 4.3, it is still challenging to reproduce in a numerical evaluation. To demonstrate the accuracy of the agreement, and thus the performance of our code, we plot the susceptibility along a specific momentum path in the Brillouin zone computed with both methods (right panel of Fig. 4.3), for a parameter set at strong coupling where the single-frequency approximation fails drastically.

The decrease of the Néel temperature at large  $U$  is known to be associated with a

change in the mechanism leading to an antiferromagnetic ground state, from Slater-type to Heisenberg-type [105, 106, 107]. The failure of the single-frequency approximation in the intermediate to strong coupling regions reveals that the vertex acquires a frequency structure that cannot be reproduced by a single bosonic frequency only.

We now turn to the first complete DMF<sup>2</sup>RG calculation at strong coupling. Here the flow of the vertex is computed with all the channels taken into account. In the particle-hole symmetric case, the DMF<sup>2</sup>RG always exhibits an antiferromagnetic instability toward a Néel state at low temperature. In Fig. 4.4 we show, from left to right, the flow of the maximum of the magnetic fluctuation channel, the flow of the maximum of the magnetic susceptibility, and the magnetic fluctuation strength for  $\mathbf{Q} = (\pi, \pi)$  and  $\Omega = 0$  at the end of the flow, as a function of the fermion frequencies. The coupling strength is  $U = 16t$ , and the temperature  $T = 0.29t$  slightly above the Néel temperature. We see that DMF<sup>2</sup>RG is able to recover convergent results at strong coupling, where the conventional fRG is clearly inapplicable. Note that the vertex maximum at strong coupling can be thousands or even millions of times larger than the hopping, as can be seen from the left panel of Fig.4.4. However, the maximum is very sharp in frequency space – see the right panel of Fig. 4.4. This, together with the self-energy, leads to relatively moderate values of the magnetic susceptibility shown in the central panel of Fig. 4.4.

In weak coupling fRG calculations [20] the flow is usually stopped when the largest vertex component exceeds a certain value  $V_{\max}$  of the order of ten or hundred times the hopping, since this is typically a precursor of a divergence, accompanied by a divergence of a susceptibility, and the weak coupling truncation is at least questionable at this point. At strong coupling, we see that the magnetic fluctuation contribution to the two-particle vertex can be huge in a small frequency regime, while the magnetic susceptibility is only moderately enhanced, and the flow remains stable. At weak coupling, the dependence of the vertex on the fermion frequencies is much more shallow [65].

The instability criterion in conventional fRG, suggested by weak coupling arguments [61] and based on the size of the two-particle vertex, is thus misleading at strong coupling. In fact, at strong coupling already the DMFT vertex can be very large for certain frequencies, while the susceptibility, which contains a summation over the fermionic frequencies of the vertex, can still be moderate. Hence, rather than looking at the maximal value of the vertex, the instability criterion should be defined by the maximum of the corresponding susceptibility.

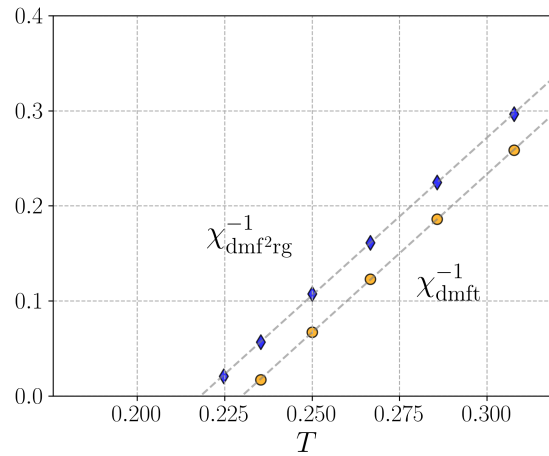


Figure 4.5: Inverse of the static magnetic susceptibility for  $\mathbf{Q} = (\pi, \pi)$  as a function of the temperature for  $U = 4t$  in DMF<sup>2</sup>RG and in RPA with DMFT vertices for  $n = 1$  and  $t' = 0$ .

In Fig. 4.5 we plot the inverse of the magnetic susceptibility for  $\Omega = 0$  and  $\mathbf{Q} = (\pi, \pi)$ , at an intermediate coupling as a function of the temperature. An extrapolation of  $(\chi^s)^{-1}$  indicates a finite Néel temperature. For a comparison we also show the same quantity as computed by the RPA with DMFT vertices. One can see that the Néel temperature in DMF<sup>2</sup>RG is only slightly reduced compared to the DMFT results, which, in turn, is much smaller than the temperature predicted by the standard RPA. In conventional fRG, fluctuations in the non-magnetic channels (mostly pairing) substantially reduce the Néel temperature. On the local level, these effects are already taken into account by the DMFT, while a further reduction of the Néel temperature due to nonlocal fluctuations in the non-magnetic channels turns out to be less pronounced.

At half filling and with  $t' = 0$ , a divergent spin susceptibility signaling a magnetic instability at low temperature is found in our calculations for any coupling strength. However, an ordered magnetic state breaking the  $SU(2)$  spin symmetry is excluded at finite temperature in two dimensions by the Mermin-Wagner theorem [39]. The truncation of nonlocal fluctuation contributions underlying our present implementation of the DMF<sup>2</sup>RG misses the order parameter fluctuations preventing the magnetic order at finite temperatures. This deficiency could be cured by including thermal order parameter fluctuations using the techniques developed by Baier et al. [37] for the plain fRG.

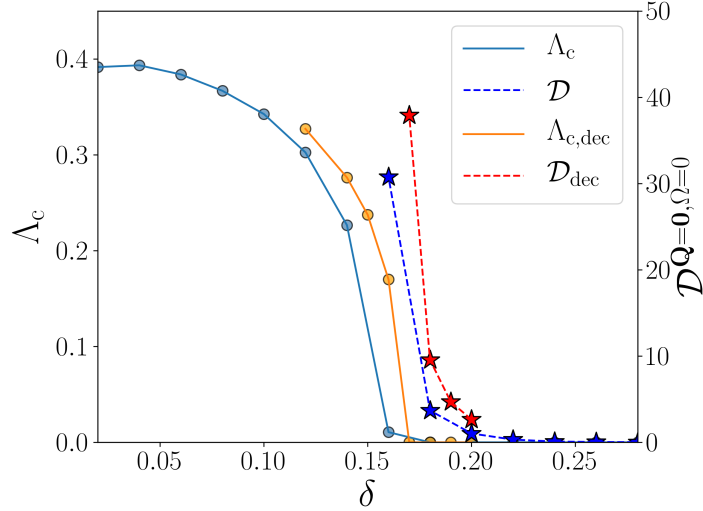


Figure 4.6: Left axis: Critical flow parameter  $\Lambda_c$  for the antiferromagnetic instability as a function of doping  $\delta = 1-n$  in full DMF<sup>2</sup>RG (blue circles) and in single-channel DMF<sup>2</sup>RG (orange circles), respectively. Right axis: Maximum of the  $d$ -wave pairing interaction  $\mathcal{D}$  from the full DMF<sup>2</sup>RG (blue stars) and in a decoupling approximation (red stars), respectively. The lines connecting the symbols are guides to the eye. Parameters are:  $U = 8t$ ,  $T = 0.08t$  and  $t' = -0.2t$ .

## 4.5 Nonlocal correlations at finite dopings

Let us now switch to the finite doping case in a parameter range relevant for cuprates. The ratio of next-to-nearest neighbor hopping and nearest neighbor hopping is  $t'/t = -0.2$  in the entire section. We keep the filling fixed during the flow by properly adjusting an additive constant in the real part of the self-energy.

### Magnetic fluctuations

In Fig. 4.6 we show the critical flow parameter  $\Lambda_c$  as a function of doping for  $U = 8t$  and  $T = 0.08t$ . Assuming a hopping value for cuprates of  $t \approx 0.4\text{eV}$ , the chosen temperature is thus about 350K. We observe a magnetic instability for all dopings smaller than  $\delta_c = 0.18$ . For higher doping values the flow reaches  $\Lambda = 0$  without encountering any instability. Decreasing the temperature to  $T = 0.044t$ , we only observe a very slight increase of the critical doping value. Hence, from our results, we see that the critical doping for a magnetic instability  $\delta_c$  remains about 0.18 down to the lowest temperatures.

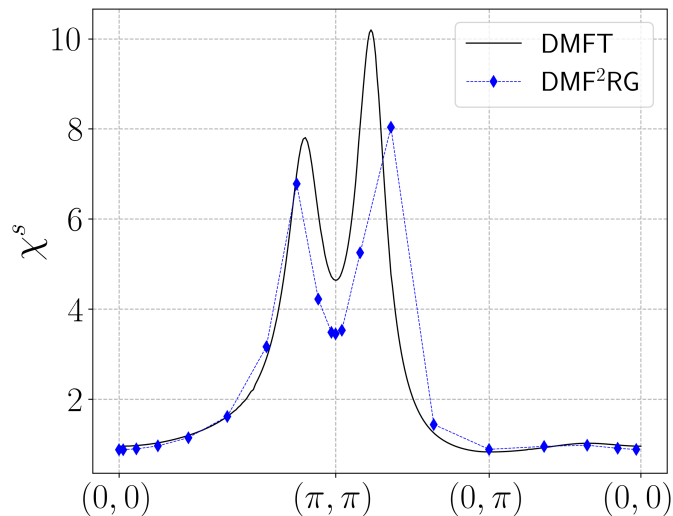


Figure 4.7: Static magnetic susceptibility in DMFT-RPA (black line) and in full DMF<sup>2</sup>RG (blue points) along a specific path in the BZ. Parameters:  $U = 8t$ ,  $T = 0.08t$ ,  $t' = -0.2t$  and  $\delta = 0.18$ .

This value is roughly comparable to the maximal doping range for which the pseudogap is experimentally observed, albeit at lower temperatures for  $\delta$  beyond the underdoped regime [108]. Hence, the large magnetic fluctuations leading to the instability of the flow should not be associated with spontaneous symmetry breaking, but rather with the onset of the pseudogap. The instability occurs at the commensurate antiferromagnetic wave vector  $(\pi, \pi)$  for  $\delta < 0.16$ , and at incommensurate wave vectors of the form  $(\pi - 2\pi\eta, \pi)$  with  $\eta > 0$  for larger values of the doping.

In Fig. 4.7 we compare the magnetic susceptibility of DMF<sup>2</sup>RG with the one from RPA with DMFT vertex for doping  $\delta = 0.18$  along a specific path in the BZ. The two susceptibilities are qualitatively similar, showing that the inclusion of the other channels leads only to minor quantitative modifications in this parameter regime. In particular we observe that in both cases  $(\pi, \pi)$  is a marked local minimum. The maximum of the susceptibility in DMF<sup>2</sup>RG seems to be shifted to a slightly different incommensurate wave vector compared to the DMFT-RPA, but the limited momentum resolution of the DMF<sup>2</sup>RG calculation does not allow for a conclusive statement.

To highlight the different frequency structures that arise in different coupling regimes, we show in Fig. 4.8 the frequency dependence of  $\mathcal{M}^\Lambda$  for  $\Omega = 0$  and  $\mathbf{Q} = (\pi, \pi)$  at weak

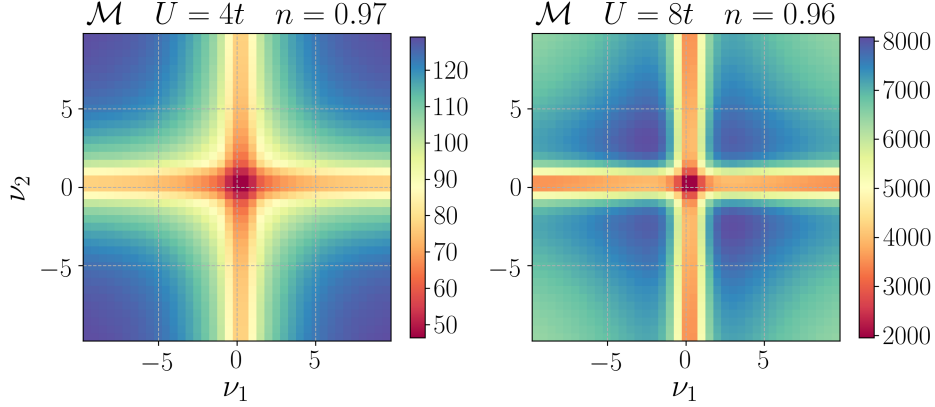


Figure 4.8: Frequency dependence of the magnetic fluctuation channel at weak (left) and strong (right) coupling close to half-filling for  $T = 0.08t$  and  $t' = -0.2t$ .

and strong coupling, with  $\Lambda$  slightly below the critical value  $\Lambda_c$ . At weak coupling the maximal value of  $\mathcal{M}^\Lambda$  is observed for asymptotically large values of  $\nu_1$  and  $\nu_2$  in the frequency region where the channel competition is less effective. The cross shaped structure, that can be ascribed to the effect of the feedback from the other channels [31], on the other hand, decreases the value of  $\mathcal{M}^\Lambda$ . At strong coupling, the cross shaped structure is still decreasing  $\mathcal{M}^\Lambda$ , but the maximal values are not in the asymptotic region, but in a localized area for limited values of  $\nu_1$  and  $\nu_2$  (and away from the cross shaped structure). Although a complete explanation of these features in Matsubara frequency space is still missing, they hint at a different nature of the magnetic fluctuations at weak and at strong coupling.

### ***d*-wave pairing fluctuations**

As discussed above, the pairing and density channels do not strongly affect the magnetic one. However the reverse is not true: the magnetic channel generates *d*-wave pairing fluctuations which, for lower temperatures, are supposed to give rise to a pairing instability.

In Fig. 4.6 (see stars and right axis) we show the maximal value of  $\mathcal{D}^\Lambda$  for the lowest accessible value of  $\Lambda$ , which measures the strength of the *d*-wave pairing interaction. For dopings much larger than  $\delta_c$  the pairing interaction is very small. Decreasing the doping

from 0.2 to 0.16 the  $d$ -wave pairing interaction rapidly increases. Decreasing the doping further, the flow runs into the magnetic instability and has to be stopped at the critical flow parameter  $\Lambda_c$ . The  $d$ -wave interaction at the critical scale  $\Lambda_c$  then drops again, to very small values.

These results can be interpreted as follows. For  $\delta \gtrsim \delta_c$  the magnetic fluctuations become strong and the large magnetic channel drives the  $d$ -wave interaction to large values. When the doping is decreased further, the flow has to be stopped before the  $d$ -wave interaction can fully develop. In the context of the conventional fRG it has been frequently observed [25, 35] that the  $d$ -wave pairing increases quite rapidly at a late stage of the flow, as compared to the more gradual increase of the magnetic channel, which sets in already at high energy scales. While the flow parameter in DMF<sup>2</sup>RG is a measure of nonlocality rather than an energy scale, the retarded but then rapid formation of pairing interactions seems to be typical here, too.

To confirm the magnetic pairing mechanism, in Fig. 4.6 we also present the critical value  $\Lambda_c$  and the pairing interaction  $\mathcal{D}^\Lambda$  within a simplified approximation, where we neglect the flow of the self-energy and set  $\mathcal{C}^\Lambda = \mathcal{S}^\Lambda = 0$ , while the magnetic channel is treated at the single-channel level as in Sec. 4.3. As a consequence, the  $d$ -wave pairing channel receives contributions only from the magnetic channel and the pairing channel itself. In this approach the feedback of charge and  $s$ -wave pairing channels is taken into account only at the DMFT level. The  $\mathcal{D}$  channel does not receive any contribution from the DMFT vertex, since the latter is local. The resulting critical flow parameter  $\Lambda_c$ , shown in orange in Fig. 4.6, is always slightly larger than the one from the full DMF<sup>2</sup>RG. This confirms that the channel competition has only a modest detrimental effect on the magnetic fluctuations. The maximal doping value for which the magnetic instability is observed increases. A sizable  $d$ -wave pairing interaction sets in for higher values of the doping, too. There is no major difference in the  $d$ -wave pairing interaction compared to the full DMF<sup>2</sup>RG where all the channels are included, supporting the hypothesis that  $d$ -wave pairing is mostly driven by the nonlocal magnetic channel.

In Fig. 4.9 we show the inverse  $d$ -wave pairing interaction  $\mathcal{D}^{-1}$  for  $\mathbf{Q} = (0, 0)$  and  $\Omega = 0$ , as a function of the flow parameter  $\Lambda$  for different fillings. The parameters are the same as in Fig. 4.6. For  $n = 0.88$  and  $n = 0.96$ , the flow is shown up to the critical value  $\Lambda_c$  at which the magnetic instability occurs. Approaching half-filling  $n = 1$ , the  $d$ -wave pairing correlations increase but cannot develop further due to the magnetic instability

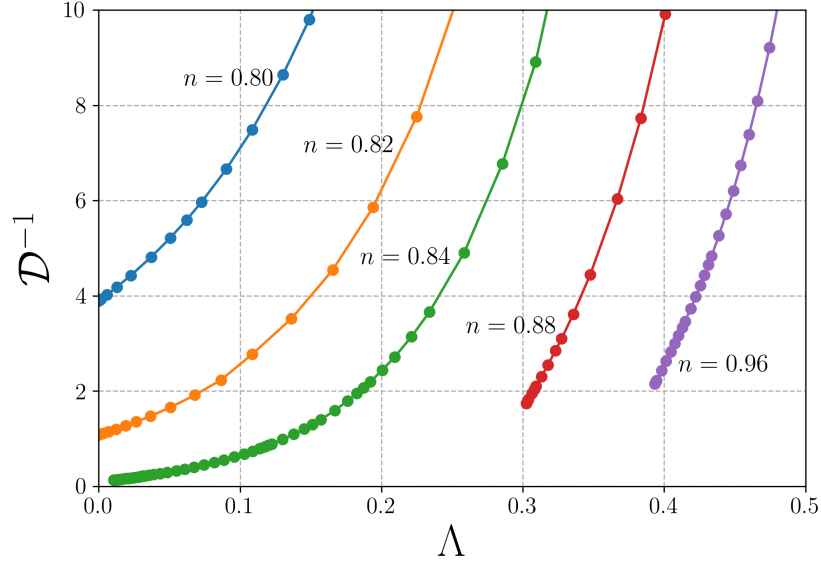


Figure 4.9: Inverse  $d$ -wave channel as a function of flow parameter  $\Lambda$  for various fillings. Parameters:  $U = 8t$ ,  $T = 0.08t$  and  $t' = -0.2$ .

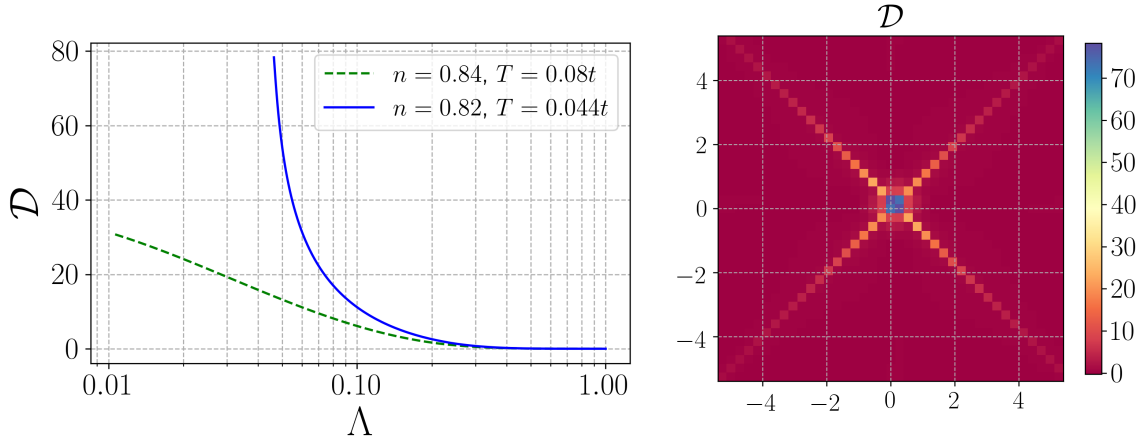


Figure 4.10: Left panel: flow of the  $d$ -wave pairing channel at higher and lower temperature for  $U = 8t$  and  $t' = -0.2$ . Right panel: plot of the  $d$ -wave pairing channel as a function of the Matsubara frequencies  $\nu_1$  and  $\nu_2$  for  $U = 8t$ ,  $t' = -0.2t$ ,  $T = 0.044t$  and  $n = 0.82$ .

which prevents a continuation of the flow to smaller  $\Lambda$ .

Finally, let us discuss the role of the temperature. The results discussed so far are for a temperature  $T = 0.08t$ , roughly comparable with room temperature and thus much higher than the maximal temperatures for which  $d$ -wave superconductivity has been observed. Therefore, we do not expect a  $d$ -wave pairing instability at this temperature, but the onset of a large  $d$ -wave pairing interaction is likely a high-temperature precursor of a superconducting phase at lower temperature.

Different theoretical studies yield different estimates for the maximal temperature for which superconductivity is observed for the Hubbard model on the square lattice. For example, while cluster extensions of the DMFT [47, 109] find a higher scale of  $T \approx 0.03t$ , more diagrammatic methods [51, 52] observed superconductivity only for temperatures below  $T \approx 0.01t$ . Experimentally, the maximal superconducting temperature observed for cuprates is  $\mathcal{O}(100)\text{K}$ , which roughly corresponds to  $T \sim 0.02t$  in units of the nearest-neighbor hopping amplitude. Hence, we expect that we need to decrease the temperature by a factor of three or four compared to what we have achieved so far.

Due to the high computational cost of low- $T$  calculations, we cannot reach the superconducting transition temperature at the moment. However, to better understand the evolution of the  $d$ -wave fluctuations at lower temperatures, we have performed few computations at a reduced (compared to the above) temperature  $T = 0.044t$ . In the left panel of the Fig. 4.10, the flow of the maximum of the  $d$ -wave pairing channel  $\mathcal{D}$  has been shown for the doping value where the  $d$ -wave pairing is most pronounced. In the same figure, we plot also the flow of  $\mathcal{D}$  for  $T = 0.08t$  and  $n = 0.84$ . Our expectation is that, as the temperature is further decreased, the relative relevance of the  $d$ -wave pairing should increase and its flow become more steep, until, eventually the  $d$ -wave pairing becomes larger than the magnetic one. This is indicated by the comparison in Fig. 4.10, where the pairing interaction at the lower temperature is not only much larger, but also has a larger slope. In both cases the critical value  $\Lambda_c$  is set by the instability in the magnetic channel, but the  $d$ -wave pairing interaction is much larger for the lower temperature.

All these observations lead us to the conclusion that also in the strong-coupling regime the magnetic fluctuations can generate large  $d$ -wave pairing interactions leading ultimately a pairing instability at sufficiently low temperatures.

In the right panel of the Fig. 4.10, we show the dependence of the  $\mathcal{D}$  channel on the Matsubara frequencies  $\nu_1, \nu_3$  for  $\Omega = 0$  and  $\mathbf{Q} = (0, 0)$ . The frequency structures are

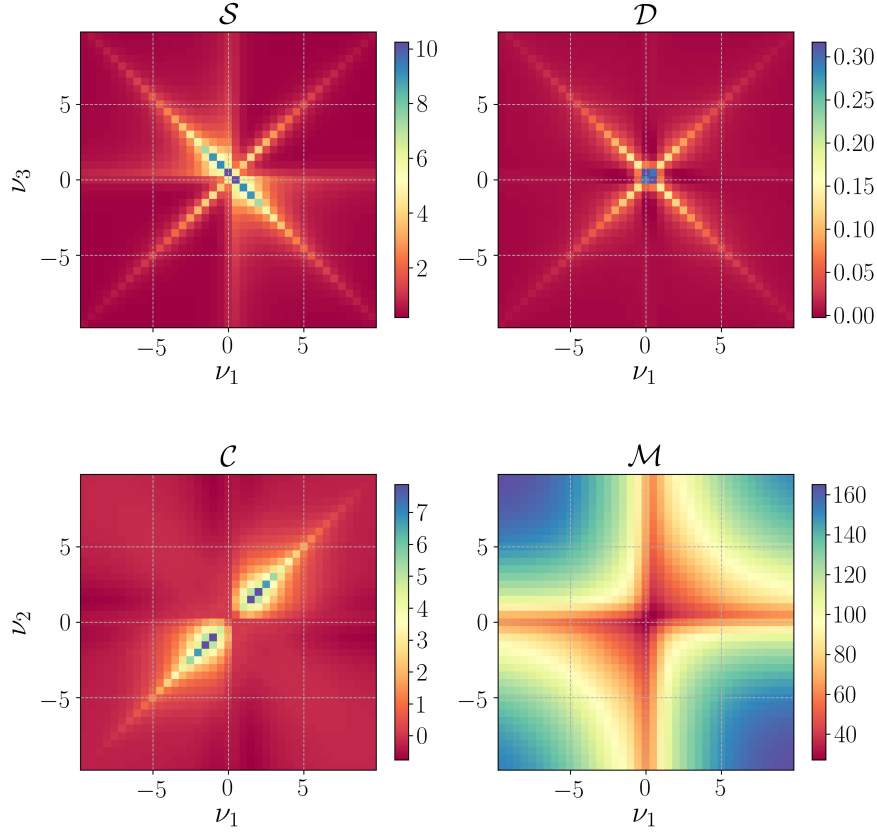


Figure 4.11: Frequency dependence of the interacting channels. Top row:  $s$ -wave and  $d$ -wave pairing channels. Bottom row: charge and magnetic channels.  $\mathcal{S}$ ,  $\mathcal{D}$  and  $\mathcal{C}$  are shown for  $\Omega = 0$  and  $\mathbf{Q} = (0, 0)$  while  $\mathcal{M}$  for  $\Omega = 0$  and  $\mathbf{Q} = (\pi, \pi - 2\pi\eta)$  with  $\eta \approx 0.18$ . Parameters are:  $U = 8t$ ,  $\delta = 0.22$ ,  $T = 0.08t$  and  $t' = -0.2t$ .

very similar to those observed in the conventional fRG calculation shown in Chapter 2, see Fig. 2.7. The leading frequency dependence of the  $d$ -wave pairing channel is localized around the lowest Matsubara frequencies  $\nu_1 = \pm\pi T$  and  $\nu_3 = \pm\pi T$ .

### Frequency dependence of the nonlocal interacting channels

In Fig. 4.11 we show the channels  $\mathcal{S}$ ,  $\mathcal{D}$ ,  $\mathcal{C}$  and  $\mathcal{M}$  as a function of the fermionic Matsubara frequencies for  $\Omega = 0$ . All the channels have important frequency structures that cannot be represented by single-frequency functions. These plots confirm the necessity of the full frequency parametrization at strong coupling also for the non-magnetic channels.

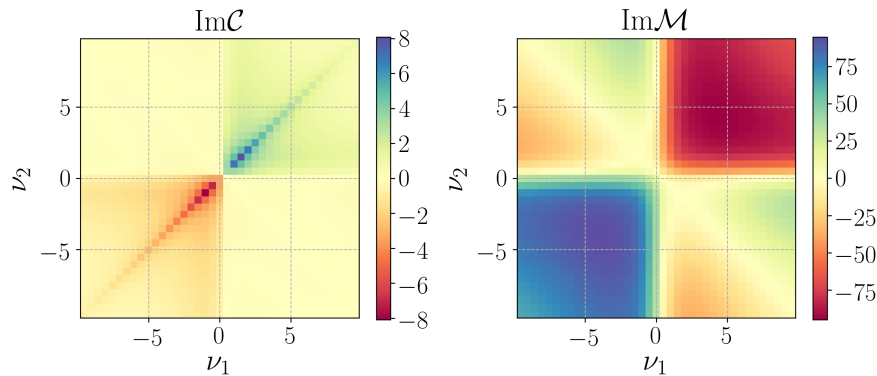


Figure 4.12: Frequency dependence of the imaginary part of the charge and magnetic channels, for transfer frequency  $\Omega = 0$  and momentum  $\mathbf{Q} = (0, 0)$  and  $\mathbf{Q} = (\pi, \pi - 2\pi\eta)$  with  $\eta \approx 0.18$ , respectively. Parameters are:  $U = 8t$ ,  $\delta = 0.22$ ,  $T = 0.08t$  and  $t' = -0.2t$ .

In Fig. 4.12 the imaginary parts of the charge and magnetic channels have been shown. They both clearly respects the symmetry properties reported in Ref. [31], for instance,  $\mathcal{M}_{\mathbf{Q},\Omega}^*(\nu_1, \nu_2) = \mathcal{M}_{\mathbf{Q},\Omega}(-\nu_2, -\nu_1)$  for  $\Omega = 0$  and  $\mathbf{Q} = (\pi, \pi - 2\pi\eta)$  with  $\eta \approx 0.18$ .

### Self-energy

In Fig. 4.13 we show the imaginary part of the self-energy in Matsubara space for different points in the BZ, and for  $\delta = 0.18$ . For this doping value, the flow reaches the final  $\Lambda$  without encountering any instability, but the magnetic fluctuations are already strongly enhanced. Therefore one could have expected some signature of a strong momentum differentiation in the self-energy, associated to a suppression of the spectral weight in the antinodal region. This is not observed in our calculation. The self-energy does not deviate qualitatively from the DMFT result. This result is very similar to the one we obtained at weak coupling within a conventional fRG scheme with full-frequency dependence [65].

In previous weak coupling fRG calculations [57, 90], the self-energy as a function of real frequencies showed evidence for pseudogap features at the antiferromagnetic hot spots. In particular, the imaginary part of the self-energy exhibited peaks at low frequencies  $|\omega| < \pi T$ . Hence, this feature is not visible in our calculation on the Matsubara axis, where the lowest frequency equals  $\pi T$ .

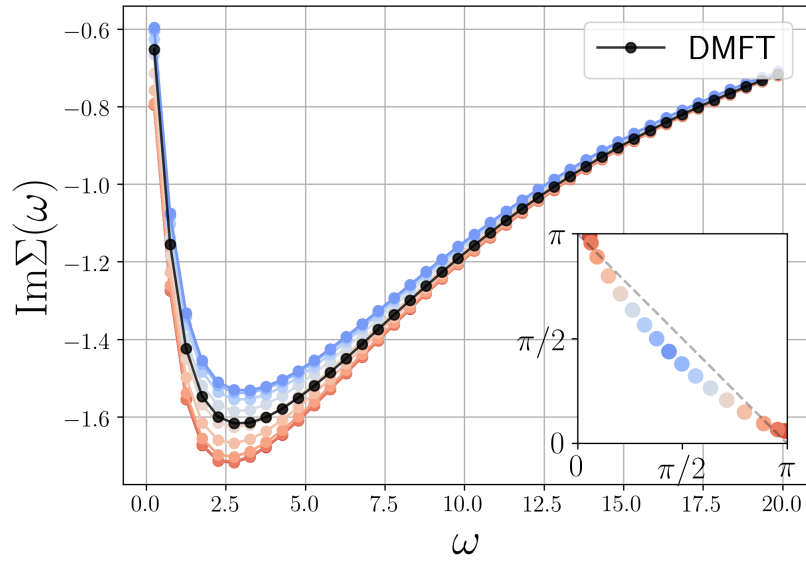


Figure 4.13: Imaginary part of the self-energy as a function of Matsubara frequency for different points in the BZ along the noninteracting Fermi surface (see inset). The local DMFT self-energy is shown in black. Parameters:  $U = 8t$ ,  $T = 0.08t$ ,  $t' = -0.2t$  and  $\delta = 0.18$ .

# Conclusions

Understanding the physics of strongly interacting Fermi systems in two-dimension is a difficult challenge. In this thesis we have dealt with this demanding task by applying to the Hubbard model two of the most successful theoretical methods in this field, the dynamical mean field theory (DMFT), able to capture local correlations nonperturbatively, and the functional renormalization group (fRG), suitable for an unbiased analysis of competing instabilities. We have presented the first application of the fRG flow at strong coupling with the DMFT used as a “booster-rocket”, and have shown that competing instabilities can now be treated also in the strongly interacting regime.

## **Moderate coupling: nontrivial frequency dependence of the vertex**

We first have applied the fRG for moderate coupling strengths. We have shown that a calculation with the full frequency dependences of both the self-energy and the vertex is now feasible. We have used a form factor decomposition for the momentum arguments of the vertex but maintaining intact all the frequency dependence with a high resolution.

The frequency dependence tends to enhance magnetic fluctuations and suppress  $d$ -wave pairing fluctuations. These tendencies are in agreement with previous results obtained from an approximate ansatz for the frequency dependence of the vertex [34]. In a flow without self-energy feedback, there exist regions of parameter space where the vertex shows a peculiar divergence in the charge channel at nonzero frequency, as already found by Husemann *et al.* [34].

We have identified a simple set of Feynman diagrams that qualitatively describe the above-mentioned divergence, which might generate unexpected singular features in the charge channel also in other theories that take into account both the frequency dependence of the vertex and the interplay of different fluctuation channels [86]. We

have revealed the mechanism of this singularity as the combinations of two effects: the feedback of an effective and frequency dependent magnetic interaction on the charge channel and the analytic properties of the particle-hole bubble. This divergence is, however, suppressed by the self-energy feedback, whose frequency dependence can now be properly generated by the frequency dependence of the vertex function. Hence, the feedback of the self-energy into the vertex flow plays an important role also at the qualitative level. The self-energy does not show strong momentum differentiation in the Brillouin zone even close to an antiferromagnetic instability. We performed the instability analysis with different approximation schemes for the vertex and studied their effects on the pairing fluctuations. Given the increasing importance of the frequency dependence as more correlated regimes are approached, the detailed analysis presented in this thesis paves the way for future developments of the fRG for strongly correlated fermion systems.

### **Strong coupling: dynamically enhanced magnetic incommensurability**

At strong coupling, we computed the spin response function and analyzed the impact of local vertex corrections as given by the dynamical mean field theory (DMFT). We showed that the momentum dependence of the spin susceptibility is drastically affected by the local two-particle dynamics. We compared the magnetic properties as captured by the DMFT vertex corrections with a more conventional RPA-like resummation, where the vertex is replaced by the bare interaction.

The vertex correction not only affects the transition temperature, but also the magnetic ordering type. While the RPA susceptibility shows commensurate Néel order as the dominant magnetic instability over a wide density range below half-filling, the DMFT vertex correction predicts incommensurate order with a shifted ordering wave vector. The position of the peaks of the DMFT susceptibility with vertex correction is strikingly close to the peaks determined by the noninteracting Fermi surface geometry. This is remarkable since at strong coupling the self-energy strongly blurs the Fermi surface. Hence, the DMFT self-energy and vertex corrections have opposite impacts on nonlocal magnetic properties with a partial cancellation effects.

Such a dichotomy of the corrections at the single-particle and two-particle levels has been found also in Fermi and Luttinger liquids for the low energy response functions [110] and in theoretical studies of the  $tJ$ -model in 2D [111, 112]. Although low-dimensional

systems are affected by strong nonlocal fluctuations, the local two-particle dynamics is also of crucial importance for the nonlocal spin correlations in a strongly interacting Fermi system.

### Strong coupling: magnetic and superconducting correlations

We finally demonstrated the applicability of the DMF<sup>2</sup>RG to the strongly interacting Hubbard model. This method captures the Mott physics at strong coupling and includes the weaker nonlocal correlations via the fRG flow.

We derived the flow equations in a way that conserves the local contributions already captured by the DMFT. This improvement reduces the errors of the unavoidable truncation of the flow equation hierarchy. An analytic equivalence between a single-channel approximation of the DMF<sup>2</sup>RG and a ladder calculation with DMFT vertices has been established. We showed that an approximation to a single bosonic frequency variable for the fluctuating channel breaks such equivalence from moderate to strong interactions. Hence, the full frequency dependence of the vertex function is essential to access the strong coupling regime and, for instance, recover the correct atomic limit for large couplings. We managed to converge the fRG flow in the Mott regime, where the frequency dependence of the vertex becomes singular due to the formation of local moments.

We then applied the DMF<sup>2</sup>RG to the hole-doped case with finite  $t'$ . From half-filling up to 18 percent doping, strong magnetic fluctuations dominate and lead to an instability for some critical value of the flow parameter  $\Lambda_c$ . The strength and the ordering wave vector of the spin response function are very similar to those predicted by the DMFT; hence, the magnetic correlations are only mildly affected by nonlocal fluctuations in other channels. The antiferromagnetic fluctuations are overestimated due to missing feedback of order parameter fluctuations in the truncated fRG hierarchy. The magnetic instability should rather be associated with the pseudogap formation and not with a signal of the symmetry broken phase.

Strong  $d$ -wave pairing fluctuations emerge close to the onset of magnetic correlations. The lowest temperature calculations showed that the system is not far from a pairing instability, consistent with the temperature range observed in cuprates. We were able to analyze the pairing mechanism by switching off the feedback of non-magnetic contributions. We observed that the pairing mechanism is clearly of magnetic type, as already

observed in the plain fRG at weaker coupling [20].

# Appendices



# Appendix A:

## Vertex and self-energy flow equations

In this appendix we derive the flow equations for the self-energy and the vertex by starting from Eqs. (1.36) and (1.35). Since the derivation is valid for both fRG and DMF<sup>2</sup>RG, we write the decomposition for the vertex as follows

$$\begin{aligned} V^\Lambda(k_1, k_2, k_3) &= V_{\text{ini}}(\nu_1, \nu_2, \nu_3) - \phi_{\text{p}}^\Lambda(k_1 + k_2; k_1, k_3) \\ &+ \frac{1}{2}\phi_{\text{m}}^\Lambda(k_3 - k_1; k_1, k_2) - \frac{1}{2}\phi_{\text{c}}^\Lambda(k_3 - k_1; k_1, k_2) \\ &+ \phi_{\text{m}}^\Lambda(k_2 - k_3; k_1, k_2), \end{aligned} \tag{A.1}$$

where we introduced the function  $V_{\text{ini}}(\nu_1, \nu_2, \nu_3)$  which takes a different value depending on the formalism

$$V_{\text{ini}}(\nu_1, \nu_2, \nu_3) = \begin{cases} U & \text{fRG} \\ V_{\text{dmft}}(\nu_1, \nu_2, \nu_3) & \text{DMF}^2\text{RG} \end{cases}. \tag{A.2}$$

Eq. (A.1) combines decomposition (2.1), used in fRG, and (4.1) in DMF<sup>2</sup>RG. We truncate a form factor expansion in the following form

$$\phi_{\text{p}}^{\Lambda}(Q; k_1, k_3) = \mathcal{S}_{\mathbf{Q}, \Omega}^{\Lambda}(\nu_1, \nu_3) + f_d\left(\frac{\mathbf{Q}}{2} - \mathbf{k}_1\right) f_d\left(\frac{\mathbf{Q}}{2} - \mathbf{k}_3\right) \mathcal{D}_{\mathbf{Q}, \Omega}^{\Lambda}(\nu_1, \nu_3), \quad (\text{A.3a})$$

$$\phi_{\text{c}}^{\Lambda}(Q; k_1, k_2) = \mathcal{C}_{\mathbf{Q}, \Omega}^{\Lambda}(\nu_1, \nu_2), \quad (\text{A.3b})$$

$$\phi_{\text{m}}^{\Lambda}(Q; k_1, k_2) = \mathcal{M}_{\mathbf{Q}, \Omega}^{\Lambda}(\nu_1, \nu_2). \quad (\text{A.3c})$$

Here we used the  $s$ - and  $d$ -wave form factors  $f_s(\mathbf{k}) = 1$  and  $f_d(\mathbf{k}) = \cos(k_x) - \cos(k_y)$ .

The flow equations for the channels  $\mathcal{S}$ ,  $\mathcal{D}$ ,  $\mathcal{C}$  and  $\mathcal{M}$  can be derived from the substitution of Eqs. (A.3) into the decomposition (A.1) and Eq. (1.35a). After a projection onto form factors we have

$$\dot{\mathcal{S}}_{\mathbf{Q}, \Omega}^{\Lambda}(\nu_1, \nu_3) = - \int_{\mathbf{k}_1, \mathbf{k}_3} \mathcal{T}_{\text{pp}}^{\Lambda}(k_1, Q - k_1, k_3), \quad (\text{A.4})$$

$$\dot{\mathcal{D}}_{\mathbf{Q}, \Omega}^{\Lambda}(\nu_1, \nu_3) = - \int_{\mathbf{k}_1, \mathbf{k}_3} f_d\left(\frac{\mathbf{Q}}{2} - \mathbf{k}_1\right) f_d\left(\frac{\mathbf{Q}}{2} - \mathbf{k}_3\right) \mathcal{T}_{\text{pp}}^{\Lambda}(k_1, Q - k_1, k_3), \quad (\text{A.5})$$

$$\dot{\mathcal{C}}_{\mathbf{Q}, \Omega}^{\Lambda}(\nu_1, \nu_2) = \int_{\mathbf{k}_1, \mathbf{k}_2} \mathcal{T}_{\text{phc}}^{\Lambda}(k_1, k_2, k_2 - Q) - 2\mathcal{T}_{\text{ph}}^{\Lambda}(k_1, k_2, Q + k_1), \quad (\text{A.6})$$

$$\dot{\mathcal{M}}_{\mathbf{Q}, \Omega}^{\Lambda}(\nu_1, \nu_2) = \int_{\mathbf{k}_1, \mathbf{k}_2} \mathcal{T}_{\text{phc}}^{\Lambda}(k_1, k_2, k_2 - Q). \quad (\text{A.7})$$

The final equations are then obtained by substituting the expressions for  $\mathcal{T}_x$ , Eqs. (1.35b), (1.35c) and (1.35d), into the equations above, and using trigonometric identities.

The flow equation for the  $s$ -wave pairing channel reads

$$\dot{\mathcal{S}}_{\mathbf{Q}, \Omega}^{\Lambda}(\nu_1, \nu_3) = T \sum_{\nu} L_{\mathbf{Q}, \Omega}^{s, \Lambda}(\nu_1, \nu) P_{\mathbf{Q}, \Omega}^{s, \Lambda}(\nu) L_{\mathbf{Q}, \Omega}^{s, \Lambda}(\nu, \nu_3), \quad (\text{A.8})$$

with

$$P_{\mathbf{Q}, \Omega}^{s, \Lambda}(\nu) = \int_{\mathbf{p}} G^{\Lambda}(\mathbf{p}, \nu) S^{\Lambda}(\mathbf{Q} - \mathbf{p}, \Omega - \nu) + G^{\Lambda}(\mathbf{Q} - \mathbf{p}, \Omega - \nu) S^{\Lambda}(\mathbf{p}, \nu), \quad (\text{A.9})$$

and

$$L_{\mathbf{Q},\Omega}^{s,\Lambda}(\nu_1, \nu_3) = V_{\text{ini}}(\nu_1, \Omega - \nu_1, \nu_3) - \mathcal{S}_{\mathbf{Q},\Omega}^{\Lambda}(\nu_1, \nu_3) + \int_{\mathbf{p}} \left[ \mathcal{M}_{\mathbf{p},\nu_3-\nu_1}^{\Lambda}(\nu_1, \Omega - \nu_1) \right. \\ \left. + \frac{1}{2} \mathcal{M}_{\mathbf{p},\Omega-\nu_1-\nu_3}^{\Lambda}(\nu_1, \Omega - \nu_1) - \frac{1}{2} \mathcal{C}_{\mathbf{p},\Omega-\nu_1-\nu_3}^{\Lambda}(\nu_1, \Omega - \nu_1) \right]. \quad (\text{A.10})$$

The flow equation for the  $d$ -wave pairing channel reads

$$\dot{\mathcal{D}}_{\mathbf{Q},\Omega}^{\Lambda}(\nu_1, \nu_3) = T \sum_{\nu} L_{\mathbf{Q},\Omega}^{\text{d},\Lambda}(\nu_1, \nu) P_{\mathbf{Q},\Omega}^{\text{d},\Lambda}(\nu) L_{\mathbf{Q},\Omega}^{\text{d},\Lambda}(\nu, \nu_3), \quad (\text{A.11})$$

with

$$P_{\mathbf{Q},\Omega}^{\text{d},\Lambda}(\nu) = \int_{\mathbf{p}} [f_{\text{d}}(\mathbf{Q}/2 - \mathbf{p})]^2 [G^{\Lambda}(\mathbf{p}, \nu) S^{\Lambda}(\mathbf{Q} - \mathbf{p}, \Omega - \nu) + G^{\Lambda}(\mathbf{Q} - \mathbf{p}, \Omega - \nu) S^{\Lambda}(\mathbf{p}, \nu)], \quad (\text{A.12})$$

and

$$L_{\mathbf{Q},\Omega}^{\text{d},\Lambda}(\nu_1, \nu_3) = -\mathcal{D}_{\mathbf{Q},\Omega}^{\Lambda}(\nu_1, \nu_3) + \frac{1}{2} \int_{\mathbf{p}} (\cos p_x + \cos p_y) \left[ \mathcal{M}_{\mathbf{p},\nu_3-\nu_1}^{\Lambda}(\nu_1, \Omega - \nu_1) \right. \\ \left. + \frac{1}{2} \mathcal{M}_{\mathbf{p},\Omega-\nu_1-\nu_3}^{\Lambda}(\nu_1, \Omega - \nu_1) - \frac{1}{2} \mathcal{C}_{\mathbf{p},\Omega-\nu_1-\nu_3}^{\Lambda}(\nu_1, \Omega - \nu_1) \right]. \quad (\text{A.13})$$

Note that  $\mathcal{D}$  is generated exclusively by fluctuation contributions (not by the Hubbard interaction  $U$  or the DMFT vertex  $V_{\text{dmft}}$ ).

The flow equation for the charge channel has the form

$$\dot{\mathcal{C}}_{\mathbf{Q},\Omega}^{\Lambda}(\nu_1, \nu_2) = -T \sum_{\nu} L_{\mathbf{Q},\Omega}^{\text{c},\Lambda}(\nu_1, \nu) P_{\mathbf{Q},\Omega}^{\Lambda}(\nu) L_{\mathbf{Q},\Omega}^{\text{c},\Lambda}(\nu, \nu_2 - \Omega), \quad (\text{A.14})$$

with

$$P_{\mathbf{Q},\Omega}^{\Lambda}(\nu) = \int_{\mathbf{p}} G^{\Lambda}(\mathbf{p}, \nu) S^{\Lambda}(\mathbf{Q} + \mathbf{p}, \Omega + \nu) + G^{\Lambda}(\mathbf{Q} + \mathbf{p}, \Omega + \nu) S^{\Lambda}(\mathbf{p}, \nu), \quad (\text{A.15})$$

and

$$\begin{aligned}
L_{\mathbf{Q},\Omega}^{c,\Lambda}(\nu_1, \nu_2) &= 2V_{\text{ini}}(\nu_1, \nu_2, \Omega + \nu_1) - V_{\text{ini}}(\nu_2, \nu_1, \Omega + \nu_1) - \mathcal{C}_{\mathbf{Q},\Omega}^\Lambda(\nu_1, \nu_2) \\
&+ \int_{\mathbf{p}} \left[ -2\mathcal{S}_{\mathbf{p},\nu_1+\nu_2}^\Lambda(\nu_1, \nu_2 - \Omega) + \mathcal{S}_{\mathbf{p},\nu_1+\nu_2}^\Lambda(\nu_1, \Omega + \nu_1) \right. \\
&+ [\cos(Q_x) + \cos(Q_y)] \left( \mathcal{D}_{\mathbf{p},\nu_1+\nu_2}^\Lambda(\nu_1, \nu_2 - \Omega) - \frac{1}{2}\mathcal{D}_{\mathbf{p},\nu_1+\nu_2}^\Lambda(\nu_1, \Omega + \nu_1) \right) \\
&\left. + \frac{3}{2}\mathcal{M}_{\mathbf{p},\nu_2-\nu_1-\Omega}^\Lambda(\nu_1, \nu_2) + \frac{1}{2}\mathcal{C}_{\mathbf{p},\nu_2-\nu_1-\Omega}^\Lambda(\nu_1, \nu_2) \right]. \tag{A.16}
\end{aligned}$$

The flow equation for the magnetic channel is

$$\dot{\mathcal{M}}_{\mathbf{Q},\Omega}^\Lambda(\nu_1, \nu_2) = -T \sum_{\nu} L_{\mathbf{Q},\Omega}^{m,\Lambda}(\nu_1, \nu) P_{\mathbf{Q},\Omega}^\Lambda(\nu) L_{\mathbf{Q},\Omega}^{m,\Lambda}(\nu, \nu_2 - \Omega), \tag{A.17}$$

with  $P_{\mathbf{Q},\Omega}^\Lambda(\nu)$  as in Eq. (A.15), and

$$\begin{aligned}
L_{\mathbf{Q},\Omega}^{m,\Lambda}(\nu_1, \nu_2) &= V_{\text{ini}}(\nu_1, \nu_2, \nu_2 - \Omega) + \mathcal{M}_{\mathbf{Q},\Omega}^\Lambda(\nu_1, \nu_2) \\
&+ \int_{\mathbf{p}} \left\{ -\mathcal{S}_{\mathbf{p},\nu_1+\nu_2}^\Lambda(\nu_1, \nu_1 + \Omega) - \frac{1}{2}\mathcal{D}_{\mathbf{p},\nu_1+\nu_2}^\Lambda(\nu_1, \nu_1 + \Omega)[\cos(Q_x) + \cos(Q_y)] \right. \\
&\left. + \frac{1}{2} \left[ \mathcal{M}_{\mathbf{p},\nu_2-\nu_1-\Omega}^\Lambda(\nu_1, \nu_2) - \mathcal{C}_{\mathbf{p},\nu_2-\nu_1-\Omega}^\Lambda(\nu_1, \nu_2) \right] \right\}. \tag{A.18}
\end{aligned}$$

The form factor decomposition allows to decouple the momentum integrals, in the calculation of the  $L$ 's, Eqs. (A.18), (A.10), (A.13) and (A.16), from the frequency summations in the flow equations, hence reducing the numerical effort.

# Appendix B:

## Numerical setup

In this appendix we discuss the numerical setup we used in the DMFT calculations and in the implementation of the flow equations at finite temperature.

In the DMFT self-consistency loop, we solve the quantum problem associated with the action (1.41) by using the Anderson impurity model (1.44) and the exact diagonalization (ED) [72], see Section 1.2.2. In the DMFT self-consistency procedure, we calculate the local Green's function of the impurity on the Matsubara axis by using the Lehmann representation. The number of bath sites can be 4-10 for the currently available computing power. However, the calculation of the vertex is more expensive than the self-consistency procedure. Hence, we fix the number of bath sites to 4 for the whole calculation, from the DMFT loop to the computation of the vertex function.

As for the Green's function, we compute the impurity vertex from the Lehmann representation. The calculation of the vertex function scales with  $N_\omega^3$ , where  $N_\omega$  is the number of Matsubara frequencies. The calculation for different frequencies is independent from one another. Hence, the openMP and MPI parallelization techniques can be both exploited in this case. Outside the frequency box, the vertex function can be extended by using the asymptotic functions introduced in Ref. [31]. The frequency box should be large enough to reach the asymptotic regions [31].

We now discuss the numerical setup for the flow equations that we used for both the fRG in Chapter 2 and the DMF<sup>2</sup>RG in Chapter 4.

We solved the flow equations reported in Appendix A by writing C++ code. To take into account the distinct momentum dependences of the self-energy and the vertex, we

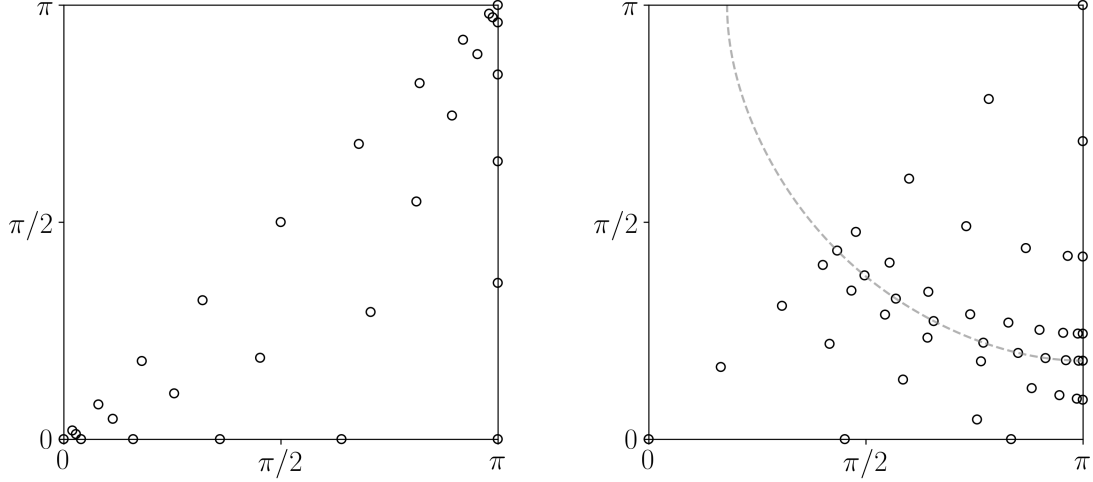


Figure B.1: Left: patch points for the momentum dependence  $\mathbf{Q}$  of the vertex. Right: patch points for the self-energy. In this case, it adapts according to the shape of the noninteracting Fermi surface. See the text for the connection between the patch points and the patch schemes.

defined two different patching schemes of the Brillouin zone. Similarly to what is done in Ref. [33], the vertex patching describes more accurately the corners around  $(0,0)$  and  $(\pi,\pi)$ , where we expect the instability vectors. In Fig. B.1 we show the set of points that define the patch scheme in the following way: whenever a general point in the (reduced) Brillouin Zone is accessed, we search for the closest point of our set, depicted in the figure. For the self-energy we concentrate the patches along the noninteracting Fermi surface and in its immediate vicinity with more points close to the *antinodal* region near  $(\pi,0)$ . In the calculations presented in the Chapters 2 and 4 we have used 29 patches for the vertex and 44 for the self-energy.

For the implementation of the frequency dependence of the interacting channels we found convenient to rewrite  $\mathcal{S}$ ,  $\mathcal{D}$ ,  $\mathcal{C}$  and  $\mathcal{M}$  as functions of three bosonic frequencies. Outside the frequency box, we numerically extrapolate the asymptotic values by following the structures presented in Ref. [31]. In the case of a pure *bosonic notation*, the extrapolation of the asymptotic behaviour is technically easier due to specific symmetries of the asymptotic functions [31]. The relation between the fermionic frequencies and the bosonic ones is nontrivial. In fact, there are combinations of three bosonic frequencies

that have no fermionic counterparts and, hence, are unphysical. When implementing the flow equations in this bosonic representation, we specifically calculate only the physical combinations of bosonic frequencies. For each frequency argument we restricted ourselves to at least 40 positive and 40 negative Matsubara frequencies.

We now discuss in more detail how we implemented the solution of the flow equations. For this scope, we report here the flow equation of the magnetic channel

$$\dot{\mathcal{M}}_{\mathbf{Q},\Omega}^{\Lambda}(\nu_1, \nu_2) = -T \sum_{\nu} L_{\mathbf{Q},\Omega}^{\text{m},\Lambda}(\nu_1, \nu) P_{\mathbf{Q},\Omega}^{\Lambda}(\nu) L_{\mathbf{Q},\Omega}^{\text{m},\Lambda}(\nu, \nu_2 - \Omega), \quad (\text{B.1})$$

with  $P_{\mathbf{Q},\Omega}^{\Lambda}(\omega)$  as in Eq. (A.15), and  $L_{\mathbf{Q},\Omega}^{\text{m},\Lambda}(\nu, \nu')$  in Eq. (A.18). The ODE is numerically solved by using the adaptive Runge-Kutta algorithm which mixes the 4th and 5th orders to estimate the errors. We use the Boost library [113] and set the absolute and relative error to circa  $10^{-3}$ .

At the step  $\Lambda$  we now show how we calculate the r.h.s. of Eq. (B.1), which depends on  $\Omega$ ,  $\nu_1$ ,  $\nu_2$  and  $\mathbf{Q}$ . We first calculate the momentum integrals contained in the function  $L_{\mathbf{Q},\Omega}^{\text{m},\Lambda}(\nu, \nu')$ , second and third line of Eq. (A.18). The loops over the  $\mathbf{Q}$ -patch and  $\Omega$  are parallelized by using openMP directives and setting a dynamical scheduling for the threads. Inside the loop, we calculate the momentum integral in  $P_{\mathbf{Q},\Omega}^{\Lambda}(\nu)$ , Eq. (A.15), for every frequency  $\nu$  and only then perform the summation over  $\nu$  in Eq. (B.1).

For the momentum integrals involved, we choose an adaptive cubature technique as implemented in the hcubature library [114] and based on Refs. [115, 116]. The relative and absolute errors are set to circa  $10^{-3}$  as in the ODE.



## Appendix C:

# DMFT from a functional perspective

In this section we propose an alternative perspective in understanding the DMFT procedure introduced in Chapter 1. We shall prove that, by approximating the self-energy to be a local function, the DMFT self-consistency condition (1.43) arises from the minimization of an action functional of the local Green's functions. Following Ref. [66], we start by introducing a new parameter  $\alpha$  in the Hubbard Hamiltonian as follows

$$\mathcal{H}_\alpha = \mathcal{H}_L + \alpha \mathcal{H}_{\text{NL}}, \quad (\text{C.1})$$

$$\mathcal{H}_L = U \sum_i n_{i,\uparrow} n_{i,\downarrow}, \quad (\text{C.2})$$

$$\mathcal{H}_{\text{NL}} = \sum_{ij} t_{ij} c_{i,\sigma}^\dagger c_{j,\sigma}. \quad (\text{C.3})$$

For  $\alpha = 1$  we recover the standard lattice Hamiltonian. Now we introduce

$$\begin{aligned} \Omega_\alpha[\Delta] = & -\ln \int \mathcal{D}\bar{\psi} \mathcal{D}\psi \exp\left\{ \left( \frac{1}{\beta} \int_0^\beta d\tau \int_0^\beta d\tau' \sum_{i\sigma} \bar{\psi}_{i,\sigma}(\tau) (-\partial_\tau + \mu) \psi_{i,\sigma}(\tau') - H_\alpha[\psi, \bar{\psi}] \right) \right. \\ & \left. - \frac{1}{\beta} \int_0^\beta d\tau \int_0^\beta d\tau' \sum_{i,\sigma} \Delta(\tau - \tau') \bar{\psi}_{i,\sigma}(\tau) \psi_{i,\sigma}(\tau') \right\}, \end{aligned} \quad (\text{C.4})$$

which is a functional of the external source  $\Delta(\tau)$  and depends on the new parameter  $\alpha$  through the Hamiltonian functional,  $H_\alpha[\psi, \bar{\psi}]$ , determined by the Hamiltonian operator  $\mathcal{H}_\alpha$ .  $\Omega_\alpha[\Delta]$  is similar to the Baym-Kadanoff functional with the difference here that

the source  $\Delta(\tau)$  is a local function. Considering the case  $\alpha = 0$ , the argument of the exponential in (C.4) can be written as  $S_{\text{eff}}[\Delta] = \sum_i S_{\text{eff},i}[\Delta]$ , with

$$S_{\text{eff},i}[\Delta] = -\frac{1}{\beta} \int_0^\beta d\tau \int_0^\beta d\tau' \sum_\sigma \bar{\psi}_{\sigma,i}(\tau) [-\partial_{\tau'} + \mu - \Delta(\tau - \tau')] \psi_{\sigma,i}(\tau') + U \int_0^\beta d\tau n_{\uparrow,i}(\tau) n_{\downarrow,i}(\tau), \quad (\text{C.5})$$

which represents the action of the AIM with a given hybridization function  $\Delta(\tau)$ . In analogy with the functional formalism reported in Chapter 1, we can define

$$G_\alpha[\Delta] \equiv \frac{\delta \Omega_\alpha}{\delta \Delta} = -\langle \psi_i(\tau) \bar{\psi}_i(\tau') \rangle_\Delta, \quad (\text{C.6})$$

where  $\langle \dots \rangle_\Delta$  is evaluated in the presence of the source field. Note that  $G_\alpha[\Delta]$ , for a given  $\Delta$ , is always a local function. We suppose that relation (C.6) is invertible and leads to the functional  $\Delta_\alpha[G]$ . In case of  $\Delta = 0$ , the functional (C.6) becomes the physical *local* Green's function of the lattice systems described by the Hamiltonian  $\mathcal{H}_\alpha$  (C.1)

$$G_\alpha[\Delta = 0] = -\langle \psi_i(\tau) \bar{\psi}_i(\tau') \rangle_\alpha \equiv G_{\alpha,\text{phys}}. \quad (\text{C.7})$$

Inverting this relation we have

$$\Delta_\alpha[G_{\alpha,\text{phys}}] = 0. \quad (\text{C.8})$$

From the functional (C.4) we are now able to define the *effective action functional* as the Legendre transform

$$\Gamma_\alpha[G] = \Omega_\alpha[\Delta_\alpha] - \int_0^\beta \Delta_\alpha(\tau) G(\tau), \quad (\text{C.9})$$

where on the r.h.s.  $\Delta_\alpha = \Delta_\alpha[G]$  is understood. The effective action introduced here should not be confused with the fRG counterpart, which is instead a functional of the fields  $\psi$  and  $\bar{\psi}$ . Taking the derivative of (C.9) with respect to  $G$  we have the relation

$$\frac{\delta \Gamma_\alpha}{\delta G} = -\Delta_\alpha[G]. \quad (\text{C.10})$$

Now, when restricting to the case of physical Green's function, and using the relation (C.8), Eq. (C.10) becomes

$$\left. \frac{\delta \Gamma_\alpha}{\delta G} \right|_{G=G_{\alpha, \text{phys}}} = 0. \quad (\text{C.11})$$

Eq. (C.11) reflects the main idea of this functional derivation, *i.e.*, the physical value for the local Green's function can be determined by the stationary point of the effective action functional. In fact, as we are going to show, after having approximated the self-energy with a local function, Eq. (C.11) yields the self-consistency relation of the DMFT.

For this scope, we start from the following trivial identity

$$\Gamma_{\alpha=1}[G] = \Gamma_{\alpha=0}[G] + \int_0^1 d\alpha \frac{d\Gamma_\alpha}{d\alpha}. \quad (\text{C.12})$$

Let us now concentrate on the second term of the right hand side in (C.12) by considering the  $\alpha$ -derivative of Eqs. (C.9)

$$\frac{d\Gamma_\alpha}{d\alpha} = \left. \frac{d\Omega_\alpha}{d\alpha} \right|_{\Delta=\text{const}} = \langle \mathcal{H}_{\text{NL}} \rangle \Big|_{\Delta_\alpha[G]} = \frac{1}{\beta} \int_{\mathbf{k}} \sum_{n,\sigma} \epsilon_{\mathbf{k}} G_\alpha(\omega_n, \mathbf{k}) \Big|_{\Delta_\alpha[G]}, \quad (\text{C.13})$$

where  $\langle \dots \rangle \Big|_{\Delta_\alpha[G]}$  and  $G_\alpha(\omega, \mathbf{k}) \Big|_{\Delta_\alpha[G]}$  are evaluated in the presence of the source field  $\Delta_\alpha[G]$ . Now, we can write

$$G_\alpha(\omega, \mathbf{k}) \Big|_{\Delta_\alpha[G]} = \frac{1}{i\omega + \mu - \Delta_\alpha[G] - \alpha \epsilon_{\mathbf{k}} - \Sigma_\alpha[G; \omega, \mathbf{k}]}, \quad (\text{C.14})$$

where we introduced the quantity  $\Sigma_\alpha[G; \omega, \mathbf{k}]$ , which is, in the case of  $\Delta = 0$ , the self-energy of the Hamiltonian (C.1). Here, we make use of the main approximation of the DMFT, *i.e.* we replace the functional  $\Sigma_\alpha[G; \omega, \mathbf{k}]$  by its value at  $\alpha = 0$ ,  $\Sigma_\alpha[G; \omega, \mathbf{k}] \simeq \Sigma_0[G; \omega]$ . To clarify the meaning of this approximation, we remind that  $\Omega_{\alpha=0}[\Delta]$  is the *free energy* of the Anderson impurity model for given hybridization function  $\Delta(\omega)$ . Hence, the  $\Sigma_0[G; \omega]$  represents the local self-energy of the AIM for a given local Green's function  $G$

$$\Sigma_0[G; \omega] = i\omega + \mu - \Delta_0[G] - G^{-1}(\omega). \quad (\text{C.15})$$

Given the DMFT approximation, Eq. (C.14) becomes

$$G_\alpha(\omega, \mathbf{k}) = \frac{1}{i\omega + \mu - \Delta_\alpha[G] - \alpha\epsilon_{\mathbf{k}} - \Sigma_0[G; \omega]}. \quad (\text{C.16})$$

Here, the  $\mathbf{k}$ -dependence of the Green's function is determined by the dispersion  $\epsilon_{\mathbf{k}}$  only.

To extract the functional  $\Delta_\alpha[G]$ , we get rid of the integration over  $\mathbf{k}$  in Eq. (C.16) with the help of the density of states  $D(\epsilon) = \int_{\mathbf{k}} \delta(\epsilon - \epsilon_{\mathbf{k}})$

$$G(\omega) = \int d\epsilon \frac{D(\epsilon)}{\Delta_0[G] - \Delta_\alpha[G] + G^{-1}(\omega) - \alpha\epsilon} = \frac{1}{\alpha} \tilde{D} \left( \frac{\Delta_0[G] - \Delta_\alpha[G] - G^{-1}(\omega)}{\alpha} \right). \quad (\text{C.17})$$

We used the Hilbert transform associated to the density of states  $D(\epsilon)$  as  $\tilde{D}(z) = \int d\epsilon \frac{D(\epsilon)}{z - \epsilon}$ .

By using the inverse Hilbert transform  $\tilde{D}[R(g)] = g$ , we extract  $\Delta_\alpha[G]$  by inverting Eq. (C.17)

$$\Delta_\alpha[G] = \Delta_0[G] + G^{-1} - \alpha R[\alpha G]. \quad (\text{C.18})$$

We are now able to rewrite Eq. (C.13) with the Green's function (C.16) and functional (C.18)

$$\frac{d\Gamma_\alpha}{d\alpha} = \frac{1}{\alpha\beta} \sum_n \int d\epsilon \frac{\epsilon D(\epsilon)}{R[\alpha G] - \epsilon} = \frac{1}{\alpha\beta} \sum_n [\alpha GR[\alpha G] - 1]. \quad (\text{C.19})$$

Our starting relation (C.12) becomes

$$\Gamma_{\alpha=1}[G] = \Gamma_{\alpha=0}[G] + \int_0^1 d\alpha \frac{1}{\alpha\beta} \sum_n [\alpha GR[\alpha G] - 1]. \quad (\text{C.20})$$

We are now ready to apply the stationary condition (C.11) for  $\alpha = 1$ ,  $\frac{\delta\Gamma_{\alpha=1}}{\delta G} \Big|_{G=G_{\text{phys}}} = 0$ . Taking the functional derivative of Eq. (C.20) and restricting to  $G = G_{\text{phys}}$  we have

$$0 = \frac{\delta\Gamma_{\alpha=1}}{\delta G} \Big|_{G=G_{\text{phys}}} = \frac{\delta\Gamma_{\alpha=0}}{\delta G} \Big|_{G=G_{\text{phys}}} + \frac{1}{\beta} \sum_n \int_0^1 d\alpha \frac{\delta}{\delta G} \left[ GR[\alpha G] - \frac{1}{\alpha} \right] \Big|_{G=G_{\text{phys}}}. \quad (\text{C.21})$$

By explicitly using relation (C.10) for  $\alpha = 0$ ,  $\delta\Gamma_{\alpha=0}/\delta G = -\Delta_0$ , we have

$$\Delta_0[G_{\text{phys}}] = \frac{1}{\beta} \sum_n \int_0^1 d\alpha \frac{\delta}{\delta G} [GR[\alpha G]] \Big|_{G=G_{\text{phys}}}. \quad (\text{C.22})$$

Considering the relation  $R[\alpha G] + \alpha G R'[\alpha G] = \frac{d}{d\alpha}[\alpha R[\alpha G]]$  and the property  $\lim_{x \rightarrow 0} R[x] = 1/x$ , the  $\alpha$ -integration can be carried out leading to

$$\Delta_0[G_{\text{phys}}] = R[G_{\text{phys}}] - G_{\text{phys}}^{-1}. \quad (\text{C.23})$$

Rearranging the terms and taking the Hilbert transform of both sides, we have

$$G_{\text{phys}}(\omega) = \int_{\mathbf{k}} \frac{1}{i\omega + \mu - \epsilon_{\mathbf{k}} - \Sigma_0(\omega)}, \quad \Sigma_0(\omega) = i\omega + \mu - \Delta_0(\omega) - G_{\text{phys}}^{-1}(\omega). \quad (\text{C.24})$$

Here, we restored the summation over  $\mathbf{k}$  and considered that  $\Sigma_0(\omega)$  is the solution of the Anderson impurity problem corresponding to the local Green's function  $G_{\text{phys}}$ . Eqs. (C.24) are equivalent to Eq. (1.43) and, hence, represent the self-consistency condition of DMFT.

To summarize, the DMFT self-consistency condition can be determined by the minimization of the functional of the local Green's function of the lattice system, the effective action (C.9), by approximating the self-energy to be local and determined by the AIM.



# Bibliography

- [1] J. G. Bednorz and K. A. Müller, “Possible high $T_c$  superconductivity in the Ba-La-Cu-O system”, *Z. Phys. B* **64** no. 2, 189–193 (Jun, 1986) .
- [2] B. Keimer, S. A. Kivelson, M. R. Norman, S. Uchida, and J. Zaanen, “From quantum matter to high-temperature superconductivity in copper oxides”, *Nature* **518**, 179 (2015) .
- [3] D. J. Scalapino, “A common thread: The pairing interaction for unconventional superconductors”, *Rev. Mod. Phys.* **84**, 1383–1417 (Oct, 2012) .
- [4] N. E. Hussey, “Phenomenology of the normal state in-plane transport properties of high- $T_c$  cuprates”, *J. Phys.: Condens. Matter* **20** no. 12, 123201 (2008) .
- [5] R. Comin, A. Frano, M. M. Yee, Y. Yoshida, H. Eisaki, E. Schierle, E. Weschke, R. Sutarto, F. He, A. Soumyanarayanan, Y. He, M. Le Tacon, I. S. Elfimov, J. E. Hoffman, G. A. Sawatzky, B. Keimer, and A. Damascelli, “Charge order driven by Fermi-arc instability in  $\text{Bi}_2\text{Sr}_{2-x}\text{La}_x\text{CuO}_{6+\delta}$ ”, *Science* **343** no. 6169, 390–392 (2014) .
- [6] R. Comin, R. Sutarto, F. He, E. H. de Silva Note, L. Chauviere, A. Frano, W. N. Liang, R. Hardy, D. A. Bonn, Y. Yoshida, H. Eisaki, A. J. Achkar, D. G. Hawthorn, B. Keimer, G. A. Sawatzky, and A. Damascelli, “Symmetry of charge order in cuprates”, *Nature Materials* **14**, 796 (2014) .
- [7] P. W. Anderson, “The resonating valence bond state in  $\text{La}_2\text{CuO}_4$  and superconductivity”, *Science* **235** no. 4793, 1196–1198 (1987) .

- 
- [8] F. C. Zhang and T. M. Rice, “Effective Hamiltonian for the superconducting Cu oxides”, *Phys. Rev. B* **37**, 3759–3761 (Mar, 1988) .
- [9] J. Hubbard, “Electron correlations in narrow energy bands”, *Proc. R. Soc. A* **276**, 238–257 (Nov., 1963) .
- [10] R. Jördens, N. Strohmaier, K. Günter, H. Moritz, and T. Esslinger, “A Mott insulator of fermionic atoms in an optical lattice”, *Nature* **455**, 204 (2008) .
- [11] U. Schneider, L. Hackermüller, S. Will, T. Best, I. Bloch, T. A. Costi, R. W. Helmes, D. Rasch, and A. Rosch, “Metallic and insulating phases of repulsively interacting fermions in a 3d optical lattice”, *Science* **322** no. 5907, 1520–1525 (2008) .
- [12] T. Esslinger, “Fermi-Hubbard physics with atoms in an optical lattice”, *Annu. Rev. Condens. Matter Phys.* **1** no. 1, 129–152 (2010) .
- [13] K. Borejsza and N. Dupuis, “Antiferromagnetism and single-particle properties in the two-dimensional half-filled Hubbard model: A nonlinear sigma model approach”, *Phys. Rev. B* **69**, 085119 (Feb, 2004) .
- [14] N. E. Bickers, D. J. Scalapino, and S. R. White, “Conserving approximations for strongly correlated electron systems: Bethe-Salpeter equation and dynamics for the two-dimensional Hubbard model”, *Phys. Rev. Lett.* **62**, 961–964 (Feb, 1989) .
- [15] D. Scalapino, “The case for  $d_{x^2-y^2}$  pairing in the cuprate superconductors”, *Phys. Rep.* **250** no. 6, 329 – 365 (1995) .
- [16] A. Georges and J. S. Yedidia, “Onsager reaction terms for quantum many-body systems: Application to antiferromagnetic and superconducting order in the Hubbard model”, *Phys. Rev. B* **43**, 3475–3482 (Feb, 1991) .
- [17] A. T. Zheleznyak, V. M. Yakovenko, and I. E. Dzyaloshinskii, “Parquet solution for a flat Fermi surface”, *Phys. Rev. B* **55**, 3200–3215 (Feb, 1997) .
- [18] G. Li, A. Kauch, P. Pudleiner, and K. Held, “The victory project v1.0: an efficient parquet equations solver”, [arXiv:1708.07457](https://arxiv.org/abs/1708.07457) [`cond-mat.str-el`].

- [19] C. Wetterich, “Exact evolution equation for the effective potential”, *Phys. Lett. B* **301**, 90–94 (Feb., 1993) .
- [20] W. Metzner, M. Salmhofer, C. Honerkamp, V. Meden, and K. Schönhammer, “Functional renormalization group approach to correlated fermion systems”, *Rev. Mod. Phys.* **84**, 299–352 (Jan, 2012) .
- [21] K. G. Wilson, “Renormalization group and critical phenomena. I. Renormalization group and the Kadanoff scaling picture”, *Phys. Rev. B* **4**, 3174–3183 (Nov, 1971) .
- [22] L. P. Kadanoff, “Scaling laws for Ising models near  $T(c)$ ”, *Physics* **2**, 263–272 (1966) .
- [23] K. G. Wilson and J. Kogut, “The renormalization group and the  $\epsilon$  expansion”, *Phys. Rep.* **12** no. 2, 75 – 199 (1974) .
- [24] J. Polchinski, “Renormalization and effective lagrangians”, *Nucl. Phys. B* **231** no. 2, 269 – 295 (1984) .
- [25] C. J. Halboth and W. Metzner, “ $d$ -wave superconductivity and Pomeranchuk instability in the two-dimensional Hubbard model”, *Phys. Rev. Lett.* **85**, 5162–5165 (Dec, 2000) .
- [26] C. Honerkamp, M. Salmhofer, N. Furukawa, and T. M. Rice, “Breakdown of the Landau-Fermi liquid in two dimensions due to umklapp scattering”, *Phys. Rev. B* **63**, 035109 (Jan, 2001) .
- [27] D. Zanchi and H. J. Schulz, “Weakly correlated electrons on a square lattice: A renormalization group theory”, *Europhys. Lett.* **44** no. 2, 235 (1998) .
- [28] D. Zanchi and H. J. Schulz, “Weakly correlated electrons on a square lattice: Renormalization-group theory”, *Phys. Rev. B* **61**, 13609–13632 (May, 2000) .
- [29] C. Karrasch, R. Hedden, R. Peters, T. Pruschke, K. Schönhammer, and V. Meden, “A finite-frequency functional renormalization group approach to the single impurity Anderson model”, *J. Phys.: Condens. Matter* **20** no. 34, 345205 (2008) .

- [30] M. Kinza, J. Ortloff, J. Bauer, and C. Honerkamp, “Alternative functional renormalization group approach to the single impurity Anderson model”, *Phys. Rev. B* **87** no. 3, 035111 (Jan, 2013) .
- [31] N. Wentzell, G. Li, A. Tagliavini, C. Taranto, G. Rohringer, K. Held, A. Toschi, and S. Andergassen, “High-frequency asymptotics of the vertex function: diagrammatic parametrization and algorithmic implementation”, [arXiv:1610.06520](https://arxiv.org/abs/1610.06520) [`cond-mat.str-el`].
- [32] C. Honerkamp, H. Fu, and D.-H. Lee, “Phonons and  $d$ -wave pairing in the two-dimensional Hubbard model”, *Phys. Rev. B* **75**, 014503 (Jan, 2007) .
- [33] C. Husemann and M. Salmhofer, “Efficient parametrization of the vertex function,  $\Omega$  scheme, and the  $t, t'$  Hubbard model at van Hove filling”, *Phys. Rev. B* **79** no. 19, 195125 (May, 2009) .
- [34] C. Husemann, K.-U. Giering, and M. Salmhofer, “Frequency-dependent vertex functions of the  $(t, t')$  Hubbard model at weak coupling”, *Phys. Rev. B* **85**, 075121 (Feb, 2012) .
- [35] A. Eberlein and W. Metzner, “Superconductivity in the two-dimensional  $t$ - $t'$ -Hubbard model”, *Phys. Rev. B* **89**, 035126 (Jan, 2014) .
- [36] A. Eberlein and W. Metzner, “Effective interactions and fluctuation effects in spin-singlet superfluids”, *Phys. Rev. B* **87**, 174523 (May, 2013) .
- [37] T. Baier, E. Bick, and C. Wetterich, “Temperature dependence of antiferromagnetic order in the Hubbard model”, *Phys. Rev. B* **70**, 125111 (Sep, 2004) .
- [38] H. Gies and C. Wetterich, “Renormalization flow of bound states”, *Phys. Rev. D* **65**, 065001 (Feb, 2002) .
- [39] N. D. Mermin and H. Wagner, “Absence of ferromagnetism or antiferromagnetism in one- or two-dimensional isotropic Heisenberg models”, *Phys. Rev. Lett.* **17**, 1133–1136 (Nov, 1966) .

- [40] W. Metzner and D. Vollhardt, “Correlated lattice fermions in  $d = \infty$  dimensions”, *Phys. Rev. Lett.* **62**, 324–327 (Jan, 1989) .
- [41] A. Georges and G. Kotliar, “Hubbard model in infinite dimensions”, *Phys. Rev. B* **45**, 6479–6483 (Mar, 1992) .
- [42] A. Georges, G. Kotliar, W. Krauth, and M. J. Rozenberg, “Dynamical mean-field theory of strongly correlated fermion systems and the limit of infinite dimensions”, *Rev. Mod. Phys.* **68**, 13–125 (Jan, 1996) .
- [43] T. Maier, M. Jarrell, T. Pruschke, and M. H. Hettler, “Quantum cluster theories”, *Rev. Mod. Phys.* **77**, 1027–1080 (Oct, 2005) .
- [44] G. Rohringer, H. Hafermann, A. Toschi, A. A. Katanin, A. E. Antipov, M. I. Katsnelson, A. I. Lichtenstein, A. N. Rubtsov, and K. Held, “Diagrammatic routes to nonlocal correlations beyond dynamical mean field theory”, *Rev. Mod. Phys.* **90**, 025003 (May, 2018) .
- [45] D. J. Scalapino, *Handbook of High-Temperature Superconductivity*. Springer, New York, 2007.
- [46] E. Gull, O. Parcollet, and A. J. Millis, “Superconductivity and the pseudogap in the two-dimensional Hubbard model”, *Phys. Rev. Lett.* **110**, 216405 (May, 2013) .
- [47] X. Chen, J. P. F. LeBlanc, and E. Gull, “Superconducting fluctuations in the normal state of the two-dimensional Hubbard model”, *Phys. Rev. Lett.* **115**, 116402 (Sep, 2015) .
- [48] A. Toschi, A. A. Katanin, and K. Held, “Dynamical vertex approximation: A step beyond dynamical mean-field theory”, *Phys. Rev. B* **75**, 045118 (Jan, 2007) .
- [49] T. Ayral and O. Parcollet, “Mott physics and spin fluctuations: A unified framework”, *Phys. Rev. B* **92**, 115109 (Sep, 2015) .
- [50] G. Rohringer and A. Toschi, “Impact of nonlocal correlations over different energy scales: A dynamical vertex approximation study”, *Phys. Rev. B* **94**, 125144 (Sep, 2016) .

- [51] M. Kitatani, T. Schäfer, H. Aoki, and K. Held, “Why  $T_c$  is so low in high- $T_c$  cuprates: importance of the dynamical vertex structure”, [arXiv:1801.05991](#) [`cond-mat.supr-con`].
- [52] J. Vučičević, T. Ayrál, and O. Parcollet, “TRILEX and  $GW+EDMFT$  approach to  $d$ -wave superconductivity in the Hubbard model”, *Phys. Rev. B* **96**, 104504 (Sep, 2017) .
- [53] C. Taranto, S. Andergassen, J. Bauer, K. Held, A. Katanin, W. Metzner, G. Rohringer, and A. Toschi, “From infinite to two dimensions through the functional renormalization group”, *Phys. Rev. Lett.* **112** no. 19, 196402 (May, 2014) .
- [54] G. Rohringer, A. Valli, and A. Toschi, “Local electronic correlation at the two-particle level”, *Phys. Rev. B* **86** no. 12, 125114 (Sept., 2012) .
- [55] C. Honerkamp and M. Salmhofer, “Magnetic and superconducting instabilities of the Hubbard model at the van Hove filling”, *Phys. Rev. Lett.* **87**, 187004 (Oct, 2001) .
- [56] C. Honerkamp and M. Salmhofer, “Temperature-flow renormalization group and the competition between superconductivity and ferromagnetism”, *Phys. Rev. B* **64**, 184516 (Oct, 2001) .
- [57] A. A. Katanin, “Fulfillment of Ward identities in the functional renormalization group approach”, *Phys. Rev. B* **70**, 115109 (Sep, 2004) .
- [58] M. Salmhofer, C. Honerkamp, W. Metzner, and O. Lauscher, “Renormalization group flows into phases with broken symmetry”, *Prog. Theor. Phys.* **112** no. 6, 943–970 (2004) .
- [59] A. Eberlein, “Fermionic two-loop functional renormalization group for correlated fermions: Method and application to the attractive Hubbard model”, *Phys. Rev. B* **90**, 115125 (Sep, 2014) .
- [60] C. Honerkamp, D. Rohe, S. Andergassen, and T. Enss, “Interaction flow method for many-fermion systems”, *Phys. Rev. B* **70**, 235115 (Dec, 2004) .

- [61] M. Salmhofer and C. Honerkamp, “Fermionic renormalization group flows —technique and theory—”, *Prog. Theor. Phys.* **105**, 1–35 (Jan, 2001) .
- [62] N. Wentzell, C. Taranto, A. Katanin, A. Toschi, and S. Andergassen, “Correlated starting points for the functional renormalization group”, *Phys. Rev. B* **91**, 045120 (Jan, 2015) .
- [63] S. Friederich, H. C. Krahl, and C. Wetterich, “Four-point vertex in the Hubbard model and partial bosonization”, *Phys. Rev. B* **81**, 235108 (Jun, 2010) .
- [64] S. Uebelacker and C. Honerkamp, “Self-energy feedback and frequency-dependent interactions in the functional renormalization group flow for the two-dimensional Hubbard model”, *Phys. Rev. B* **86**, 235140 (Dec, 2012) .
- [65] D. Vilardi, C. Taranto, and W. Metzner, “Nonseparable frequency dependence of the two-particle vertex in interacting fermion systems”, *Phys. Rev. B* **96**, 235110 (Dec, 2017) .
- [66] A. Georges, “Strongly correlated electron materials: Dynamical mean field theory and electronic structure”, *AIP Conference Proceedings* **715** no. 1, 3–74 (2004) .
- [67] E. Müller-Hartmann, “Correlated fermions on a lattice in high dimensions”, *Z. Phys. B* **74** no. 4, 507–512 (Dec, 1989) .
- [68] A. Abrikosov, L. Gorkov, and D. I.E., *Methods of quantum field theory in statistical physics*. Dover Publications, Inc., 1963.
- [69] U. Brandt and C. Mielsch, “Free energy of the Falicov-Kimball model in large dimensions”, *Z. Phys. B* **82** no. 1, 37–41 (Feb, 1991) .
- [70] J. E. Hirsch and R. M. Fye, “Monte Carlo method for magnetic impurities in metals”, *Phys. Rev. Lett.* **56**, 2521–2524 (Jun, 1986) .
- [71] K. G. Wilson, “The renormalization group: Critical phenomena and the Kondo problem”, *Rev. Mod. Phys.* **47**, 773–840 (Oct, 1975) .
- [72] M. Caffarel and W. Krauth, “Exact diagonalization approach to correlated fermions in infinite dimensions: Mott transition and superconductivity”, *Phys. Rev. Lett.* **72**, 1545–1548 (Mar, 1994) .

- [73] N. Blümer, *Mott-Hubbard Metal-Insulator Transition and Optical Conductivity in High Dimensions*. PhD thesis, Universität Augsburg, 2002.
- [74] C. Taranto, *Diagrammatic methods beyond DMFT*. PhD thesis, Technischen Universität Wien, 2015.
- [75] N. Mott, “The basis of the electron theory of metals, with special reference to the transition metals”, *Proc. Phys. Soc. A* **62** no. 7, 416 (1949) .
- [76] N. F. Mott, *Metal-insulator transitions*. Taylor and Francis, London, 1990.
- [77] E. Gull, P. Werner, X. Wang, M. Troyer, and A. J. Millis, “Local order and the gapped phase of the Hubbard model: A plaquette dynamical mean-field investigation”, *Europhys. Lett.* **84** no. 3, 37009 (2008) .
- [78] G. Rohringer, *New routes toward a theoretical treatment of nonlocal electronic correlations*. PhD thesis, Technische Universität Wien, 2014.
- [79] H. Hafermann, C. Jung, S. Brener, M. I. Katsnelson, A. N. Rubtsov, and A. I. Lichtenstein, “Superperturbation solver for quantum impurity models”, *Europhys. Lett.* **85** no. 2, 27007 (2009) .
- [80] Pairault, S., Sénéchal, D., and A.-M.S. Tremblay, “Strong-coupling perturbation theory of the Hubbard model”, *Eur. Phys. J. B* **16** no. 1, 85–105 (2000) .
- [81] K.-M. Tam, S.-W. Tsai, D. K. Campbell, and A. H. Castro Neto, “Phase diagram of the Holstein-Hubbard two-leg ladder using a functional renormalization-group method”, *Phys. Rev. B* **75**, 195119 (May, 2007) .
- [82] H. Bakrim and C. Bourbonnais, “Superconductivity close to the charge-density-wave instability”, *Europhys. Lett.* **90** no. 2, 27001 (2010) .
- [83] B. Binz, D. Baeriswyl, and B. Douçot, “Weakly interacting electrons and the renormalization group”, *Ann. Phys.* **12**, 704–736 (2003) .
- [84] A. L. Fetter and J. D. Walecka, *Quantum Theory of Many-Particle Systems*. Dover Publications, 2003.

- [85] C. Platt, W. Hanke, and R. Thomale, “Functional renormalization group for multi-orbital Fermi surface instabilities”, *Adv. Phys.* **62** no. 4-6, 453–562 (2013) .
- [86] H. Hafermann, E. G. C. P. van Loon, M. I. Katsnelson, A. I. Lichtenstein, and O. Parcollet, “Collective charge excitations of strongly correlated electrons, vertex corrections, and gauge invariance”, *Phys. Rev. B* **90**, 235105 (Dec, 2014) .
- [87] E. A. Stepanov, E. G. C. P. van Loon, A. A. Katanin, A. I. Lichtenstein, M. I. Katsnelson, and A. N. Rubtsov, “Self-consistent dual boson approach to single-particle and collective excitations in correlated systems”, *Phys. Rev. B* **93**, 045107 (Jan, 2016) .
- [88] C. Honerkamp, “Electron-doping versus hole-doping in the 2d  $t - t'$  Hubbard model”, *Eur. Phys. J. B* **21** no. 1, 81–91 (2001) .
- [89] C. Honerkamp and M. Salmhofer, “Flow of the quasiparticle weight in the  $N$ -patch renormalization group scheme”, *Phys. Rev. B* **67**, 174504 (May, 2003) .
- [90] D. Rohe and W. Metzner, “Pseudogap at hot spots in the two-dimensional Hubbard model at weak coupling”, *Phys. Rev. B* **71**, 115116 (Mar, 2005) .
- [91] T. Schäfer, F. Geles, D. Rost, G. Rohringer, E. Arrigoni, K. Held, N. Blümer, M. Aichhorn, and A. Toschi, “Fate of the false Mott-Hubbard transition in two dimensions”, *Phys. Rev. B* **91**, 125109 (Mar, 2015) .
- [92] W. Wu, M. Ferrero, A. Georges, and E. Kozik, “Controlling Feynman diagrammatic expansions: Physical nature of the pseudogap in the two-dimensional Hubbard model”, *Phys. Rev. B* **96**, 041105 (Jul, 2017) .
- [93] X. Montiel, T. Kloss, and C. Pépin, “Effective SU(2) theory for the pseudogap state”, *Phys. Rev. B* **95**, 104510 (Mar, 2017) .
- [94] A. Abanov, A. V. Chubukov, and J. Schmalian, “Quantum-critical theory of the spin-fermion model and its application to cuprates: Normal state analysis”, *Adv. Phys.* **52** no. 3, 119–218 (2003) .

- [95] Y.M. Vilk and A.-M.S. Tremblay, “Non-perturbative many-body approach to the Hubbard model and single-particle pseudogap”, *J. Phys. I France* **7** no. 11, 1309–1368 (1997) .
- [96] W. Wu, M. S. Scheurer, S. Chatterjee, S. Sachdev, A. Georges, and M. Ferrero, “Pseudogap and Fermi surface topology in the two-dimensional Hubbard model”, [arXiv:1707.06602](https://arxiv.org/abs/1707.06602) [cond-mat.str-el].
- [97] D. Furman and M. Blume, “Ornstein-Zernike expression for correlation functions near a tricritical point”, *Phys. Rev. B* **10**, 2068–2077 (Sep, 1974) .
- [98] A.-M. Daré, Y. M. Vilk, and A. M. S. Tremblay, “Crossover from two- to three-dimensional critical behavior for nearly antiferromagnetic itinerant electrons”, *Phys. Rev. B* **53**, 14236–14251 (Jun, 1996) .
- [99] P. A. Igoshev, A. V. Efremov, A. I. Poteryaev, A. A. Katanin, and V. I. Anisimov, “Magnetic fluctuations and effective magnetic moments in  $\gamma$ -iron due to electronic structure peculiarities”, *Phys. Rev. B* **88**, 155120 (Oct, 2013) .
- [100] A. Toschi, R. Arita, P. Hansmann, G. Sangiovanni, and K. Held, “Quantum dynamical screening of the local magnetic moment in Fe-based superconductors”, *Phys. Rev. B* **86**, 064411 (Aug, 2012) .
- [101] M. Liu, L. W. Harriger, H. Luo, M. Wang, R. A. Ewings, T. Guidi, H. Park, K. Haule, G. Kotliar, S. M. Hayden, and P. Dai, “Nature of magnetic excitations in superconducting  $\text{BaFe}_{1.9}\text{Ni}_{0.1}\text{As}_2$ ”, *Nat. Phys.* **8**, 376–381 (May, 2012) .
- [102] D. Vilaridi, C. Taranto, and W. Metzner, “Dynamically enhanced magnetic incommensurability: Effects of local dynamics on nonlocal spin correlations in a strongly correlated metal”, *Phys. Rev. B* **97**, 235110 (Jun, 2018) .
- [103] T. Holder and W. Metzner, “Incommensurate nematic fluctuations in two-dimensional metals”, *Phys. Rev. B* **85**, 165130 (Apr, 2012) .
- [104] J. Kuneš, “Efficient treatment of two-particle vertices in dynamical mean-field theory”, *Phys. Rev. B* **83**, 085102 (Feb, 2011) .

- [105] A. Toschi, M. Capone, and C. Castellani, “Energetic balance of the superconducting transition across the BCS—Bose Einstein crossover in the attractive Hubbard model”, *Phys. Rev. B* **72**, 235118 (Dec, 2005) .
- [106] G. Sangiovanni, A. Toschi, E. Koch, K. Held, M. Capone, C. Castellani, O. Gunnarsson, S.-K. Mo, J. W. Allen, H.-D. Kim, A. Sekiyama, A. Yamasaki, S. Suga, and P. Metcalf, “Static versus dynamical mean-field theory of Mott antiferromagnets”, *Phys. Rev. B* **73**, 205121 (May, 2006) .
- [107] C. Taranto, G. Sangiovanni, K. Held, M. Capone, A. Georges, and A. Toschi, “Signature of antiferromagnetic long-range order in the optical spectrum of strongly correlated electron systems”, *Phys. Rev. B* **85**, 085124 (Feb, 2012) .
- [108] L. Taillefer, “Scattering and pairing in cuprate superconductors”, *Annu. Rev. Condens. Matter Phys.* **1** no. 1, 51–70 (2010) .
- [109] L. Fratino, P. Sémon, G. Sordi, and A.-M. S. Tremblay, “Pseudogap and superconductivity in two-dimensional doped charge-transfer insulators”, *Phys. Rev. B* **93**, 245147 (Jun, 2016) .
- [110] W. Metzner, C. Castellani, and C. Di Castro, “Fermi systems with strong forward scattering”, *Adv. Phys.* **47** no. 3, 317–445 (1998) .
- [111] B. I. Shraiman and E. D. Siggia, “Spiral phase of a doped quantum antiferromagnet”, *Phys. Rev. Lett.* **62**, 1564–1567 (Mar, 1989) .
- [112] V. N. Kotov and O. P. Sushkov, “Stability of the spiral phase in the two-dimensional extended  $t-J$  model”, *Phys. Rev. B* **70**, 195105 (Nov, 2004) .
- [113] B. Schling, *The Boost C++ Libraries*. XML Press, 2011.
- [114] S. G. Johnson, “Cubature”. [http://ab-initio.mit.edu/wiki/index.php/Cubature\\_\(Multi-dimensional\\_integration\)](http://ab-initio.mit.edu/wiki/index.php/Cubature_(Multi-dimensional_integration)).
- [115] A. C. Genz and A. A. Malik, “Remarks on algorithm 006: An adaptive algorithm for numerical integration over an N-dimensional rectangular region”, *J. Comput. Appl. Math.* **6** no. 4, 295 – 302 (1980) .

- [116] J. Berntsen, T. O. Espelid, and A. Genz, “Algorithm 698: DCUHRE: An adaptive multidimensional integration routine for a vector of integrals”, *ACM Trans. Math. Softw.* **17** no. 4, 452–456 (Dec, 1991) .

# Acknowledgments

I would like to acknowledge the people involved in the realization of this thesis. First of all, I thank my supervisor, Walter Metzner, for his excellent guidance. His deep expertise on renormalization group and condensed matter physics gave me the possibility to improve my knowledge in the early stage of the scientific career. His lessons and advices on how the research should be pursued were precious. Besides the funding supports for many conferences and workshops, I thank him also for transferring his passion on the interesting physical aspects in our field. Maria Daghofer is thanked for co-refereeing this thesis.

I have a debt of gratitude with my collaborator Ciro Taranto for having inspired me with scientific and personal discussions. I thank him for the precious time we had in the years spent together in the office and for teaching me to look at the 'general framework' and not only at technical details.

A special thank goes to my wife for her continuous and essential support during my time as PhD student.

I am grateful to Sabine Andergassen for the several discussions and visits in her group in Tübingen. I also thank Alessandro Toschi and Karsten Held for inviting me in Vienna and for the discussions I had in their groups. I am grateful to Carsten Honerkamp for giving me the chance to present my studies at the RWTH in Aachen. Let me acknowledge all the people I discussed with during my PhD in Stuttgart, in particular, Daniil Mantadakis, Xiaodong Cao and Philipp Hansmann.

Finally, I thank all the people I met in conferences and workshops who shared their understanding of the physical issues.



# Deutsche Zusammenfassung

Die Behandlung stark wechselwirkender zweidimensionaler Fermi Systeme ist eines der größten Probleme auf dem Gebiet der Festkörperphysik. Viele theoretische Arbeiten konzentrierten sich auf das stark wechselwirkende Hubbard-Modell, da erwartet wird, dass es die wichtigste Physik von Kupratsupraleitern erfasst. Aufgrund unserer methodischen Verbesserungen und des Verständnisses der Frequenzabhängigkeit der Zweiteilchen-Vertexfunktion kann die funktionale Renormierungsgruppe in Kombination mit der dynamischen Molekularfeldtheorie nun dazu verwendet werden, konkurrierende Korrelationen im stark wechselwirkenden Regime zu untersuchen.

Die funktionale Renormierungsgruppe ist normalerweise nur bei moderater Wechselwirkung anwendbar, beschreibt aber effizient Systeme mit einer Hierarchie unterschiedlicher Energieskalen und konkurrierenden Korrelationen. Zum Beispiel liefert es eindeutige Evidenz für die d-Wellen-Supraleitung im zweidimensionalen Hubbard-Modell bei moderater Kopplung. In einem ersten Projekt untersuchen wir die Frequenzabhängigkeit der durch den funktionalen Renormierungsgruppenfluss generierten einteilchenirreduziblen Vertexfunktion. Die Frequenzabhängigkeit, die für starke Wechselwirkungen singular wird, scheint bereits für moderate Kopplungen wichtig zu sein, und sie kann nicht durch getrennte Kanäle repräsentiert werden, die jeweils nur von einer einzigen linearen Kombination von Frequenzen abhängen.

Bei stark wechselwirkenden Systemen erfasst die dynamische Molekularfeldtheorie starke lokale Korrelationseffekte nicht-perturbativ. Mit dieser Näherung untersuchen wir den Einfluss lokaler Korrelationen auf die magnetische Suszeptibilität. Die lokale Dynamik beeinflusst stark die Spinantwortfunktion und ihre Impulsabhängigkeit. Im Gegensatz zu der weit verbreiteten Random-Phase-Approximation mit Selbstenergiekorrekturen, die antiferromagnetische Néel Ordnung vorhersagt, begünstigen die lokalen Vertex-

Korrekturen eine inkommensurable Ordnung ähnlich der von der Fermi-flächengeometrie vorhergesagten Instabilität, wie für schwach wechselwirkende Systeme.

Die dynamische Molekularfeldtheorie wird auch als Ausgangspunkt für den funktionalen Renormierungsgruppenfluss verwendet. Wir zeigen, dass ein solcher Ansatz aufgrund unserer Verbesserungen bei der Parametrisierung der Vertex-Funktion tatsächlich in der Lage ist, die starke Kopplungsphysik zu erfassen. Darüber hinaus leiten wir ein Flussschema ab, das die lokalen Beiträge erhält und den Trunkierungsfehler der Flussgleichungen reduziert. Im stark wechselwirkenden Regime finden wir starke  $d$ -Wellen-Paarungskorrelationen, die durch magnetische Fluktuationen angetrieben werden, mit einem Mechanismus, der dem im schwach wechselwirkenden System ähnelt.